

OPTICAL PROPERTIES OF III-V AND II-VI STRAINED
SEMICONDUCTOR HETEROSTRUCTURES
UNDER PRESSURE

By

SEON-JU HWANG

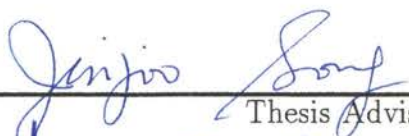
Bachelor of Science
Pusan National University
Pusan, Korea
1982

Master of Science
Pusan National University
Pusan, Korea
1984

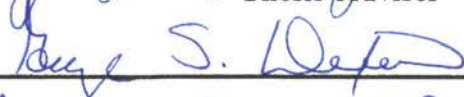
Submitted to the Faculty of the
Graduate College of the
Oklahoma State University
in partial fulfillment of
the requirements for
the Degree of
DOCTOR OF PHILOSOPHY
December, 1994

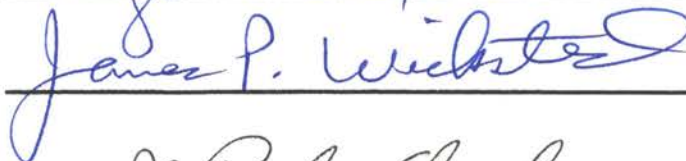
OPTICAL PROPERTIES OF III-V AND II-VI STRAINED
SEMICONDUCTOR HETEROSTRUCTURES
UNDER PRESSURE

Thesis Approved:



Thesis Adviser









Dean of the Graduate College

ACKNOWLEDGEMENTS

I wish to express my sincere gratitude to every individual who helped and supported me in various ways. However, I regret that I can not put all names here because of the limited space.

My sincerest gratitude goes to my thesis advisor, Dr. Jin-Joo Song, for giving me the opportunity to work in her laboratory. I deeply appreciate her guidance, encouragement, patience and support during the course of this work. I am also grateful to my committee members, Dr. George S. Dixon, Dr. James P. Wicksted, and Dr. J. Paul Devlin, for their careful review of my thesis and valuable discussions. I am also thankful to Dr. Wei Shan for his invaluable aid and contributions to this work. I am greatly thankful to sample growers who supplied samples for this study: Dr. C.W. Tu and Dr. H.Q. Hou at University of California in San Jose, Dr. Yao and Zhu at Hiroshima University in Japan, and Dr. Morkoç at University of Illinois in Urbana-Champaign.

I would like to express my gratitude to all co-workers in Dr. Song's group: Arthur Fischer, Theodore Schmitt, Drs. John M. Hays, Xiao Hua Yang, John Jacob, Abdellatif Bouchalkha, Jin Fu Zhou, Pan Sang Jung. The time I have spent the last several years with them will be unforgettable and a very important part of my life. In particular, I owe a lot Dr. John Hays and Arthur Fisher for their careful review, discussions and proof reading. I would like to thank all of the professors in the physics department. I am also thankful of all staffs in physics department and Center for Laser Research, and machine shop.

I am also grateful to church members and friends. Thanks to pastor Shin-Kwan Chung who prayed for me and encouraged me. I also thank to pastor Kie-Tai Kim and all church members for their prayers and support. More importantly I want to glorify the Lord and to thank Him for His grace and blessing.

My greatest gratitude is to my family. Without their great support, this work could not be completed. I thank my parents, Chi-Hyun Hwang and Hee-Ok Cho, and parents-in-law, Myung-Soo and Un-Sang Lee, whose unlimited support, sacrifices and prayers I cannot find any words to describe. Thanks to brothers and sisters for their encouragement and prayers.

Lastly, I would like to thank to my wife, Yun Ok, for her love, sacrifice, patient, support and prayers. I wish I can find a way to describe my appreciation for her.

TABLE OF CONTENTS

Chapter	Page
I. INTRODUCTION	1
Electronic band structures	1
Bulk semiconductor	1
Heterostructures	4
Band offsets in QW structures	7
Strained layer semiconductor heterostructures	9
Accommodation of lattice mismatched heterostructures	9
Effects of strain on the band structures of het-	
erostructures	12
Motivation of this study	14
II. ELECTRONIC PROPERTIES OF STRAINED HET-	
EROSTRUCTURES	17
Strain effects on band structures	17
Effects of homogeneous strain on electronic	
energy levels	17
Calculation of interband transitions: envelope func-	
tion approximation	25
Band offset	32
Energy level crossing and valence band offset	33
III. EXPERIMENTAL TECHNIQUES	38
Optical measurements	38
Photoluminescence and excitation spectroscopies	38
Modulation spectroscopy	42
Diamond anvil cell technique	52
Principle of diamond anvil cells	52
Pressure media	54
Sample preparation	54
Pressure calibration	55

Chapter	Page
IV. GaAs/GaAs _{1-x} P _x STRAINED MULTIPLE QUANTUM WELLS . . .	57
Introduction	57
Experimental details and results	58
Analysis and discussion	66
Energy level crossover and valence band offset	68
Pressure coefficients and identification of un- known transitions	73
Conclusions	76
V. InAs _x P _{1-x} /InP STRAINED MULTIPLE QUANTUM WELLS . . .	78
Introduction	78
Experiments	79
Sample preparations	79
Experimental technique	79
Results and discussion	81
Conclusions	88
VI. HIGHLY STRAINED CdSe/ZnSe QUANTUM WELLS	89
Introduction	89
Experimental details and results	90
Sample preparations	90
Experimental technique	93
Experimental results	94
Analysis and discussion	97
Effects of hydrostatic pressure	103
Estimation of critical thickness	110
MQW and SQW	111
Franz-Keldysh oscillation	113
Conclusions	115
VII. CUBIC GaN EPILAYER GROWN ON A GaAs SUBSTRATE . . .	118
Introduction	118
Experimental results and discussion	120
Conclusion	128
VIII. SUMMARY	129
BIBLIOGRAPHY	134

LIST OF TABLES

Table		Page
I.	Parameters used for the calculations for GaAs/GaAs _x P _{1-x} SMQWs	69
II.	Pressure coefficients of various PL transitions in the GaAs/ GaAs _x P _{1-x} SMQWs	74
III.	Sample parameters of InAsP/InP strained multiple quan- tum wells	81
IV.	Sample structures of CdSe/ZnSe QW's.	90
V.	Parameters used for the theoretical calculations for CdSe/ZnSe QWs	102
VI.	Energy positions of the Γ_{1e} - Γ_{1hh} emissions and their pres- sure dependence obtained from CdSe/ZnSe SQW's.	106
VII.	Some physical properties of the cubic and hexagonal GaN	119
VIII.	Energy positions and pressure coefficients for the various PL emission structures from the cubic and hexagonal GaN . . .	127
IX.	Summary of built-in strains in all QW samples studied in this work	133

LIST OF FIGURES

Figure	Page
1. The crystal structure and the Brillouin zone for a zinc blende structure of a bulk semiconductor	2
2. Band structure for GaAs and GaP	3
3. Schematic representation of semiconductor quantum well structures.	5
4. Different types of QW structures.	8
5. Energy bandgap versus lattice constant for a variety of semiconductors	10
6. Schematic illustration of a layer with a larger lattice constant than the substrate for a strained layer.	11
7. The effects of a biaxial strain in zinc blende semiconductor band structures	13
8. Schematic representation of the effects of compressive strain on the band edges	24
9. Pressure dependence of the band edges of bulk GaAs	34
10. Band alignments for a Type-I quantum well before and after the crossover pressure, P_c	36
11. Experimental setup for the photoluminescence and photoluminescence excitation measurement	41
12. A comparison of three types of spectra for a GaAs semiconductor.	43
13. Photorefectance effect with above band gap illumination creating electron-hole pairs	46
14. Experimental setup for the photorefectance measurement	49
15. Experimental setup for the photomodulated transmission measurement	51

Figure	Page
16. A schematic of a diamond anvil cell for the application of the hydrostatic pressure on a sample	53
17. Schematic illustration of the GaAs/GaAs _{1-x} P _x MQW structure	59
18. Photoluminescence spectra of the GaAs/GaAs _{0.68} P _{0.32} MQW's at different pressures	60
19. Photoluminescence spectra of the GaAs/GaAs _{0.61} P _{0.39} MQW's at different pressures	61
20. Pressure dependence of various photoluminescence peaks observed in the GaAs/GaAs _{0.68} P _{0.32} SMQW	63
21. Pressure dependence of various photoluminescence peaks observed in the GaAs/GaAs _{0.61} P _{0.39} SMQW	64
22. Photoluminescence excitation (PLE) spectra taken at 10 K from the GaAs/GaAs _{0.61} P _{0.39} MQW	65
23. A schematic representation of the band-edge energies for the strained GaAs/GaAs _{1-x} P _x heterostructure under the condition of (001) tension	67
24. Band alignments of the strained GaAs/GaAs _{0.68} P _{0.32} quantum well before and after the crossover pressure, P_c	70
25. Schematic representation of InAs _x P _{1-x} /InP strained multiple quantum well (SMQW) structure.	80
26. Photoluminescence and excitation spectra at 10K for the InAs _x P _{1-x} /InP SMQW	82
27. Schematic representation of effects of the biaxial compressive strain on the InAs _x P _{1-x} layers	84
28. Comparison of PLE spectrum at 10K and PT spectrum at room temperature for the InAs _{0.6} P _{0.4} /InP SMQW.	86
29. Schematic illustration of the CdSe/ZnSe QW structure.	91
30. Schematic illustration of the CdSe/ZnSe submonolayer SQW structure.	92
31. Photoluminescence spectra taken from CdSe/ZnSe SQW's with different well widths.	95
32. Photoluminescence spectrum of the CdSe/ZnSe SQW sample with nominal submonolayer CdSe wells.	96

Figure	Page
33. Photoreflectance and photoluminescence spectra from the CdSe/ZnSe MQW sample.	98
34. Experimentally obtained energy positions of Γ_{1e} - Γ_{1hh} transitions of CdSe/ZnSe QWs as a function of CdSe well thickness.	99
35. Schematic representation of the effects of compressive strain on the CdSe band edges	101
36. Typical 10 K PL spectra taken at different pressures from the 2 ML CdSe/ZnSe SQW	104
37. Pressure dependence of the Γ_{1e} - Γ_{1hh} transitions in monolayer SQW samples.	105
38. PLE spectra obtained near the ZnSe band gap for 3 ML and 4 ML SQW samples.	109
39. Photoluminescence excitation (PLE) spectra obtained near the ZnSe band gap for 1ML SQW and MQW samples.	112
40. PLE spectra obtained from 3 ML and 4 ML CdSe/ZnSe SQWs.	114
41. Quantity $(4/3\pi)(E_m - E_g)^{3/2}$ as a function of the index number m for 3 and 4 ML CdSe/ZnSe SQW samples	116
42. Schematic representation of various transitions in a bulk semiconductor	121
43. PL spectra of the cubic GaN sample at several different pressures.	122
44. PL spectra of the GaN sample at different temperatures.	124
45. The variations of the energy positions for different PL emission structures of the GaN as a function of the hydrostatic pressure	125

CHAPTER I

INTRODUCTION

After Esaki and Tsu proposed new semiconductor microstructures in 1970 [1], a great amount of work has been done on these heterostructures in a wide range of material systems to investigate the underlying physics and to explore potential device applications. The development of epitaxial growth techniques, such as molecular beam epitaxy (MBE) and metal organic chemical vapor deposition (MOCVD), has allowed the growth of semiconductor epitaxial layered structures with very thin layers. The layer thickness can now be controlled to nearly an atomic scale (e.g. to a monolayer). These epitaxial growth techniques allow new artificial semiconductor microstructures such as quantum wells (QW's) and superlattices (SL's) which have exhibited new and interesting properties important in physics as well as in device applications. Before we discuss the semiconductor heterostructures in detail, a brief description of the crystal and band structures of bulk semiconductors will be given.

Electronic band structures

Bulk semiconductor

The crystal structure and its Brillouin zone for a zinc blende bulk semiconductor such as GaAs, GaP, or ZnSe, are shown in Fig. 1 [2]. Calculated electronic band structures along the $\langle 111 \rangle$ and $\langle 100 \rangle$ directions in bulk zinc blende GaAs and GaP are also shown in Fig. 2 [3]. The high symmetry points, which are of most importance in optical properties in semiconductors, are valleys in the conduction band at the zone center (Γ -point) and at the zone edge in the $\langle 100 \rangle$ direction

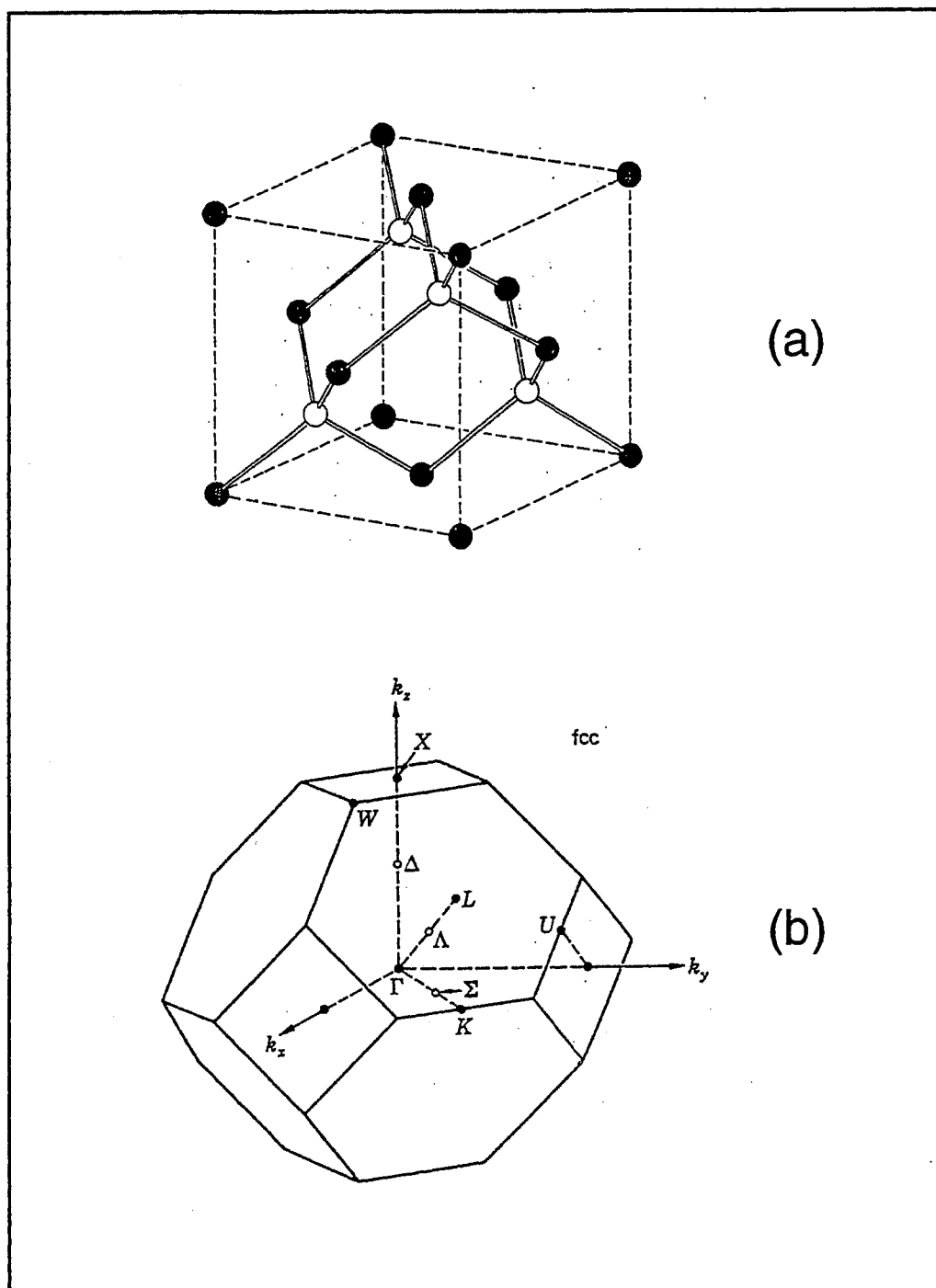


Figure 1. (a) The crystal structure and (b) the Brillouin zone for a zinc blende bulk semiconductor, such as GaAs, GaP, and ZnSe. The lattice constant a is the same as length of two monolayers (ML), $1 \text{ ML} = 0.5a$ (From [2]).

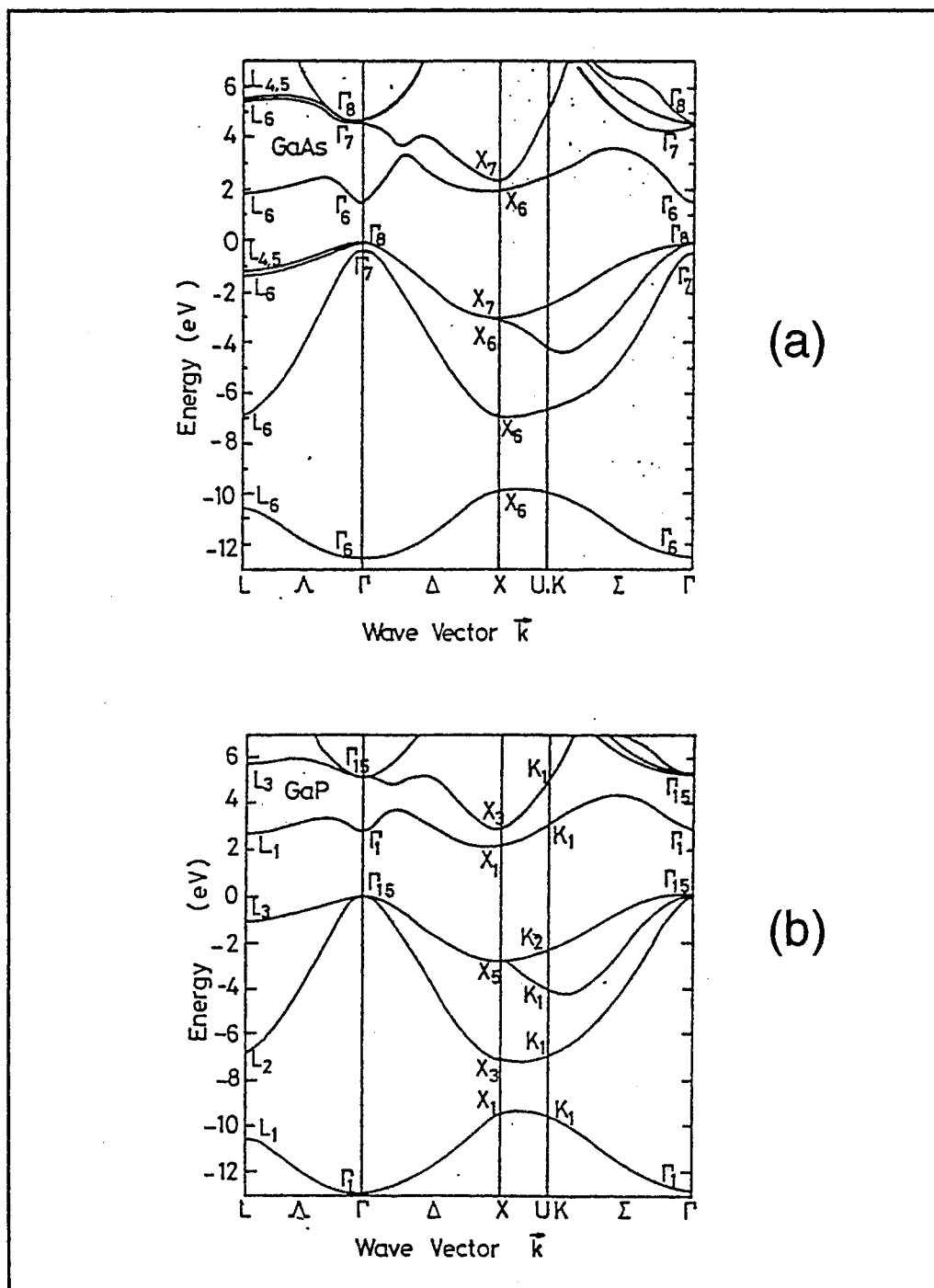


Figure 2. Band structure for (a) GaAs and (b) GaP. GaAs is a direct band gap semiconductor in which Γ -point is the lowest conduction band edge. GaP is an indirect band gap semiconductor in which conduction band edges at X-point are the lowest (From [3]).

(X -point) and in the $\langle 111 \rangle$ direction (L -point), that is,

$$\begin{aligned}
 \Gamma\text{-point} & : \vec{k} = (0, 0, 0) \frac{\pi}{2}, \\
 X\text{-point} & : \vec{k} = (1, 0, 0) \frac{\pi}{2}, \\
 L\text{-point} & : \vec{k} = (1, 1, 1) \frac{\pi}{2}.
 \end{aligned} \tag{1}$$

In most bulk semiconductors such as GaAs, the Γ -conduction band edge is located at the lowest among these conduction band edges (Fig. 2a). This kind of semiconductor material is called a *direct* band gap semiconductor. In some bulk semiconductors such as GaP, the X -point is located lower than any other conduction band edges becoming an *indirect* band gap semiconductor (Fig. 2b).

An important property of these three conduction band edges related to externally applied hydrostatic pressure is that they have different pressure coefficients. The Γ - and L -points have positive pressure coefficients while the X -point has a negative one. As pressure is increased, the Γ - and L -points move toward higher energy while the X -point moves toward lower energy. The different responses of these conduction band edges with hydrostatic pressure is a useful tool for determining important physical properties in a semiconductor, for example, band alignments in a QW structure.

Heterostructures

Semiconductor QW structures can be constructed by alternately growing two semiconducting materials with different band gap energies, that is, by embedding a single thin layer of material A (E_g^A) between thick layers of material B with a larger band gap, E_g^B , (Fig. 3b). In this case, the material B becomes the barrier while the material A becomes a well. A structure with a series of single QW's is known as a multiple quantum well (MQW) if the thickness of the barriers is large enough so that the resonant coupling of the wave functions between neighboring wells through the barrier is negligible. Then, the individual single QW's are isolated from others and the MQW structure shows the same characteristics as the single QW. However, if the thickness of the barriers is thin enough so that the well-to-well

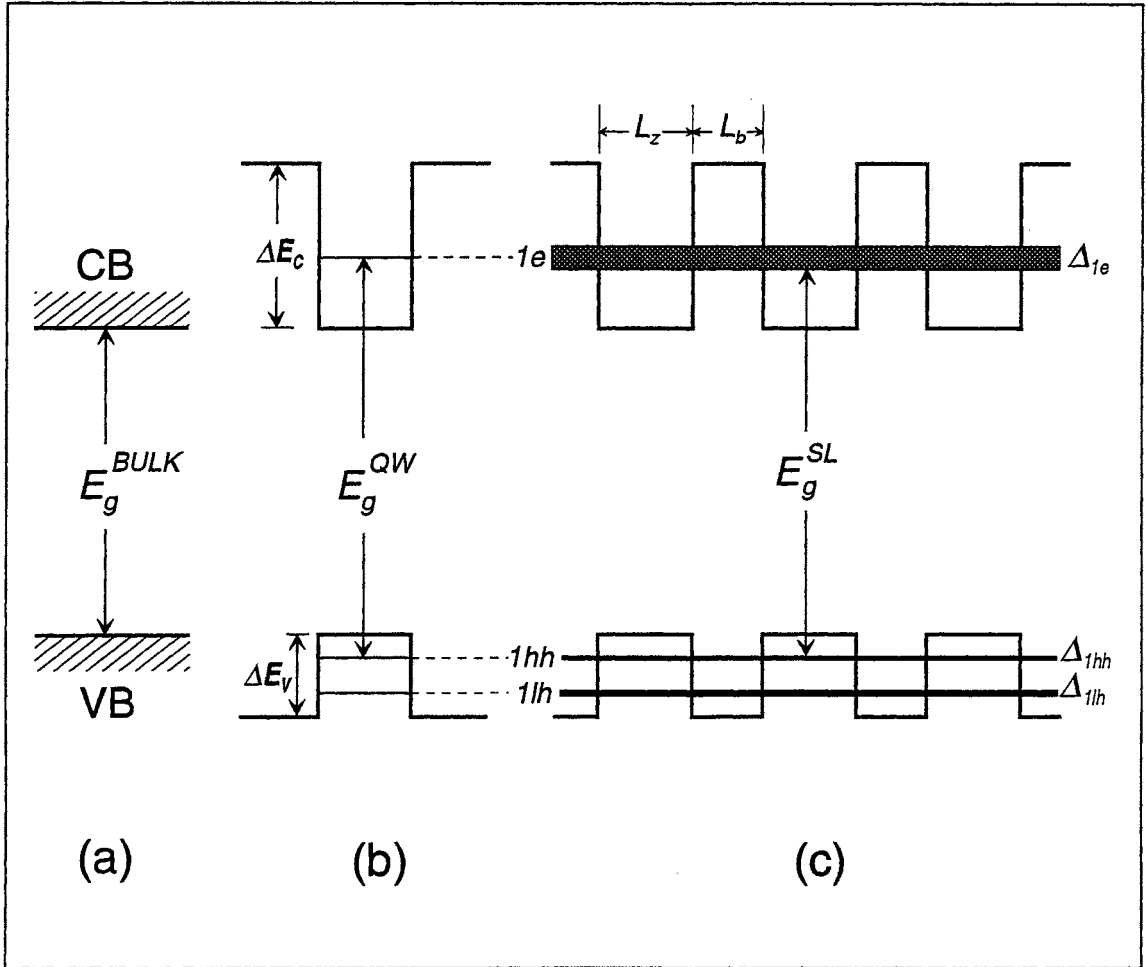


Figure 3. Schematic representation of semiconductor QW structures: (a) bulk, (b) single QW, and (c) SL. For simplicity, the Coulomb interaction (excitonic effect) is not included. ΔE_v (ΔE_c) denotes a band offset for the valence (conduction) band. The absorption edges for each structure denoted as E_g^{BULK} , $E_g^{QW} = E_g^{BULK} + E_{1e} + E_{1hh}$ and $E_g^{SL} = E_g^{QW} - 0.5(\Delta_{1e} + \Delta_{1hh})$ for bulk, QW and SL, respectively. Here $1e$, $1hh$ and $1lh$ are respectively the first confined electron, heavy-hole and light-hole levels and their corresponding confinement energies are E_{1e} , E_{1hh} and E_{1lh} . Their miniband widths are denoted as Δ_{1e} , Δ_{1hh} and Δ_{1lh} . The sum of the thicknesses of a well and a barrier is defined as a period of a MQW structure, $d = L_z + L_b$.

coupling of wave functions can occur, this structure is called a superlattice (SL) (Fig. 3c). In this case, the well-to-well coupling of the wave functions results in the formation of minibands. The SL structure exhibits novel properties not seen in uncoupled QW's.

The resulting QW structure, in general, forms wells in both the conduction band and the valence band in material *A*, while the material *B* becomes a barrier for both bands (Fig. 3b). Thus, both carriers (electrons and holes) are confined in the material *A*. This confinement of carriers in a well results in the well-known quantum mechanical discrete energy levels. The number of the confinement levels and their energies in a QW depend on the well thickness and the barrier height. The quantum confinement energy levels and their wave functions can be easily calculated using the envelope function approximations [4-6]. In an infinitely deep quantum well, the energy levels and wave functions can be expressed as:

$$E_n = \frac{\hbar^2}{2m} \left(\frac{n\pi}{L_z} \right)^2 \quad n = 1, 2, 3, \dots \quad (2)$$

and

$$\psi_n = A \cos \frac{n\pi z}{L_z}. \quad (3)$$

Here L_z denotes the well width of the QW. For a finite well with a potential barrier V_0 , the confinement energy levels are the solution of the transcendental equations with boundary conditions at $z = \pm \frac{L}{2}$:

$$\begin{cases} k_w \tan \left(k_w \frac{L}{2} \right) = k_b & \text{for even states,} \\ k_w \cot \left(k_w \frac{L}{2} \right) = -k_b & \text{for odd states,} \end{cases} \quad (4)$$

with wavevectors k_w and k_b in the well and barrier:

$$\begin{cases} k_w = \sqrt{\frac{2m^*}{\hbar^2} (E + V_0)}, \\ \text{and} \\ k_b = \sqrt{\frac{2m^*}{\hbar^2} E}. \end{cases} \quad (5)$$

Therefore, from these equations we can calculate the confinement energies in a QW which depend on L_z and V_0 .

Band offsets in QW structures

The difference in energies between the bands, that is the potential barrier height in a well due to the spatial variation in potential, is called the band offset. These band offsets are denoted by ΔE_c and ΔE_v , for the conduction and the valence band, respectively. For a semiconductor heterojunction, one usually defines the fraction $Q_v = \Delta E_v / \Delta E_g$ and $Q_c = \Delta E_c / \Delta E_g$, which are respectively known as the valence and conduction band offset ratios. Here, ΔE_g is the difference between band gap energies of the constituent semiconductor materials, $\Delta E_g = E_g^B - E_g^A$.

Depending on the band alignment between the two materials, meaning the sign of the band offsets in conduction and valence bands, the QW structure is classified as a Type-I or a Type-II. Fig. 4 shows a schematic representation of these two types of QW structures. In a Type-I QW, both electrons and holes are confined in the same layer (here material A) and thus electrons excited into the conduction band recombine with the holes in the valence band resulting in a direct transition. In a Type-II QW, on the other hand, electrons and holes are confined in different layers which are spatially separated.

Since the band offset in a heterostructure can be critical for device performance [7] in which carrier transfer is the major factor, the determination of the band offset in the heterostructure is very important for both fundamental study and device applications. In spite of the importance of the band offset values in heterostructures, the values obtained using different methods do not agree in many cases. These discrepancies might be due to the fact that most techniques for determining band offsets are indirect methods such as the use of theoretical fittings to spectral results [8]. A new pressure-optical technique has been discovered to be a direct method to determine the band offset in QW structures. In this technique, a hydrostatic pressure is applied to samples using a diamond anvil pressure cell and photoluminescence is measured. This technique utilizes the different pressure dependent characteristics of band edges (Γ and X) in semiconductors. This technique will be described in detail in later chapters.

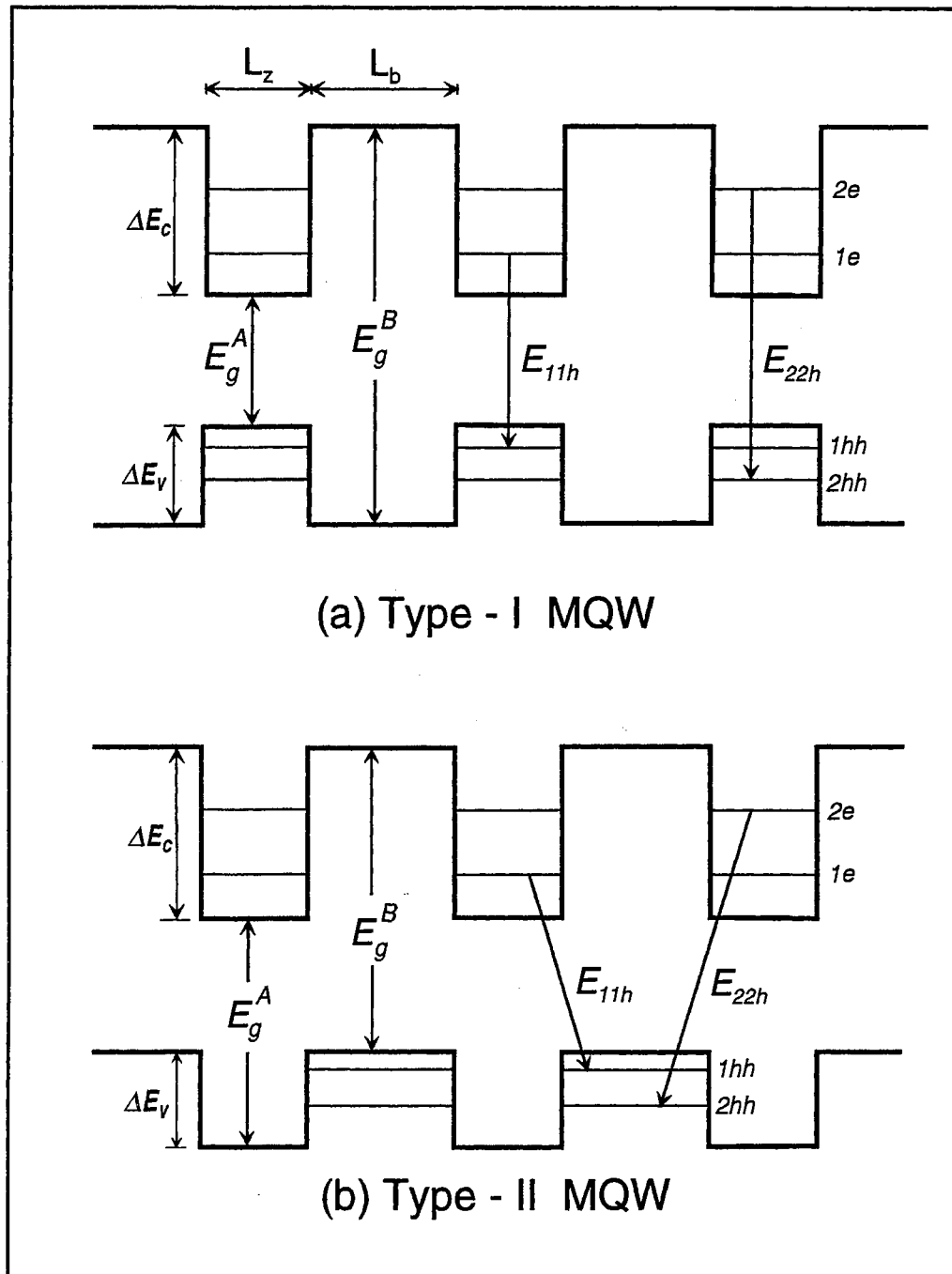


Figure 4. Different types of QW structures, (a) Type-I and (b) Type-II. Both electrons and holes are confined in well material A in the Type-I QW. For the Type-II QW, electrons are confined in material A, while holes are confined in the material B. E_{11h} is the energy of an interband transition between lowest confined electron subband ($1e$) and lowest confined heavy-hole subband ($1hh$). Here, the only heavy-hole subbands in the conduction band are shown and the excitonic effect is not included.

Strained layer semiconductor heterostructures

During the last decade, tremendous developments have occurred in the field of semiconductor heterojunctions and their applications in electronic devices. The most extensively studied heterostructures are lattice matched systems such as GaAs/ $\text{Al}_x\text{Ga}_{1-x}\text{As}$ QW structures [9]. For lattice matched systems, however, device applications are limited due to the few choices of possible combination of heterostructure materials. As seen in Fig. 5, there are only a few combinations of materials for lattice matched heterostructures, limiting the range of device applications. If lattice mismatched systems with large strain can be grown, different material combinations become possible allowing flexible band gap tailoring.

The great improvement of epitaxial growth techniques with precise layer control nearly on the atomic scale, allows high quality (device quality in some cases) heterostructures to be grown, not only for lattice matched but also for lattice mismatched systems. For example, highly strained heterostructures, such as ZnSe/CdSe QW structures with about 6.8 % of lattice mismatch, have been successfully grown [11,12].

Accommodation of lattice mismatched heterostructures

Strained layers can be grown pseudomorphically on a substrate with their thickness below a certain value (called the critical thickness). When the thickness of an epitaxial layer grown on a substrate exceeds the critical value, both elastic strain and misfit dislocations will result. Fig. 6 illustrates a simple concept of the growth of a single strained layer. If the lattice mismatch between an epilayer and a substrate is small and the epilayer is sufficiently thin, the epilayer will be accommodated with homogeneous in-plane elastic strain by keeping the same lattice constant of the substrate throughout the structure (Fig. 6b). When the epilayer exceeds the critical thickness, misfit dislocations are formed at or near the heterojunction because the energy associated with the homogeneous strain exceeds the energy sustaining the crystal bonds (Fig. 6c). These strain-relaxed

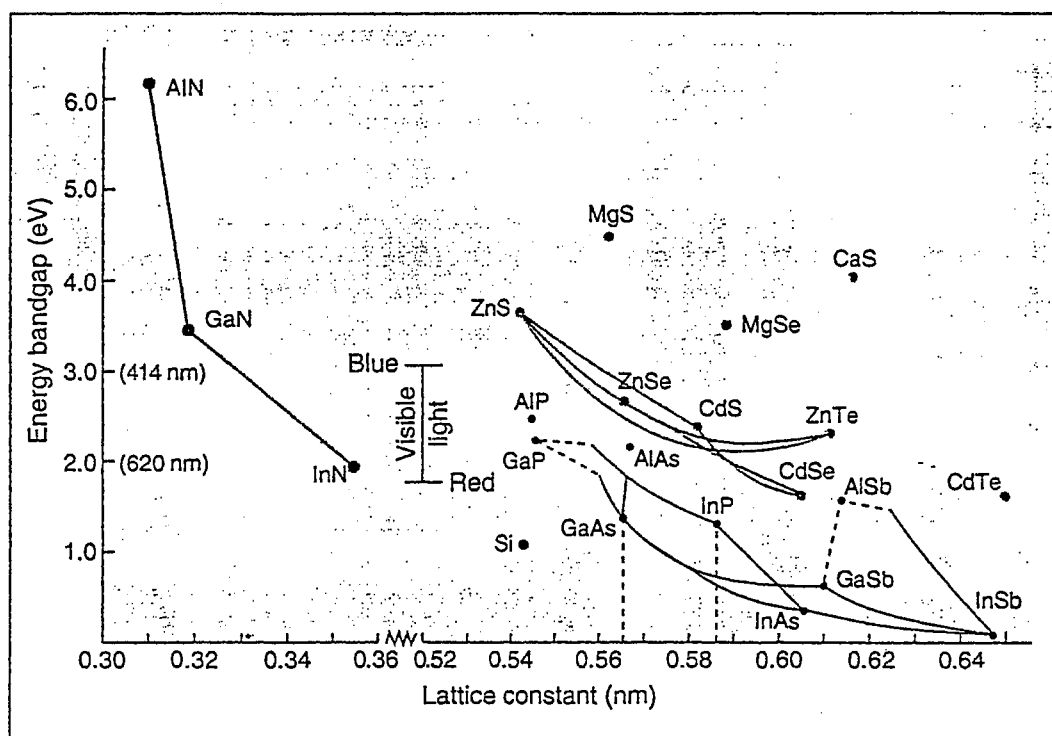


Figure 5. Energy bandgap versus lattice constant for a variety of semiconductors. The lines that connect points for binary compounds represent values of intermediate ternary compounds; for example, GaAsP characteristics fall along the line connecting GaP with GaAs. The shown nitride based materials have a hexagonal crystal structure (after [10])

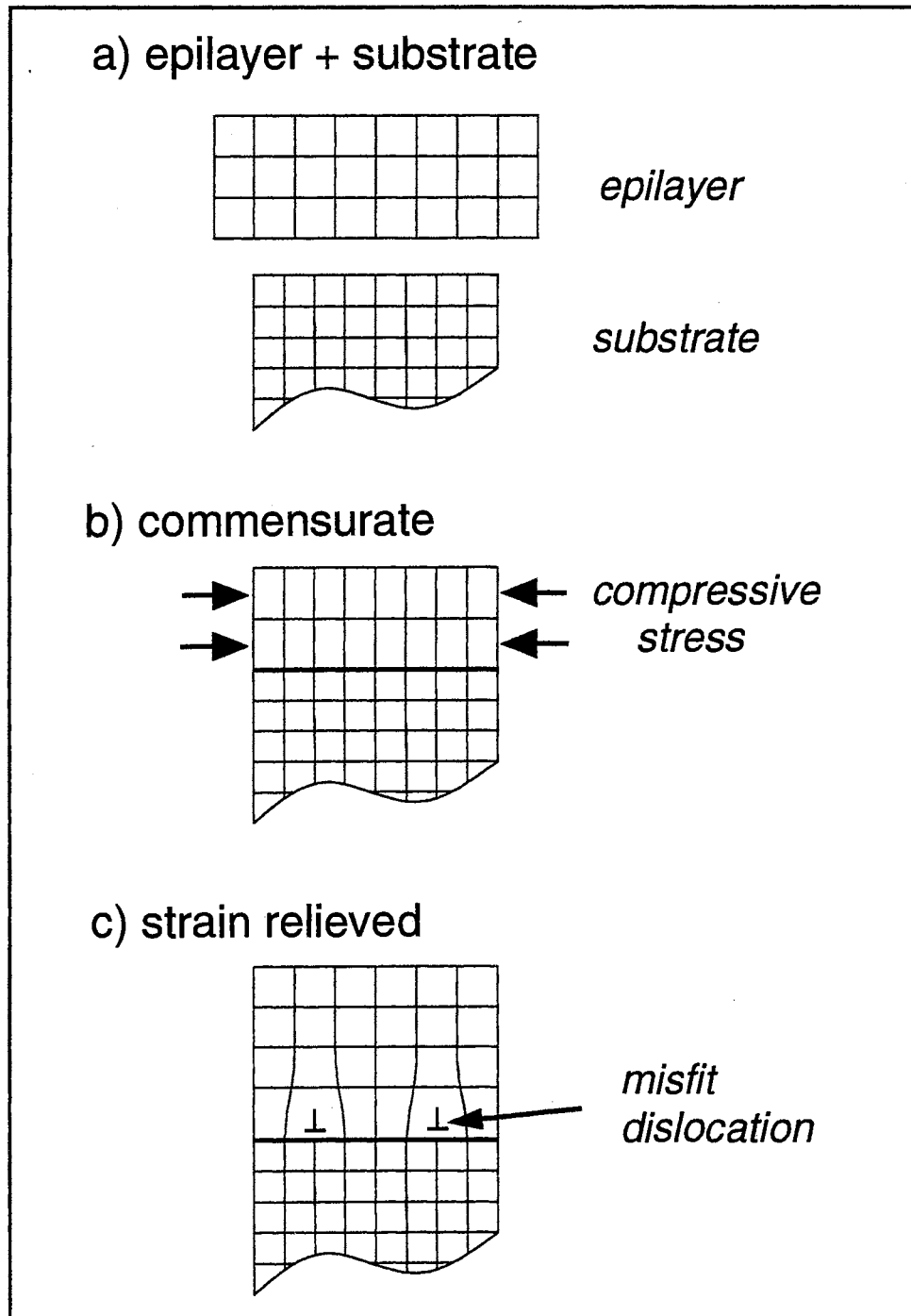


Figure 6. Schematic illustration of a layer with a larger lattice constant than the substrate for (a) an isolated layer and a substrate in equilibrium, (b) commensurately grown compressively strained-layer on a substrate, and (c) strain-relaxed layer on a substrate. Dislocations are formed at or near the interface.

misfit dislocations will relax the lattice constant of the epilayer to its bulk value. With further growth, the epilayer will be completely relaxed resulting in a free standing situation (in equilibrium) where the lattice constant of the epilayer will be the same as that of the bulk.

For the strained system, the lattice mismatch induced in-plane strain ε is defined as

$$\varepsilon = \frac{a_{\perp} - a_0}{a_0} \quad (6)$$

where a_{\perp} and a_0 are strained and unstrained lattice constants of the epilayer, respectively.

Effects of strain on the band structures of heterostructures

The effects of built-in strain on a strained epilayer (here, limited to Γ -point) with a zinc blende structure are: (1) the changes in the band gap, (2) the strain-induced splitting of the top of valence band at the Γ -point into the heavy-hole and light-hole band edges by reducing the degeneracy. In Fig. 7, the effects of the strain on the band structure are shown near $k = 0$ for (a) biaxial compressive strain and (c) biaxial tensile strain. The biaxial compressive (tensile) strain on the epilayer is caused by its larger (smaller) equilibrium lattice constant than that of the substrate. For comparison, the band structure for an unstrained system is also shown in Fig. 7b. These strain-induced changes in the energy band gap can be accessible through the greater freedom in choice of materials and alloy compositions [13]. The properties of the whole heterostructure, especially in QW's, may be changed depending on the type and amount of strain. Sometimes, the QW structure becomes Type-II for one or both hole bands. The light-hole band can also be located above the heavy-hole band for the tensile strain case (Fig. 7c).

This homogeneous strain can change the electronic properties in the strained layer and provides a large flexibility in device design. Thus, the strain effects on the heterostructure microstructures (QW and SL structures) can offer important benefits in device applications utilizing the changes in the electronic and resultant

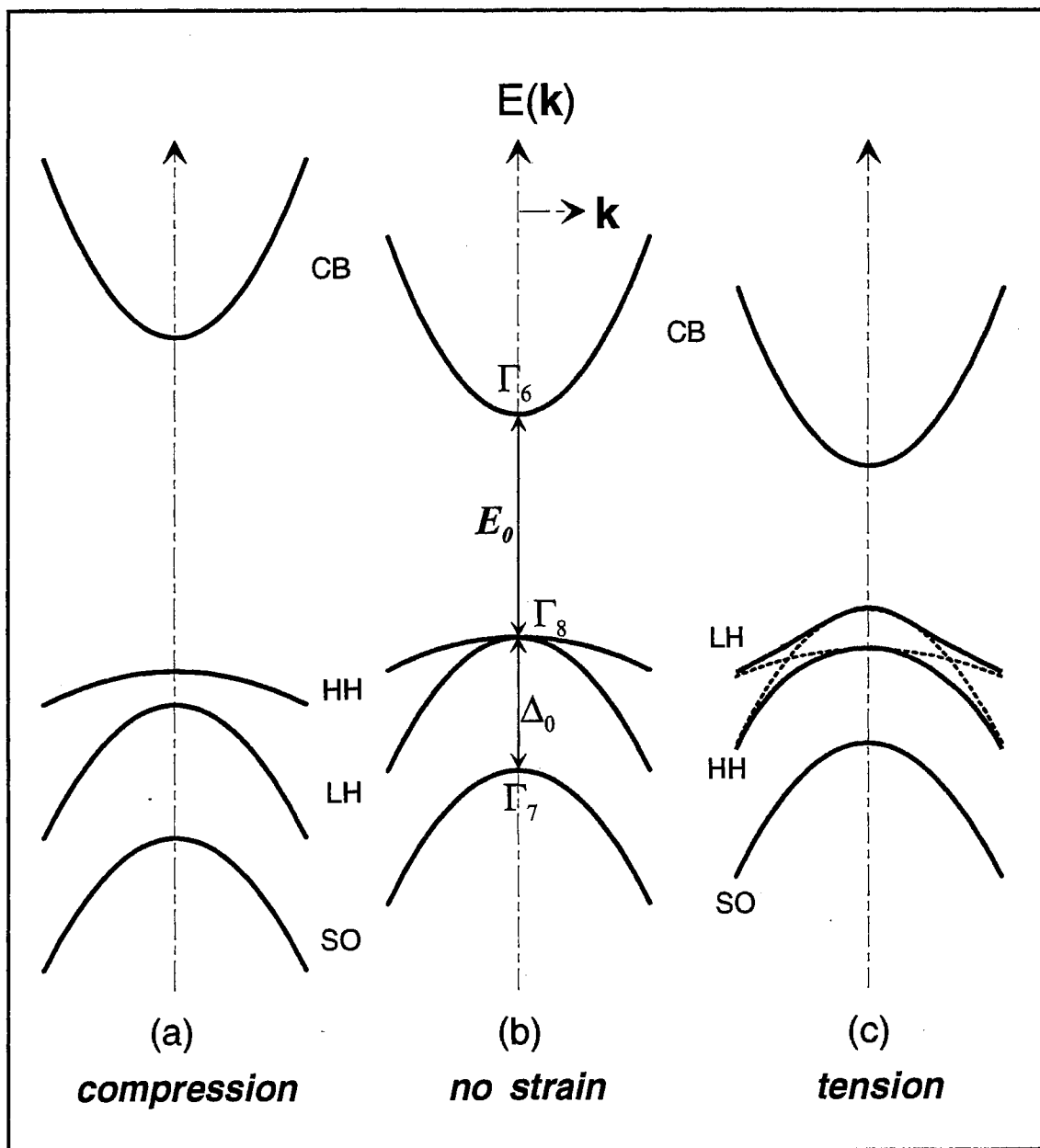


Figure 7. The effects of a biaxial strain in zinc blende semiconductor band structures near $k = 0$ for (a) biaxial compressive strain, (b) no strain, and (c) biaxial tensile strain. HH, LH, and SO represent heavy-hole, light-hole, and spin-orbit split-off bands, respectively. In (b), the energy difference between the Γ_6 (bottom of the conduction band) and Γ_8 (top of the valence band) is denoted as E_0 , the fundamental direct gap. Δ_0 denotes the spin-orbit splitting of the top of the valence band Γ_8 .

transport properties. In the last few years, a vast number of studies have been reported demonstrating the great advantage of the strained system in many devices, such as photodetectors, high speed transistors, QW lasers, etc. In photodetectors utilizing strain effects, appropriately designed strained layers modify the band gap of the photodetector and thus provide for operation at the desired optical frequency or bandwidth [14–16]. The emission wavelength of a strained QW laser structure can also be modified by using a strained layer as the active region and by modifying the band gap of the active material utilizing the strain effect [17]. It was also demonstrated that the accumulation of carriers (electrons and holes) due to the strain induced increment of the band offset and the change of the hole transport properties by the splitting of the heavy-hole and light-hole bands could improve the performance in fast electronic devices such as modulation-doped field effect transistors (MODFET's), heterojunction bipolar transistors (HBT's), and resonant tunneling structures [7,17].

Motivation of this study

In this thesis, optical properties of strained heterostructures, including III-V and II-VI compounds, are investigated using various optical spectroscopic techniques such as photoluminescence (PL), photoluminescence excitation (PLE), photorefectance (PR), and photomodulated transmission (PT) spectroscopy. The effect of the hydrostatic pressure on the optical transitions using a high pressure diamond anvil cell is also investigated for most of the samples. In chapter II, strain effects on the semiconductor heterostructure are discussed. In chapter III, the experimental techniques employed in this study are described. In chapter IV, GaAsP/GaAs strained multiple quantum well (SMQW) structures are extensively investigated giving several valuable results such as the band offset ratio in the heterojunction and the origin of the optical transitions. The interband transitions in the InAsP/InP SMQW's are discussed in chapter V. Chapter VI shows the results of an intensive study for different QW structures of highly strained CdSe/ZnSe

QW samples. The critical layer thickness of the CdSe well layer in the QW structure is estimated from results of the pressure dependent PL data. In chapter VII, the first pressure dependent PL study on bulk GaN in cubic structure is given. GaN is very interesting because of its large band gap energy which can be used for device applications in the UV-blue region. Finally, chapter VIII will conclude this thesis with a summary of results.

The GaAsP/GaAs strained QW structure has been studied due to the potential of its wide application in devices such as diode lasers and MODFETs [18–22]. Despite its crucial importance in device design, however, the band offset at the heterojunction is not well known in GaAsP/GaAs material systems. The application of the hydrostatic pressures on the sample can be used to determine the band offset ratio at the heterojunction by utilizing the different pressure coefficients of the conduction band edges. The observation of the pressure-induced band-edge-crossover in the GaAsP/GaAs strained MQW allowed the determination of the band offset.

Due to the strong demand for fiber optical communication in the range of 1.3–1.5 μm , materials using phosphorus (such as InAsP/InP heterostructures) would be very attractive for devices such as optical modulators. Understanding the physical properties of these material systems, such as interband transitions, and band alignment (band offset), is therefore very important for both scientific aspects and device applications.

Another strong demand in material science is developing devices in the UV and blue range for under water communications and for light emitting devices. Materials based on ZnSe and wide bandgap nitrides have been extensively studied because their band gap energies are in this spectral region. For instance, the band gap energies are at about 2.82 eV and 3.4 eV for ZnSe and wurtzite GaN, respectively. In the last few years, a great amount of work in this area has been done around the world resulting in the development of the blue-green lasers. These lasers are mainly based upon the ZnSe material system which includes materials, such as bulk ZnSe, ZnSe/CdSe and ZnSe/ZnS. Very recently, GaN based materials

have been studied for their potential use in device applications due to their high band gap energy. Therefore, the characterization of these new material systems is essential in evaluating their potential for device applications.

CHAPTER II

ELECTRONIC PROPERTIES OF STRAINED HETEROSTRUCTURES

In this chapter, the effects of strain on semiconductor band structures described by the deformation potential theory will be followed by a brief summary of the envelope function approximation (EFA) for calculations of confinement energy levels in a QW. The hydrostatic pressure technique to determine band offsets in a heterostructure is then discussed along with the pressure effect on the band edges.

Strain effects on band structures

Effects of homogeneous strain on electronic energy levels

The introduction of homogeneous strain in a solid changes the lattice parameter and crystal symmetry of the material thereby producing changes in the energy band gap and a splitting of the bands caused by a reduction of crystal symmetry. In order to fully describe the electronic energy levels of strained QW's and SLs, it is important to have information about the effects of strain on the properties of the materials. A great amount of work has been done on these strain effects. In this section, a brief summary based on Pollak's review will be presented [23]. The strain induced changes in band extrema will be discussed for the zinc blende structure only because this is the structure of the samples used in this study. The discussion will also be limited to the biaxial strain in the (001) plane (uniaxial strain along [001]), the conduction and valence bands extrema at $\vec{k} = 0$ (Γ -point), and the conduction band extrema at $\vec{k} \neq 0$ (X -point).

Critical Point Near $\vec{k} = 0$ (Γ -point) Without any strain or spin-orbit splitting, the valence band edge at the center of the Brillouin zone ($\vec{k} = 0$) in zinc

blende materials is a six-fold degenerate multiplet with orbital symmetry Γ_{15} . The spin-orbit interaction will lift this six-fold degenerate multiplet into a four-fold degenerate $P_{3/2}$ multiplet (Γ_8 , hole bands including heavy-hole and light-hole bands; $J = \frac{3}{2}$, $M_J = \pm\frac{3}{2}, \pm\frac{1}{2}$) and a two-fold degenerate $P_{1/2}$ multiplet (Γ_7 , spin-orbit split-off band; $J = \frac{1}{2}$, $M_J = \pm\frac{1}{2}$). Both multiplets include a doubly degenerate state due to the spin.

The strain effect on semiconductor materials can be divided by two components as shown in Fig. 7: (1) hydrostatic component (or isotropic term), which does not change any crystal symmetry but produces changes in the energy band gap, and (2) shear component (or anisotropic term), which in general reduces the crystal symmetry resulting in the splitting of the top of valence band and the $\vec{k} \neq 0$ conduction band edges. The shear component splits the four-fold degenerate state ($J = \frac{3}{2}$ multiplet band) into two doubly degenerate states as $J = 3/2$ (heavy-hole) and $J = 1/2$ (light-hole).

For a layer with a uniaxial compressive strain (Fig. 7a), the heavy-hole band edge moves to higher energies than the light-hole band while the light-hole band is higher than the heavy-hole band in the case of a biaxial tensile strain (Fig. 7c). In the latter case, the band mixing between heavy-hole and light-hole bands will be expected at $\vec{k} \neq 0$ due to the different effective mass for heavy-hole and light-hole bands.

In order to characterize the effect of the strain on the semiconductor band structure, we start with the strain Hamiltonian H_ϵ for a p -like multiplet which can be expressed as [24]:

$$H_\epsilon = H_\epsilon^{(1)} + H_\epsilon^{(2)}, \quad (7)$$

where $H_\epsilon^{(1)}$ is the orbital strain Hamiltonian and $H_\epsilon^{(2)}$ is the strain-dependent spin-orbit Hamiltonian.

The orbital strain Hamiltonian $H_\epsilon^{(1)}$ of the valence bands can be described as [24]:

$$\begin{aligned} H_\epsilon^{(1)} = & -\mathbf{a}_1 (\epsilon_{xx} + \epsilon_{yy} + \epsilon_{zz}) \\ & -3\mathbf{b}_1 \left[\left(L_x^2 - \frac{1}{3} L^2 \right) \epsilon_{xx} + c.p. \right] \\ & -\sqrt{3}\mathbf{d}_1 [(L_x L_y + L_y L_x) \epsilon_{xy} + c.p.]. \end{aligned} \quad (8)$$

In Eq.(8), ϵ_{ij} are the components of the strain tensor, L is the angular momentum operator and $c.p.$ represents the cyclic permutations with respect to x, y, z . The \mathbf{a}_1 is absolute hydrostatic deformation potential which represents the intraband (absolute) shift of the orbital valence bands due to the hydrostatic component of the strain. The \mathbf{b}_1 and \mathbf{d}_1 are orbital uniaxial deformation potentials appropriate to strains of tetragonal and rhombohedral symmetries, respectively.

The strain-dependent spin-orbit Hamiltonian can be expressed as [24]:

$$\begin{aligned} H_\epsilon^{(2)} = & -\mathbf{a}_2 (\vec{L} \cdot \vec{\sigma}) (\epsilon_{xx} + \epsilon_{yy} + \epsilon_{zz}) \\ & -3\mathbf{b}_2 \left[\left(L_x \sigma_x + \frac{1}{3} \vec{L} \cdot \vec{\sigma} \right) \epsilon_{xx} + c.p. \right] \\ & -\sqrt{3}\mathbf{d}_2 [(L_x \sigma_y + L_y \sigma_x) \epsilon_{xy} + c.p.], \end{aligned} \quad (9)$$

where \mathbf{a}_2 , \mathbf{b}_2 , and \mathbf{d}_2 represent additional deformation potentials which describe the effects of a strain on the spin-orbit interaction, and $\vec{\sigma}$ is the Pauli matrix vector.

Since the conduction band minima for the zinc blende type solid is an antibonding s -state with symmetry Γ_2 , the strain-induced hydrostatic shift of this band minima can be given by:

$$H_\epsilon^{(c)} = -\mathbf{a}_c (\epsilon_{xx} + \epsilon_{yy} + \epsilon_{zz}), \quad (10)$$

where \mathbf{a}_c is the interband (absolute) hydrostatic deformation potential of the lowest conduction band.

For the structure of the conduction and valence bands near $\vec{k} = 0$, Kane's $\vec{k} \cdot \vec{p}$ perturbation approach can be used where the Hamiltonian is given by [25]:

$$H_k = \left(-\frac{\hbar^2}{2m} \right) \nabla^2 + V(r) + \left(\frac{\hbar^2 k}{2m} \right) + \left(\frac{\hbar}{m} \right) \vec{k} \cdot \vec{p}. \quad (11)$$

Therefore, the total Hamiltonian can be written as:

$$H = H_k + H_{so} + H_\epsilon^{(c)} + H_\epsilon^{(1)} + H_\epsilon^{(2)}, \quad (12)$$

where H_{so} is the effect of the spin-orbit interaction.

For biaxial strain in the (001) plane, we have

$$\begin{aligned}\varepsilon_{xx} = \varepsilon_{yy} = \varepsilon &= \frac{a_{\perp} - a_0}{a_0}, \\ \varepsilon_{zz} &= -\frac{2C_{12}}{C_{11}}\varepsilon, \\ \varepsilon_{xy} = \varepsilon_{yz} = \varepsilon_{zx} &= 0,\end{aligned}\tag{13}$$

where a_{\perp} is the in-plane lattice constant of the epilayer, a_0 the lattice constant of the epilayer without strain, and C_{ij} are elastic stiffness constants. For an epilayer coherently grown on a substrate (or buffer layer), the in-plane lattice constant is the same as that of the substrate, $a_{\perp} = a_{substrate}$. With equations (13) for this direction of the strain, equations (8) and (9) for the strain Hamiltonian reduce to

$$\begin{aligned}H_{\varepsilon}^{(1)} &= -\mathbf{a}_1 \left(2 + \frac{2C_{12}}{C_{11}}\right) \varepsilon \\ &= -3\mathbf{b}_1 \left(1 - \frac{2C_{12}}{C_{11}}\right) \left(L_z^2 - \frac{1}{3}L^2\right) \varepsilon,\end{aligned}\tag{14}$$

$$\begin{aligned}H_{\varepsilon}^{(2)} &= -\mathbf{a}_2 \left(2 + \frac{2C_{12}}{C_{11}}\right) (\vec{L} \cdot \vec{\sigma}) \varepsilon \\ &= -3\mathbf{b}_2 \left(1 - \frac{2C_{12}}{C_{11}}\right) \left((L_z \sigma_z) - \frac{1}{3}\vec{L} \cdot \vec{\sigma}\right) \varepsilon.\end{aligned}\tag{15}$$

Now we want find energy eigenvalues of the Hamiltonian for the transition energy with uniaxial strain between conduction band and valence bands. First, we need to find the eigenfunctions of the Hamiltonian.

When a perturbation theory is used, the choice of the set of unperturbed wave functions is very important. If we can choose a set of basis functions so that the unperturbed term in the Hamiltonian is already diagonalized, the treatment will be much simpler. Hence, if the energy changes produced by the $H_k + H_{\varepsilon}$ are much smaller than the spin-orbit splitting, then the most convenient set of basis functions for a perturbation expansion are those that makes H_{so} diagonal. Conversely, if the spin-orbit splitting is small compared with the energy changes produced by the other terms, functions that make $H_k + H_{\varepsilon}$ diagonal are the most convenient set of unperturbed wave functions for the problem. Here, variations of spin-orbit splitting with \vec{k} are neglected.

We now start with wave functions that make H_{so} diagonal. These are functions that have the same transformation properties as the eigenfunctions of the

total angular momentum operators $\vec{J} (= \vec{L} + \vec{S})$, i.e., $|J, M_J\rangle$. These wave functions are for s -like conduction band (Γ_1) [25]:

$$\begin{aligned} \left| \frac{1}{2}, \frac{1}{2} \right\rangle_c &= |S \uparrow\rangle, \\ \left| \frac{1}{2}, -\frac{1}{2} \right\rangle_c &= |S \downarrow\rangle, \end{aligned} \quad (16)$$

while for the p -like valence bands (Γ_8, Γ_7) the wave functions can be written as:

$$\begin{aligned} \left| \frac{3}{2}, \frac{3}{2} \right\rangle_v &= \frac{1}{\sqrt{2}} |(X + iY) \uparrow\rangle, \\ \left| \frac{3}{2}, \frac{1}{2} \right\rangle_v &= \frac{1}{\sqrt{6}} |(X + iY) \downarrow\rangle - \sqrt{\frac{2}{3}} |Z \uparrow\rangle, \\ \left| \frac{3}{2}, -\frac{1}{2} \right\rangle_v &= \frac{1}{\sqrt{6}} |(X - iY) \uparrow\rangle - \sqrt{\frac{2}{3}} |Z \downarrow\rangle, \\ \left| \frac{3}{2}, -\frac{3}{2} \right\rangle_v &= -\frac{1}{\sqrt{2}} |(X - iY) \downarrow\rangle, \\ \left| \frac{1}{2}, \frac{1}{2} \right\rangle_v &= \frac{1}{\sqrt{3}} |(X + iY) \downarrow\rangle + \frac{1}{\sqrt{3}} |Z \uparrow\rangle, \\ \left| \frac{1}{2}, -\frac{1}{2} \right\rangle_v &= \frac{1}{\sqrt{3}} |(X - iY) \uparrow\rangle - \frac{1}{\sqrt{3}} |Z \downarrow\rangle, \end{aligned} \quad (17)$$

where the arrows \uparrow and \downarrow represent spin-up and spin-down, respectively.

In many zinc blende materials, the conduction band is close to the valence bands and they are far away from all other bands. Therefore, we shall diagonalize the Hamiltonian exactly for sets of conduction band and valence bands and treat the coupling between this group of bands with the rest of the bands as a second order perturbation. A detailed account of the Kane model is given in Ref. [25].

Taking the wave functions in Eq. (17), the Hamiltonian matrix of Eqs. (14) and (15) becomes a simple form at $\vec{k} = 0$ for a strain with a uniaxial component along [100]:

$$\begin{array}{cccc} \left| \frac{1}{2}, \pm \frac{1}{2} \right\rangle_c & \left| \frac{3}{2}, \pm \frac{3}{2} \right\rangle_v & \left| \frac{3}{2}, \pm \frac{1}{2} \right\rangle_v & \left| \frac{1}{2}, \pm \frac{1}{2} \right\rangle_v \\ \left| \frac{1}{2}, \pm \frac{1}{2} \right\rangle_c & E_0 + \delta E_{H,c} & 0 & 0 \\ \left| \frac{3}{2}, \pm \frac{3}{2} \right\rangle_v & 0 & -\delta E_{H,v} - \delta E_S & 0 \\ \left| \frac{3}{2}, \pm \frac{1}{2} \right\rangle_v & 0 & 0 & -\delta E_{H,v} + \delta E_S \quad \pm \sqrt{2} \delta E'_S \\ \left| \frac{1}{2}, \pm \frac{1}{2} \right\rangle_v & 0 & 0 & \pm \sqrt{2} \delta E'_S \quad -\Delta_0 - \delta E'_{H,v} \end{array} \quad (18)$$

where E_0 is the band gap energy and Δ_0 is spin-orbit split-off band energy of the material without strain. The energy $E = 0$ is set at the top of valence band in the unstrained system. In Eq. (18), the δE 's are defined as:

$$\begin{aligned}
\delta E_{H,c} &= \mathbf{a}_c \left(2 - \frac{2C_{12}}{C_{11}} \right) \varepsilon = \mathbf{a}_c (2 - \lambda) \varepsilon, \\
\delta E_{H,v} &= (\mathbf{a}_1 + \mathbf{a}_2) (2 - \lambda) \varepsilon = \mathbf{a} (2 - \lambda) \varepsilon, \\
\delta E'_{H,v} &= (\mathbf{a}_1 - 2\mathbf{a}_2) (2 - \lambda) \varepsilon = \mathbf{a}' (2 - \lambda) \varepsilon, \\
\delta E_S &= -(\mathbf{b}_1 + 2\mathbf{b}_2) [1 + \lambda] \varepsilon = -\mathbf{b} [1 + \lambda] \varepsilon, \\
\delta E'_S &= (\mathbf{b}_1 - \mathbf{b}_2) [1 + \lambda] \varepsilon = -\mathbf{b}' [1 + \lambda] \varepsilon,
\end{aligned} \tag{19}$$

with

$$\lambda = 2C_{12}/C_{11},$$

where \mathbf{a} and \mathbf{a}' are interband hydrostatic deformation potentials, \mathbf{b} and \mathbf{b}' are shear deformation potentials.

Thus, the effects of the strain is to create a hydrostatic shift and to split the degeneracy of the top of the valence band, Γ_8 , into the v_1 (heavy-hole) and v_2 (light-hole) bands which correspond to the $|\frac{3}{2}, \pm\frac{3}{2}\rangle$ state and $|\frac{3}{2}, \pm\frac{1}{2}\rangle$ state, respectively. Since the heavy-hole band does not couple to either the Γ_8 light-hole band or the Γ_7 spin-orbit split band at $k = 0$, it has a linear stress dependence while the states with $M_J = \pm\frac{1}{2}$ couple with each other giving non-linear stress-dependence caused by the off-diagonal terms in Eq. (18).

Then, the strain dependent eigenfunctions for the $\vec{k} = 0$ valence bands can be written as [26]:

$$\begin{aligned}
|v_1\rangle &= |\frac{3}{2}, \pm\frac{3}{2}\rangle, \\
|v_2\rangle &= \alpha |\frac{3}{2}, \pm\frac{1}{2}\rangle + \beta |\frac{1}{2}, \pm\frac{1}{2}\rangle, \\
|v_3\rangle &= -\beta |\frac{3}{2}, \pm\frac{1}{2}\rangle + \alpha |\frac{1}{2}, \pm\frac{1}{2}\rangle,
\end{aligned} \tag{20}$$

where

$$\begin{aligned}
\alpha &= [2\sqrt{2} |\delta E_S|] / q_0, \\
\beta &= (m_0 - n_0) (\delta E_S) / q_0 |\delta E_S|, \\
m_0 &= [n_0^2 + 8 (\delta E_S)^2]^{1/2}, \\
n_0 &= \Delta_0 + \delta E_S, \\
q_0 &= [2m_0 (m_0 - n_0)]^{1/2}.
\end{aligned} \tag{21}$$

Normally, the strain dependence of the spin-orbit splitting is not very significant. For simplicity, we shall ignore this dependence (i.e., $\mathbf{a}_2 \approx 0$, $\mathbf{b}_2 \approx 0$) [24]. Under this approximation,

$$\begin{aligned}
\mathbf{a}' &\approx \mathbf{a}_1 \approx \mathbf{a}_v, \\
\mathbf{b}' &\approx \mathbf{b}_1 \approx \mathbf{b}, \\
\delta E_{H,v} &\approx \delta E'_{H,v} \approx \mathbf{a}_v (2 - \lambda) \varepsilon, \\
\delta E_S &\approx \delta E'_S \approx -\mathbf{b} [1 + \lambda] \varepsilon.
\end{aligned} \tag{22}$$

In this case, where we neglect the strain dependence of the spin-orbit splitting, we can write for the strain dependence of the conduction to v_1 (hh), v_2 (lh), and v_3 (so) bands [23]:

$$\begin{aligned}
E_0(hh) &= E_0 + \delta E_H + \delta E_S, \\
E_0(lh) &= E_0 + \delta E_H + \frac{1}{2} (\Delta_0 - \delta E_S) - \frac{1}{2} \left[\Delta_0^2 + 2\Delta_0 \delta E_S + 9(\delta E_S)^2 \right]^{\frac{1}{2}}, \\
E_0(so) &= E_0 + \delta E_H + \frac{1}{2} (\Delta_0 - \delta E_S) + \frac{1}{2} \left[\Delta_0^2 + 2\Delta_0 \delta E_S + 9(\delta E_S)^2 \right]^{\frac{1}{2}},
\end{aligned} \tag{23}$$

where E_0 is the zero-strain band gap. In the Eq. (23), the bandgap shifts of the hydrostatic component δE_H and of shear component δE_S are:

$$\begin{aligned}
\delta E_H &= \delta E_{H,c} + \delta E_{H,v} = (\mathbf{a}_c + \mathbf{a}_v) (2 - \lambda) \varepsilon = \mathbf{a} (2 - \lambda) \varepsilon, \\
\delta E_S &= -\mathbf{b} [1 + \lambda] \varepsilon,
\end{aligned} \tag{24}$$

where $\delta E_{H,c}$ and $\delta E_{H,v}$ are the hydrostatic shifts of the conduction and valence band edges, respectively. Sometimes, we neglect the coupling between light-hole and spin-orbit split-off bands, and then the light-hole band gap energy $E_0(lh)$ in Eq. (23) becomes

$$E_0(lh) = E_0 + \delta E_H - \delta E_S. \tag{25}$$

Fig. 8 shows the schematic illustration of the strain effects on the band edges at $\vec{k} = 0$.

Critical Point at $\vec{k} \neq 0$ (X -point) For a biaxial strain in the (001) plane, the strain induced shifts for the X conduction band minima are given by [23]

$$\Delta E^S(X_z) = \left[-2\mathbf{a}_X (2 - \lambda) - \frac{2}{3} \Xi_u^X (1 + \lambda) \right] \varepsilon, \tag{26}$$

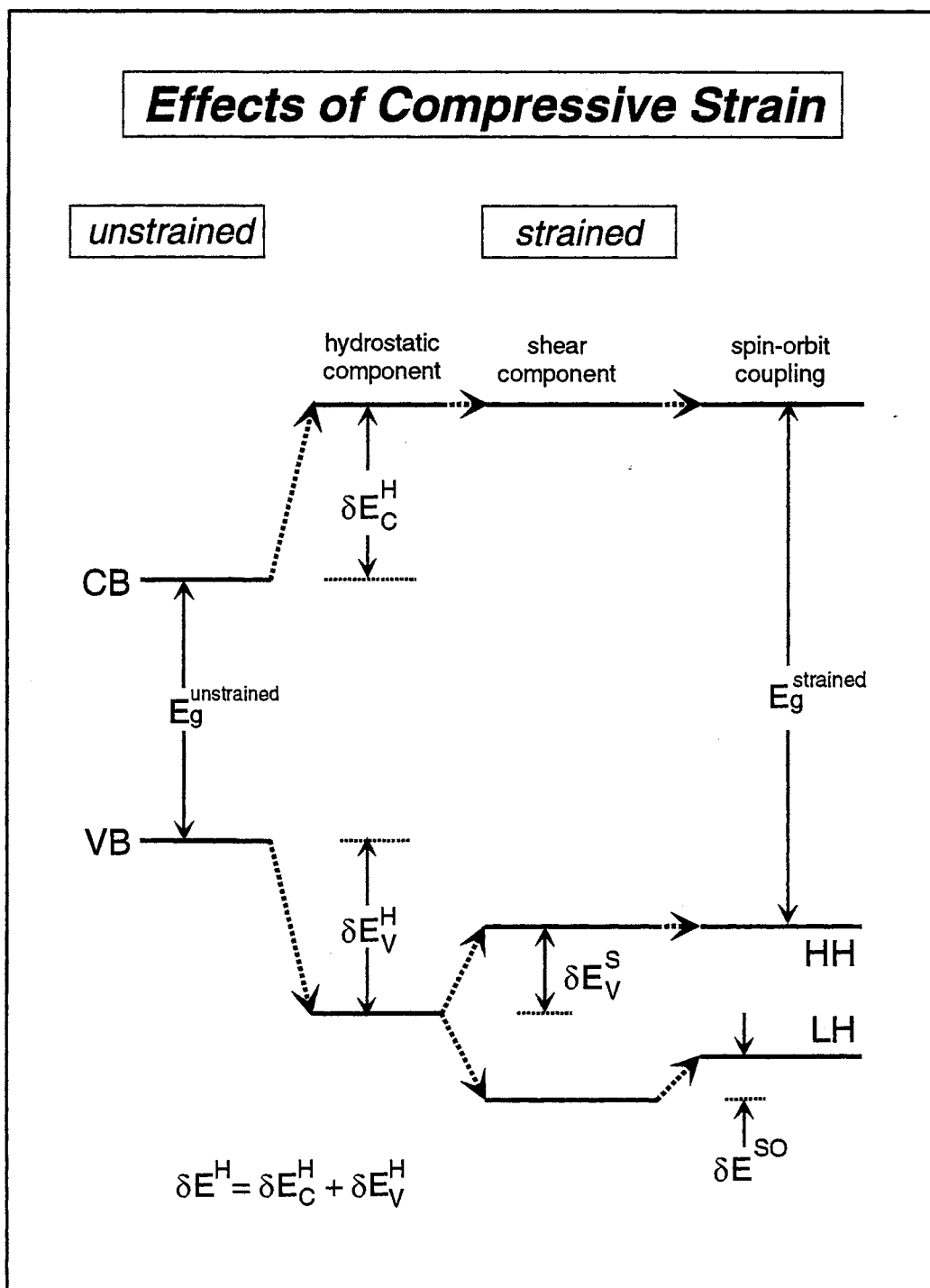


Figure 8. Schematic representation of the effects of compressive strain on the band edges.

for the [001] singlet band, and

$$\Delta E^D(X_z) = \left[-2\mathbf{a}_X(2 - \lambda) + \frac{1}{3}\Xi_u^X(1 + \lambda) \right] \varepsilon \quad (27)$$

for the [001,010] doublet bands. Here, \mathbf{a}_X is the X band gap hydrostatic deformation potential and Ξ_u^X is the shear deformation potential. For a compressive (tensile) biaxial strain in the (001) plane, the doublet bands move to higher (lower) energy than the singlet band. A more detailed discussion of the strain effects on the band structure for other directions and other band extrema can be found in Ref. [23]. Since all our samples studied are subject to biaxial strain in the (001) plane, only this type of strain will be considered in this thesis.

Calculation of interband transitions: envelope function approximation

In order to calculate the interband transition energies within QW's, we employed the envelope function approximation (EFA) which was first developed by Bastard [4–6]. In this theory, heterostructure wave functions are factorized into bulk-like Bloch functions and slowly varying envelope functions. The essential point of this EFA is to neglect any phenomena which is rapidly varying at the atomic scale, and to focus attention on the effective Hamiltonian which governs the slowly varying envelope functions. The EFA expands the Kane model [25,27–29] of the bulk semiconductor band structure to QW conduction and valence levels. Since it is a relatively simple calculation compared with other microscopic approaches such as the empirical tight binding calculations [30] and pseudopotential calculations [31], this EFA method has been applied to many heterostructures with great success and has become the most widely used theory on the electronic structure of semiconductor QW heterostructures. Since the detailed description of this EFA can be found in many papers and text books [4–6], this section presents only a brief summary of results of EFA which have been used for the calculation of the interband transitions in our QW structures.

Let us consider a heterostructure consisting of layers of bulk semiconductors A and B with the same crystal structure (zinc blende) with perfect lattice matching

between both materials. We also choose \hat{z} as the growth direction of heterostructures. As in the case of bulk semiconductors, we want to solve Schrödinger equation for the heterostructures:

$$H(\vec{r})\Psi(\vec{r}) = E\Psi(\vec{r}). \quad (28)$$

The band structure of each material A and B can be described with a dispersion relation by the Kane model. In this envelope function model, two key assumptions are made:

- (i) Inside each layer the wave function is expanded on the periodic parts of the Bloch functions of the edges under consideration

$$\Psi(\vec{r}) = \sum_n f_n^{A(B)}(\vec{r}) u_{n0}^{A(B)}(\vec{r}), \quad (29)$$

where $u_{n0}^{A(B)}$ are the Bloch functions for A and B at $\vec{k}=0$. The summation over n runs over as many band edges as are included in the analysis.

- (ii) The periodic parts of the Bloch functions are assumed to be the same in each kind of layer which constitutes the heterostructure:

$$u_{n0}^{(A)}(\vec{r}) = u_{n0}^{(B)}(\vec{r}) = u_{n0}(\vec{r}) \quad (30)$$

Since the lattice constants of the layers are assumed to be the same, the heterostructure becomes translationally invariant in the layer plane. Thus, the envelope functions f_n 's can be factorized into the form:

$$f_n^{(A,B)}(\vec{r}_\perp, z) = \frac{1}{\sqrt{S}} \exp(i\vec{k}_\perp \cdot \vec{r}_\perp) \chi_n^{(A,B)}(z) \quad (31)$$

where S is the sample area and the bi-dimensional wave vector $\vec{k}_\perp = (k_x, k_y)$ is the same in both A and B layers in order to comply with the in-plane translational invariance. We will assume that $\chi_n^{(A,B)}(z)$ varies slowly at the scale of the unit cell of each material for all n . Thus, the wave function of the heterostructure $\Psi(\vec{r})$ is a sum of the products of rapidly varying functions, u'_{n0} s, and slowly varying functions f'_n s as Eq. (29).

We can write the heterostructure Hamiltonian as:

$$H(\vec{r}) = \frac{p^2}{2m_0} + \left[V_A(\vec{r}) + \frac{\hbar}{4m_0^2c^2} (\vec{\sigma} \times \nabla V_A(\vec{r})) \cdot \vec{p} \right] Y_A \\ + \left[V_B(\vec{r}) + \frac{\hbar}{4m_0^2c^2} (\vec{\sigma} \times \nabla V_B(\vec{r})) \cdot \vec{p} \right] Y_B, \quad (32)$$

where Y_A (Y_B) are step functions which are unity when \vec{r} corresponds to an A layer (to a B layer) and 0 elsewhere. Here we neglect the band bending in the interface region. Let $\varepsilon_{n0}^{(A)}$ and $\varepsilon_{n0}^{(B)}$ denote the energies of the n -th band edge at the Brillouin zone center ($\vec{k} = 0$) of layers A and B , respectively. We then have, at $\vec{k} = 0$,

$$H(\vec{r}) u_{n0}(\vec{r}) = (\varepsilon_{n0}^{(A)} Y_A + \varepsilon_{n0}^{(B)} Y_B) u_{n0}(\vec{r}). \quad (33)$$

Then, using Eqs. (29)-(33), the Eq. (28) can be written as:

$$\sum_n \left\{ \left[\varepsilon_{n0}^A Y_A + \varepsilon_{n0}^B Y_B \right] f_n^{A(B)}(\vec{r}) u_{n0}(\vec{r}) \right. \\ \left. + \frac{1}{2m_0} u_{n0}(\vec{r}) p^2 f_n^{A(B)}(\vec{r}) + \frac{1}{m_0} [\vec{p} u_{n0}(\vec{r})] \cdot [\vec{p} f_n^{A(B)}(\vec{r})] \right. \\ \left. + u_{n0}(\vec{r}) \frac{\hbar}{4m_0^2c^2} \vec{\sigma} \times \nabla (V_A(\vec{r}) Y_A + V_B(\vec{r}) Y_B) \cdot \vec{p} f_n^{A(B)}(\vec{r}) \right\} = \sum_n E f_n^{A(B)}(\vec{r}) u_{n0}(\vec{r}) \quad (34)$$

The last term in the left is for the spin-orbit interaction and is very small. By neglecting this spin-orbit term, multiplying Eq. (34) by $u_{n0}^*(\vec{r})$ and integrating over the crystalline volume Ω , we obtain:

$$\int_{\Omega} \sum_n \left\{ \left[\varepsilon_{n0}^A Y_A + \varepsilon_{n0}^B Y_B + \frac{p^2}{2m_0} - E \right] \delta_{mn} + \frac{1}{m_0} \vec{p}_{mn}^0 \cdot \vec{p} \right\} f_n^{A(B)}(\vec{r}) d\vec{r} = 0 \quad (35)$$

where

$$\vec{p}_{mn}^0 = \frac{1}{\Omega_0} \int_{\Omega_0} u_{m0}(\vec{r}) \vec{p} u_{n0}(\vec{r}) d\vec{r}. \quad (36)$$

Here the slowly varying property of $f_n^{A(B)}(\vec{r})$ is used. The condition for non-trivial solutions of Eq. (35) is that $f_n^{A(B)}(\vec{r})$ are eigenfunction of the following equations:

$$\sum_n \left\{ \left[\varepsilon_{n0}^A Y_A + \varepsilon_{n0}^B Y_B + \frac{p^2}{2m_0} - E \right] \delta_{mn} + \frac{1}{m_0} \vec{p}_{mn}^0 \cdot \vec{p} \right\} f_n^{A(B)}(\vec{r}) = 0. \quad (37)$$

Since the heterostructure is translationally invariant in the xy -plane, by assuming that the lattice parameters of the A and B materials are the same, we can rewrite the Eq. (37), using Eq. (31), as:

$$\begin{aligned} \sum_n \left\{ \left[\varepsilon_{n0}^A + V_n(z) + \frac{\hbar^2 k_{\perp}^2}{2m_0} + \frac{1}{2m_0} p_z^2 \right] \delta_{mn} \right. \\ \left. + \frac{\hbar}{m_0} \vec{p}_{\perp mn}^0 \cdot \vec{k}_{\perp} + \frac{1}{m_0} p_z^0 p_z \right\} f_n^{A(B)}(\vec{r}) = f_m^{A(B)}(\vec{r}) \end{aligned} \quad (38)$$

where

$$V_n = \begin{cases} 0 & \text{if } z \text{ is in } A \\ \varepsilon_{n0}^B - \varepsilon_{n0}^A & \text{if } z \text{ is in } B \end{cases} . \quad (39)$$

In the case $\vec{k}_{\perp} = 0$, and by choosing $\vec{J} \parallel \hat{z}$ and using the 8 basis states of the Kane Model, given in Eqs. (16) and (17), Eq. (38) can be expressed in the block diagonal form:

$$\begin{bmatrix} H^+ & 0 \\ 0 & H^- \end{bmatrix} \begin{bmatrix} \chi^+(z) \\ \chi^-(z) \end{bmatrix} = E \begin{bmatrix} \chi^+(z) \\ \chi^-(z) \end{bmatrix}, \quad (40)$$

where $\chi^+(z)$ and $\chi^-(z)$ are 4×1 column vectors consisting of $m_J > 0$ and $m_J < 0$, respectively. H^+ and H^- are identical 4×4 matrices:

$$H^+ = \begin{bmatrix} V_s(z) + \frac{p_z^2}{2m_0} & -\sqrt{\frac{2}{3}} P p_z & 0 & \sqrt{\frac{1}{3}} P p_z \\ -\sqrt{\frac{2}{3}} P p_z & -E_g^A + V_s(z) + \frac{p_z^2}{2m_0} & 0 & 0 \\ 0 & 0 & -E_g^A + V_s(z) + \frac{p_z^2}{2m_0} & 0 \\ \sqrt{\frac{1}{3}} P p_z & 0 & 0 & -E_g^A - \Delta^A + V_{\delta}(z) + \frac{p_z^2}{2m_0} \end{bmatrix}, \quad (41)$$

where $V_s(z)$, $V_p(z)$, $V_{\delta}(z)$ are step functions describing the band offsets between A and B of the Γ_6 , Γ_8 , Γ_7 edges, respectively. It is easily seen that the heavy-hole

states are decoupled from other states and the envelope function equation for the heavy-holes is:

$$H\chi_{hh}(z) = \left[-\frac{p_z^2}{2m_0} - E_g^A + V_p(z) \right] \chi_{hh}(z) = E\chi_{hh}(z) \quad (42)$$

For the heavy-hole levels, we will solve the eigenvalue equation with envelope functions which is of the form

$$H\chi_{hh}^{A(B)}(z) = \left[p_z \frac{1}{2m_{hh}^{A(B)}} p_z - E_g^A + V_p(z) \right] \chi_{hh}^{A(B)}(z) = E\chi_{hh}^{A(B)}(z) \quad (43)$$

where m_{hh} is the heavy-hole effective mass.

For the light particles states, we have 3×3 coupled second order differential equations. If we neglect the free electron energy term, these reduce to first order differential equations. This approximation is valid because the effective masses of the light particles are much smaller than the free electron mass and therefore the contribution of the free electron energy to the kinetic energy of these particles is negligible. Neglecting the free electron energy term, we obtain the following set of three coupled differential equations:

$$V_s(z)\chi_e^{A(B)}(z) - \sqrt{\frac{2}{3}}Pp_{zx}^{A(B)}(z) + \frac{1}{\sqrt{3}}Pp_{z\chi_{so}}^{A(B)}(z) = E\chi_e^{A(B)}(z) \quad (44)$$

$$-\sqrt{\frac{2}{3}}Pp_z\chi_e^{A(B)}(z) + [E_g^A - V_p(z)]\chi_{lh}^{A(B)}(z) = E\chi_{lh}^{A(B)}(z) \quad (45)$$

$$\frac{1}{\sqrt{3}}Pp_z\chi_e^{A(B)}(z) + [-E_g^A - \Delta^A + V_\delta(z)]\chi_{so}^{A(B)}(z) = E\chi_{so}^{A(B)}(z) \quad (46)$$

By substituting Eqs. (45) and (46) into Eq. (44), we obtain a second order differential equation for $\chi_e^{A(B)}(z)$:

$$\left[p_z \frac{1}{2\mu(E, z)} p_z + V_s(z) \right] \chi_e^{A(B)}(z) = E\chi_e^{A(B)}(z), \quad (47)$$

where:

$$\frac{1}{\mu(E, z)} = \frac{2P^2}{3} \left[\frac{2}{E + E_g^A - V_p(z)} + \frac{1}{E + E_g^A + \Delta^A - V_\delta(z)} \right] \quad (48)$$

is the energy dependent effective mass. Similarly, we can obtain equations for $\chi_{lh}^{A(B)}(z)$ and $\chi_{so}^{A(B)}(z)$. Eq. (47) can be solved in layers A and B, using boundary conditions of continuity of the wave function and the particle current at the interface of A and B at $z = z_0$, that is:

$$\chi_{\nu}^A(z_0) = \chi_{\nu}^B(z_0) \text{ , where } \nu = e, lh, so, \quad (49)$$

and

$$\frac{1}{\mu^A(E)} \left. \frac{d}{dz} \chi_{\nu}^A(z) \right|_{z=z_0} = \frac{1}{\mu^B(E)} \left. \frac{d}{dz} \chi_{\nu}^B(z) \right|_{z=z_0} \quad (50)$$

Therefore, we can get the general solutions of Eq. (47) as linear combinations of incoming and outgoing plane waves:

$$\chi^A(z) = ae^{ik_A z} + be^{-ik_A z}, \quad (51)$$

$$\chi^B(z) = ce^{ik_B z} + de^{-ik_B z}, \quad (52)$$

where the wave vectors k_A and k_B can be obtained from the bulk Kane dispersion relations:

$$E(E + E_g^A)(E + E_g^A + \Delta^A) = \hbar^2 k_A^2 P^2 \left(E + E_g^A + \frac{2\Delta^A}{3} \right), \quad (53)$$

$$(E - V_s)(E - V_s + E_g^B)(E - V_s + E_g^B + \Delta^B) = \hbar^2 k_B^2 P^2 \left(E - V_s + E_g^B + \frac{2\Delta^B}{3} \right). \quad (54)$$

A more simplified approach can be found in the Ben Daniel-Duke model, which assumes that the heterostructure envelope function is built from host quantum states which belong to a single parabolic band. In this model the envelope function equation is obtained by replacing $\mu(E, z)$ in Eq. (47) with the band edge effective mass of the corresponding layer, i.e.,

$$\mu(E, z) = \begin{cases} m_A, & \text{if } z \text{ corresponding to A} \\ m_B, & \text{if } z \text{ corresponding to B.} \end{cases} \quad (55)$$

With both boundary conditions and the fact that the envelope functions $\chi^{A(B)}(z)$ satisfy the Bloch theorem, we can get a Kronig-Penney like dispersion relation for the Type-I QW structure as :

$$\cos(qd) = \cos(k_A L_A) \cos(k_B L_B) - \frac{1}{2} (\xi + \xi^{-1}) \sin(k_A L_A) \sin(k_B L_B) \quad (56)$$

with:

$$\xi = \frac{k_A}{m_A(E)} \times \frac{m_B(E)}{k_B}. \quad (57)$$

$$\frac{1}{m_A(E)} = \frac{2P^2}{3} \left(\frac{2}{E + E_A} + \frac{1}{E + E_A + \Delta^A} \right) \quad (58)$$

$$\frac{1}{m_B(E)} = \frac{2P^2}{3} \left(\frac{2}{E + E_A} + \frac{1}{E + E_A + \Delta^A - V_\delta} \right) \quad (59)$$

Now we consider a type I QW structure where $V_s > 0$, $V_p < 0$, and $V_\delta < 0$. Thus, for energies E such that $0 \leq E \leq V_s$, $V_p - E \leq E \leq -E_g^A$, or that $V_\delta - E - \Delta^A \leq E \leq -E_g^A - \Delta^A$, the wave vector k_B is imaginary. Therefore, by setting $k_B = i\kappa_B$ and $\xi = -i\tilde{\xi}$ in the above equations, we obtain their dispersion relations:

$$\cos(qd) = \cos(k_A L_A) \cosh(\kappa_B L_B) - \frac{1}{2} (\tilde{\xi} - \tilde{\xi}^{-1}) \sin(k_A L_A) \sinh(\kappa_B L_B) \quad (60)$$

When the barrier thickness L_B becomes infinitely thick resulting in an isolated QW structure, the dispersion relation becomes:

$$\cos(qd) = \cos(k_A L_A) - \frac{1}{2} (\tilde{\xi} - \tilde{\xi}^{-1}) \sin(k_A L_A) \quad (61)$$

If we use the parity of the potentials $V_s(z)$, $V_p(z)$ and $V_\delta(z)$ with respect to the center of the A layer in the above equation, this can be factorized into two equations corresponding to even and odd parity respectively:

$$\cos\left(\frac{1}{2}k_A L_A\right) - \tilde{\xi} \sin\left(\frac{1}{2}k_A L_A\right) = 0 \quad (62)$$

$$\cos\left(\frac{1}{2}k_A L_A\right) + \tilde{\xi}^{-1} \sin\left(\frac{1}{2}k_A L_A\right) = 0 \quad (63)$$

Therefore, the isolated QW bound states can be recovered.

For the heavy-hole states, we will use the same form as the Eq. (60), except that:

$$\xi = \frac{k_A}{M_{hh}^{(A)}} \frac{M_{hh}^{(B)}}{k_B} \quad (64)$$

with

$$k_A = \left(\frac{2M_{hh}^{(A)}}{\hbar^2} (-E_g^A - E) \right)^{\frac{1}{2}} \quad (65)$$

$$k_B = \left(\frac{2M_{hh}^{(B)}}{\hbar^2} (-E_g^A - E + V_p) \right)^{\frac{1}{2}} \quad (66)$$

where $M_{hh}^{(A)}$ and $M_{hh}^{(B)}$ are the effective mass of heavy-holes for layers A and B, respectively. Again, for energy less than barrier height, $-E_g^A + V_p < E < -E_g^A$, the wave vector k_B becomes imaginary. In this case, the equation should be modified, replacing k_B by $i\kappa_B$ and ξ by $-i\tilde{\xi}$.

Band offset

The band offset is one of the most important parameters in the design and characterization of heterostructures. However, accurate band offset values for most heterostructures are not well known. One of major reasons for the difficulties in experimentally determining accurate band offsets is that high quality samples with extremely sharp interfaces are required. Therefore, only a few heterostructures, such as GaAs/AlGaAs, have been extensively studied. Various experimental and theoretical efforts have been made in determining band offsets in heterostructures [8].

The most typical experimental techniques for determining the band offset are spectroscopic techniques, such as absorption [32,33], photoluminescence excitation (PLE) [34–36], and photoconductivity (PC) [37]. In these methods, the interband transition energies are measured and then compared with values from theoretical calculation using the band offset as one of the fitting parameters. In these techniques, there are some problems in reliability of the resulting band offset values. One is that the theoretically calculated transition energies are not sensitive to the band offset values. Another significant problem would be that the theoretical model itself may not be perfect, giving an error in the result which we can not verify. Even with these problems, the band offsets values for the GaAs/AlGaAs system from theories and experiments are in a good agreement. However, for many other material systems, they often do not agree.

Hydrostatic pressure, in general, produces a uniform dilation of the center of gravity of a given band edge, and hence a uniform motion (without splitting)

of the various semiconductor band gaps (i.e., Γ , X , L , etc.). The motion of a gap of given symmetry is defined in terms of the band gap hydrostatic deformation potential, and volume dilation $\Delta V/V_0$, of the crystal. Therefore, application of hydrostatic pressures on semiconductors, not only bulk but also QW structures, will bring great insight to the physics of any material of interest.

Using the pressure characteristics of different conduction band edges, this pressure-optical technique of determining the band offset of QW's and SLs has been developed independently by Venkateswaran *et al.* [38] and Wolford *et al.* [39]. These pioneering works on the determination of the band offset of a GaAs/AlGaAs QW system at high pressure provided a spectroscopic method to determine the band offsets of semiconductor QW and SL structures. This pressure-optical technique has proved to be a powerful method for determining the band offset in QW structures because it is a more direct method than other experimental methods. There have been numerous optical investigations utilizing the effect of different pressure coefficients for different conduction band minima to induce the Type-I to Type-II conversion and to determine the band offsets in some SLs and QW systems [13,40–48].

Energy level crossing and valence band offset

Bulk Semiconductors It is well known that band edges of a semiconductor have different pressure coefficients. For direct band gap semiconductors such as GaAs, the pressure coefficients of Γ -, L - and X -band edges are about 10.7, 5.6 and -1.3 meV/kbar, respectively. The application of hydrostatic pressure to a direct band gap semiconductor can therefore lead to an indirect band gap semiconductor [49–52]. As the pressure is increased, Γ - and L -band edges move up in energy while the X -band edge moves down due to its negative pressure coefficient (Fig. 9). When the pressure reaches a certain value, P_c (crossover pressure), the Γ - and X -band edges are lined up. At pressures higher than P_c , the X -band edge becomes the lowest conduction band edge, then this material becomes an indirect band gap semiconductor. The pressure dependence of the band edges in bulk GaAs

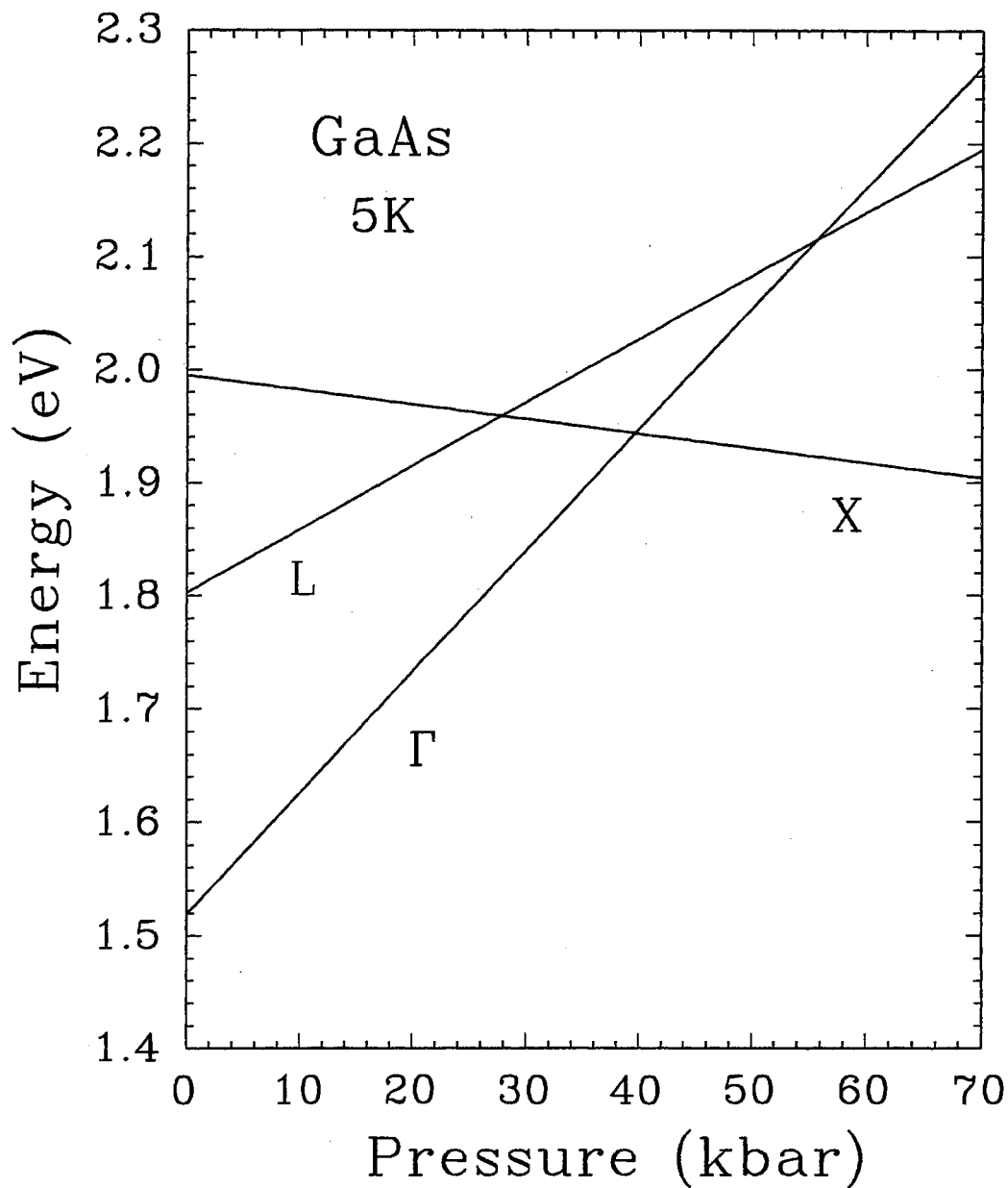


Figure 9. Pressure dependence of the band edges of bulk GaAs at low temperature.

Band edges of GaAs have different pressure coefficients. Pressure coefficients of Γ -, L -, and X -band edges are about 10.7, 5.7 and -1.3 meV/kbar, respectively. The Γ - X crossover occurs at pressure around 40 kbar. Then, a direct band gap bulk GaAs becomes an indirect gap material at pressures higher than this crossover pressure P_c , because the X -band edge becomes the lowest conduction band edge.

is shown indicating the crossings of $\Gamma - X$ and $L - X$ band edges. These $\Gamma - X$ and $L - X$ band edge crossings occur around 40 and 55 kbar, respectively. Such a phenomenon of pressure-induced band edge crossover will be utilized to study band offset in some QW systems discussed later on in this thesis.

Quantum wells In a Type-I QW, such as a GaAs/Al_xGa_{1-x}As QW, electrons and holes are confined in the well layers. Fig. 10 illustrates schematically the pressure effect on the band edges of a Type-I QW. As the pressure increases, the X -band edge in the barrier moves down in energy and the Γ -band edge in the well moves up in energy increasing the PL transition energy as mentioned for the bulk case (Fig. 10a). At pressures $P < P_c$, the measured PL transition between the lowest Γ -confined levels in conduction and valence bands is:

$$E_{PL}(P) = E_{1e-1hh}^{\Gamma-\Gamma}(P) - E_{ex}^b, \quad (67)$$

where $E_{1e-1hh}^{\Gamma-\Gamma}$ is the energy between the first confined electron level ($1e$) and the first confined heavy-hole level ($1hh$) in the well. In Eq. (67), E_{ex}^b denotes the exciton binding energy. At a certain pressure $P = P_c$, the X -band edge in the barrier lines up with the first confined electron state in the well. Some electrons in the well can be expected to transfer into the barrier.

At pressures $P > P_c$, the X -band edge of the barrier is lower in energy than the lowest Γ -confined level in the well. Then, the structure becomes a spatially separated Type-II QW, that is, the lowest confined transition occurs between the X -band edge of the barrier and the lowest confined heavy-hole level in the well (Fig. 10b). The PL transition at pressures $P > P_c$, can be expressed as:

$$E_{PL}^X(P) = E_{1hh}^{X,B}(P) - E_{ex}^b \quad (68)$$

where $E_{1hh}^{X,B}$ denotes the transition between X -band edge of the barrier and $1hh$ state in the well.

From Fig. 10a, the valence-band offset for a QW at atmospheric pressure can be deduced using the formula [13,40]

$$\Delta E_v(P = 0) = E_g^{X,B}(0) - E_{1hh}^{X,B}(0) + E_{1hh} \quad (69)$$

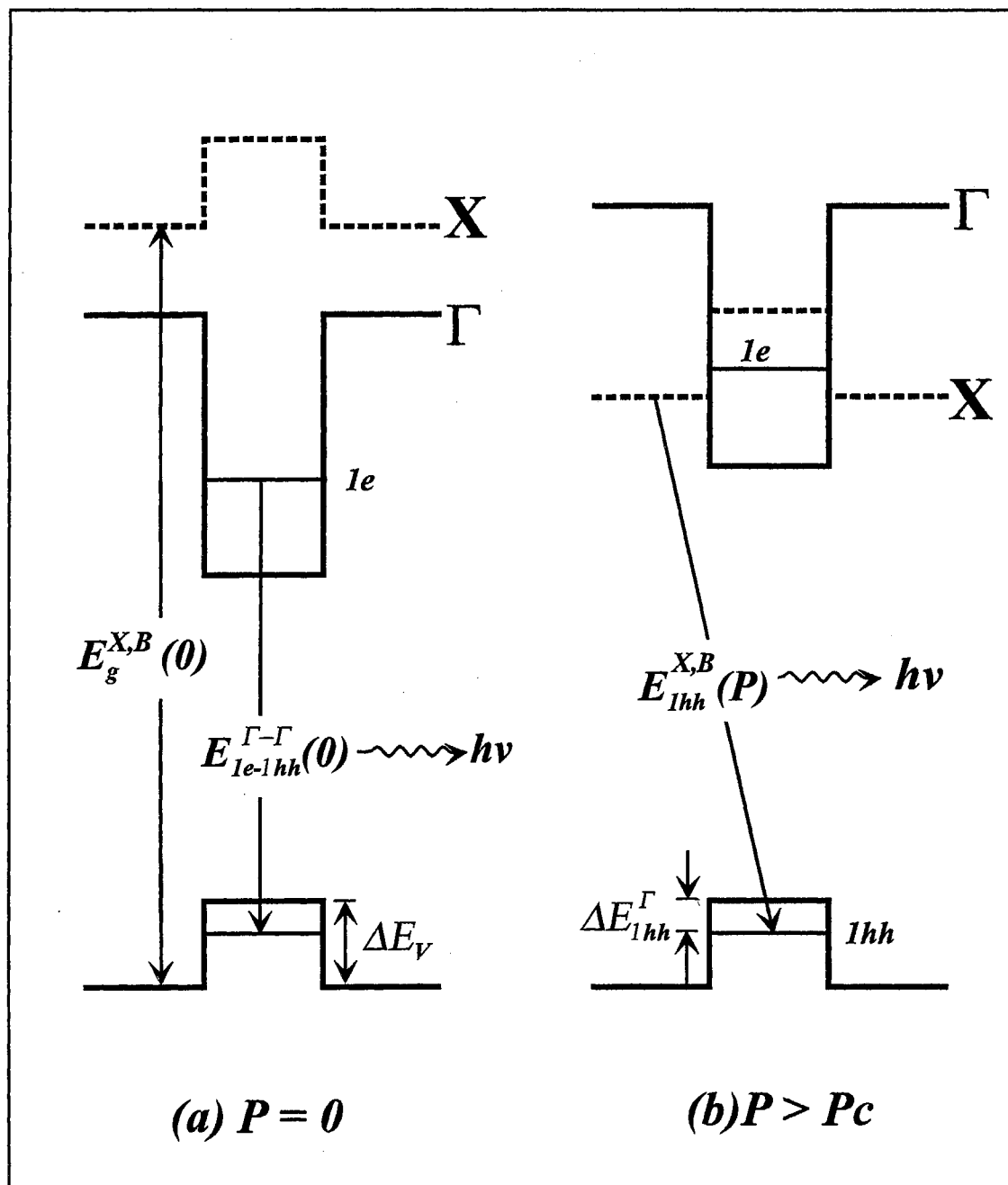


Figure 10. Band alignments for a Type-I quantum well (a) before and (b) after the crossover pressure, P_c . The direct Type-I transition with energy of $E_{1e-1hh}^{\Gamma-\Gamma}(P)$ converts to the spatially separated Type-II transition with the energy of $E_{1hh}^{X,B}(P)$ at pressures $P > P_c$.

Here $E_g^{X,B}$ is the band gap energy of the barrier X_z minima and E_{11h} is the confinement energy of the lowest heavy-hole state ($1hh$) in the well. With the Eq. (68), the expression for the valence band offset at atmospheric pressure becomes:

$$\Delta E_v(P = 0) = E_g^{X,B}(0) - E_{PL}^X(0) - E_{ex}^b + E_{1hh} \quad (70)$$

Since $E_{PL}^X(0)$ can not be measured directly from conventional PL measurement, it is estimated by extrapolating from the pressure dependent PL transitions with energies of $E_{PL}^X(P)$.

CHAPTER III

EXPERIMENTAL TECHNIQUES

Low temperature photoluminescence (PL), low temperature photoluminescence excitation (PLE), and photomodulated reflectance (PR) measurements were performed to study quantum confinement effects and/or optical properties of these semiconductor samples. Effects of hydrostatic pressure on semiconductor heterostructures have been studied using various optical spectroscopic techniques in conjunction with diamond anvil pressure cell technique. Samples studied in this thesis are GaAsP/GaAs, InAsP/InP and ZnSe/CdSe QW structures, and bulk cubic GaN epilayers.

Optical measurements

Photoluminescence and excitation spectroscopies

Photoluminescence spectroscopy PL spectroscopy is the most commonly used optical experimental technique for characterizing semiconductor materials. PL is a fundamental optical process which is a measure of the radiative recombination of the photoexcited electron-hole pair. PL and absorption are somewhat different. In an absorption process, a photon is absorbed promoting an electron from the level $|i\rangle$ to the level $|f\rangle$ and photons which have not been absorbed are detected. In PL, an emission involves the transition $|i\rangle \rightarrow |f\rangle$ with $E_i > E_f$, and a photon emitted by the recombination process with energy $E_i - E_f$ can be observed. Therefore, the level $|i\rangle$ must be initially excited. Thus, the complete PL process involves (1) excitation of electrons into the conduction band with an energy higher than the fundamental band gap, (2) relaxation down to the band minima via non-radiative processes, and then (3) recombination with holes by emitting photons.

The radiative channel is in competition with nonradiative relaxation processes such as phonon emission, capture by deep centers, Auger effect, etc.. In nonradiative processes, the excited carriers are sent to lower states from which they can emit photons by electron-hole recombination or relax further nonradiatively to lower excited states. Therefore, the lifetimes of the level $|i\rangle$ with respect to the radiative and nonradiative relaxations are the key factors to determine which relaxation process will occur in PL. For example, if the lifetime of level $|i\rangle$ for a radiative process is longer than that for a nonradiative process (this is the most common case), the carrier will relax nonradiatively down to a lower state, usually emitting phonons. Another distinctive difference between PL and absorption is that the PL signal intensity is sensitive to the population density of the excited states while the absorption is sensitive to the density of states. Therefore, the lowest lying excited states are favorable for PL, even though their density of states is very small. In fact, in bulk semiconductors at low temperature, the PL very often involves impurity levels even though the density of states for the impurity levels is much smaller (by the several orders of magnitude) than that of free states in the band. Therefore, due to their small density of the states, impurity levels are not usually observed in absorption. In a QW at low temperatures, the PL signal usually corresponds to the lowest confined exciton energy emitting a photon of energy E_{PL} :

$$E_{PL} = E_g^W + E_{1e} + E_{1hh} - E_{ex}^b, \quad (71)$$

where E_g^W is the band gap energy of the bulk well material, E_{1e} and E_{1hh} are the confinement energies of the lowest electron and heavy-hole subband, and E_{ex}^b is the exciton binding energy. The spectral half-width is considered to reflect the quality of the heterostructures, such as interface roughness or layer thickness fluctuation, etc..

Photoluminescence excitation spectroscopy In PLE spectroscopy, the detection spectrometer is set at some energy inside the emitted photoluminescence band while the energy of the excitation light source is scanned above the detection energy. As a result, the variation of the luminescence intensity from the various

excited levels is measured at the fixed detection energy. When the excitation light source is scanned, these excited states $|2\rangle, |3\rangle \dots$ will be populated at rates $g_2, g_3 \dots$ respectively. These population rates are proportional to the absorption coefficients $\alpha(E_2), \alpha(E_3) \dots$. Once these states are populated, the carriers will relax down to the lower states radiatively or nonradiatively. When some fraction of the population reaches the lowest lying excited state $|2\rangle$, radiative recombination occurs emitting photons corresponding the detection energy. The PLE spectrum then is obtained by recording the intensity of this luminescence as a function of the excitation energy. Usually the observed photon energy of the lowest interband transition (E_{11h}) measured by PL is lower than that given by PLE. This difference is called Stokes shift and is due to the inhomogeneity of the heterostructure interfaces caused by the interface roughness.

This PLE technique is particularly useful for QW structures because it can probe the higher confined levels. One important advantage of the PLE technique, particularly in the multiple quantum well structure, is that PLE is more selective than the absorption technique. If we have different size of quantum wells within a sample, the absorption technique cannot give information about each well separately because it gives all possible transitions including higher order transitions. However, separate PLE spectra for individual QW can be obtained by setting the detection spectrometer at the PL energy corresponding to that QW.

Experimental Setup The experimental setup for the PL and PLE is shown in Fig. 11. In most cases, an Ar^+ laser or a He-Ne laser are used as an excitation source for the PL measurement. Quasi-monochromatic light from a tungsten halogen lamp dispersed by a 0.25 m monochromator (SPEX 1681) was used for the excitation source for PLE measurements. Samples were mounted on a sample block and attached to the closed cycle refrigerator for measurements at low temperature down to 10 K. The excitation light source was focused on the sample in the backscattering geometry and the collected luminescence signal was dispersed by a monochromator. Then, the PL signal was detected by a photon counting system with the proper detector and processed by a computer. Depending

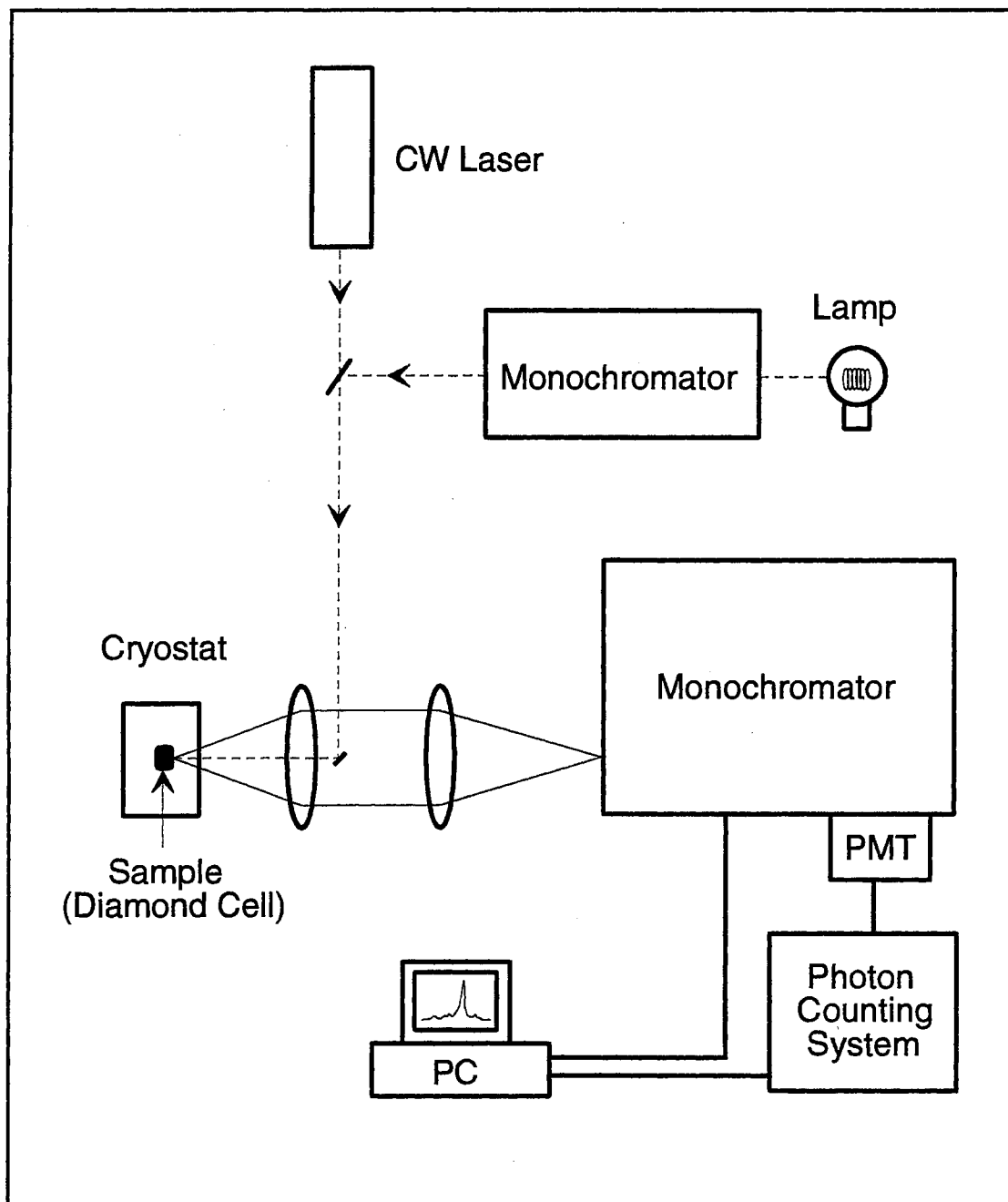


Figure 11. Experimental setup for the photoluminescence (PL) and photoluminescence excitation (PLE) measurement. Various lasers were used for the excitation source for the PL measurement. Monochromatic light from a 250 W tungsten halogen lamp dispersed by a monochromator was used as the excitation source for the PLE measurement.

on the experimental conditions, such as wavelength range and sample structure, different monochromators and detectors were used. More equipment details will be discussed in later chapters.

Modulation spectroscopy

Overview The basic idea of modulation spectroscopy is that the derivative form of the spectrum with respect to a parameter is measured while in conventional spectroscopy a direct optical spectrum is usually measured. This can easily be accomplished by applying the parameter as a small perturbation in a periodic fashion and measuring the corresponding change in the optical properties with a phase sensitive detection technique such as a lock-in amplifier. The modulation of a parameter will change some optical properties of material. For example, in electromodulation spectroscopy, the modulation of the external electric field changes the electric field inside of the material resulting in the modulation of its dielectric function.

Structures in the conventional optical spectra are considerably enhanced in the derivative-like spectra while flat and structureless backgrounds are eliminated. Fig. 12 shows a comparison of typical spectra from conventional linear measurement and the corresponding modulation results. As shown in Fig. 12a), weak structures in conventional spectrum are sometimes impossible to resolve due to the large background. As shown in b) and c), however, structures can be more easily resolved in a modulation measurement since the structureless background is depressed while the structures are enhanced due to the derivative nature of the experiment. Thus, the main advantage of modulation spectroscopy lies in its ability to resolve weak structures.

Many types of modulation spectroscopy have been used to study semiconductors with each technique having a different modulated parameter. For example, the electric field, either built-in or applied, is the modulated parameter in the electromodulation. There are some commonly used modulation techniques

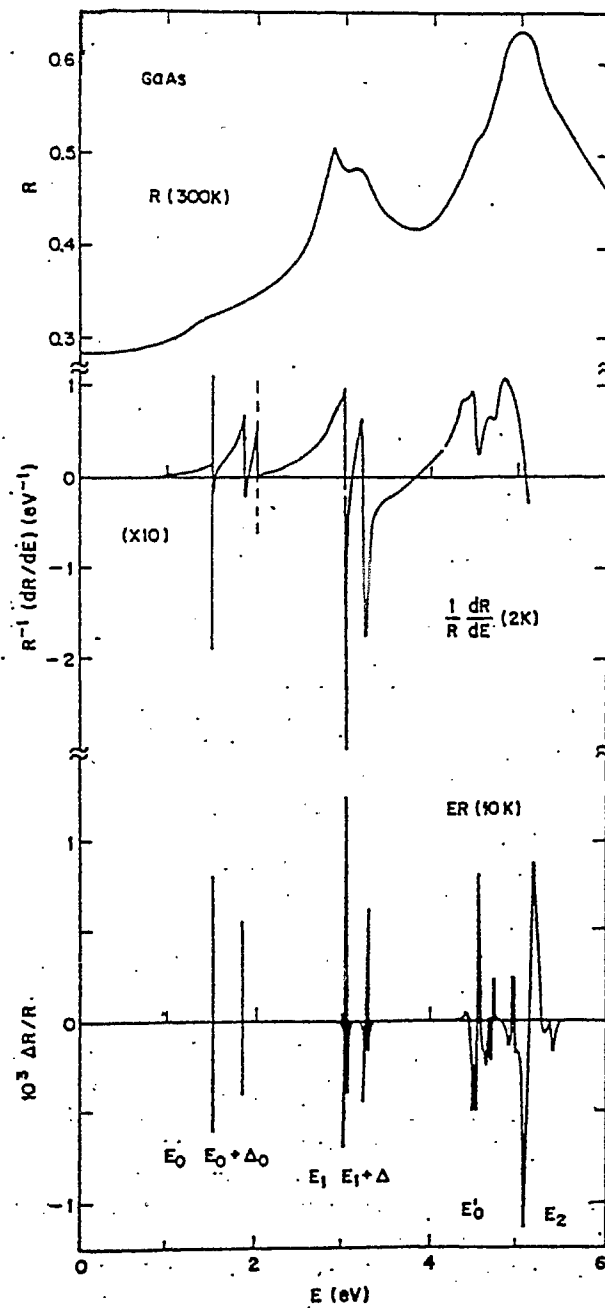


Figure 12. A comparison of three types of spectra for a GaAs semiconductor. Top: reflectance; middle: energy derivative reflectance; bottom: low-field electroreflectance (after [53]).

depending on parameters which can be changed in measurement conditions: electromodulation (electric field : either applied or built-in field), wavelength modulation (wavelength of incident beam), thermomodulation (sample temperature), piezomodulation (stress), magnetomodulation (applied magnetic field), etc. The detailed descriptions of these modulation techniques can be found in various review articles [54,53,55].

Among these modulation techniques, electroreflectance (ER) and photoreflectance (PR) are popular room temperature probes for studying optical properties of semiconductors. Because of their derivative nature, sharp optical features related to interband transitions in the material under study can be readily obtained. As a direct consequence of the derivative nature of modulation spectroscopy, information can be obtained about the response of the sample to the applied perturbation (used for the modulation), i.e. the electric field or optically induced free carriers.

ER has been used extensively for characterizing bulk material due to its high sensitivity at room temperature. However, it requires special treatment of the samples such as making electrodes in order to apply the E-field. Consequently, the sample has to be processed before experiments can be performed. Furthermore, these ER techniques are not applicable to microstructures grown on semi-insulating substrates.

A more convenient experimental method, the photoreflectance (PR) technique, which is first introduced by Wang *et al.* in 1967 [56] as a special form of the electromodulation spectroscopy, does not require any electric contacts on the sample. This contactless form of electromodulation spectroscopy has become very popular for the study of semiconductors, in particular, for two dimensional electronic system such as quantum wells and superlattices. Due to the relative ease of performing PR experiments, a great amount of work has been done on semiconductors both bulk and microstructures including QW's [55,57,58] as well as on heterostructure devices [55,59]. Even though intensity and sensitivity in PR are much less than in the ER case, the PR technique has been widely used as a room

temperature probe, particularly for routine characterizations, for semiconductor heterostructures because of the non-contact method and relative simplicity of the experiment.

One drawback of modulation spectroscopy is that the interpretation of the modulation spectrum, especially line shapes, involves the rather formidable problem of theoretically describing the optical properties in the presence of a perturbation. However, considerable progress can be made without completely solving this problem, especially if one is only interested in the energy positions and selection rules of sharp structures and not in analyzing the detailed line shapes.

Since we were only interested in the transition energies in the PR spectra taken in this work, the complicated line shape of the modulation spectrum will not be discussed in detail. Well documented and detailed line shape discussion of the modulation spectra can be found in many places [53,55]. It is worth noting that the changes in the dielectric function by the optical modulation has a third derivative functional form (TDF) for 3-dimensional systems such as bulk [53,55] and superlattice and a first derivative functional form (FDF) in 2-dimensional system such as QW's [60,55].

Mechanism Photorefectance (PR), a contactless form of electromodulation spectroscopy, takes advantage of the fact that the Fermi level is pinned at the surface in the depletion region of the semiconductor interface. A number of early studies have indicated that PR is a modulation of the electric field built-in near the surface [56,54,60,55].

The mechanism of this kind of field modulation is schematically illustrated in Fig. 13, for an n -type semiconductor. When a semiconductor is exposed to the air, the Fermi level is pinned at the semiconductor surface inducing a space-charge layer near the surface producing a built-in field. Then, this pinning introduces surface states (Fig. 13a) and occupied surface states contain electrons from the bulk. When the modulated laser light is incident on the sample surface with energy higher than band gap (Fig. 13b), the photoexcited electron-hole pairs are separated by the built-in field. Then, the minority carriers (holes in this case) are swept toward

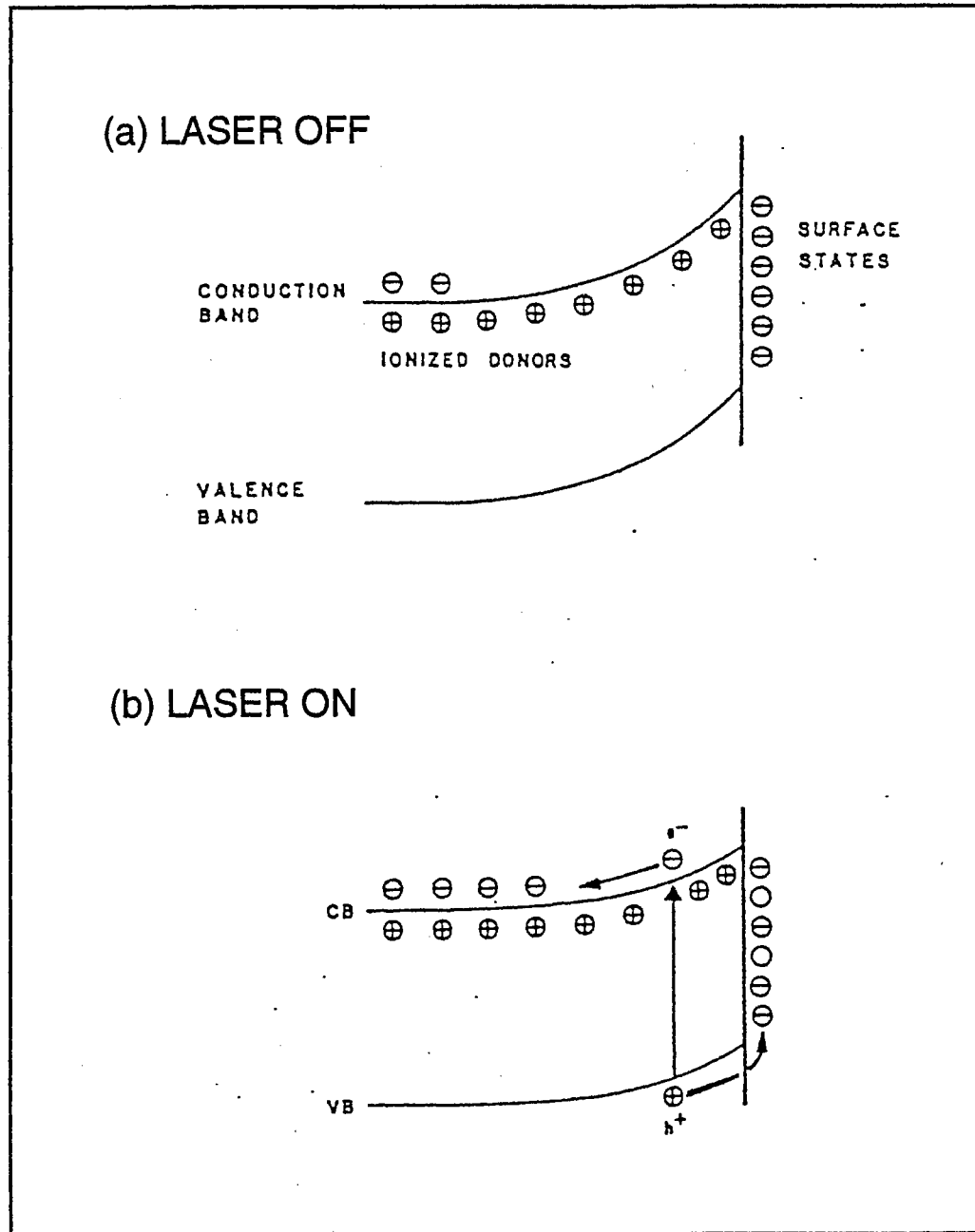


Figure 13. Photoreflectance effect with above band gap illumination creating electron-hole pairs. Minority carriers reduce charge in surface states (after [57]).

the surface. At the surface, the holes neutralize the charges trapped at surface states and thereby reduce the built-in field. Therefore, the modulation of the built-in field can be obtained by the periodic change of the photoexcited carriers, for example, by turning on and off the laser. Then, the periodically modulated built-in field by the photoexcited carriers will cause a periodic change in the dielectric function of the sample resulting in changes in the absorptivity or reflectivity. This spectroscopy has shown to be sensitive to critical point transitions in the Brillouin zone, with the resulting spectrum having sharp derivative-like features and little if any featureless background.

Although this mechanism is well understood in the bulk case, the mechanism of PR in QW (2D) structures should be somewhat different. In QW's, because carriers (electrons and holes) are confined in the growth direction, the excitonic effect becomes dominant showing excitonic transitions even in room temperature absorption. Therefore, the exciton should be considered when extending the PR mechanism from the bulk to the QW case. In the bulk case, the band to band transition is dominant while the exciton effect is very small. However, the experimental results [58,60] indicated that the PR spectra should be described by the excitonic dielectric function modulated by changes in excitonic transition energy at low temperature below 150K. For higher temperatures, since the excitonic effect decreases, the PR spectra is described better by the changes in the energy near the 2D critical point which is similar to the bulk case.

The basic concept of modulation spectroscopy is that the small periodic perturbation of an experimental parameter causes changes in physical properties of the material such as the dielectric function. The perturbation induced change ΔR or ΔT in the reflectance R or transmittance T of a sample makes change in the intensity reflected or transmitted by the sample such that

$$\begin{aligned}\Delta I/I &= \Delta R/R \text{ or} \\ \Delta I/I &= \Delta T/T .\end{aligned}\tag{72}$$

The complex dielectric function, which is a fundamental quantity describing the dielectric response of the material, can be written as;

$$\epsilon(\omega) = \epsilon_1(\omega) + i\epsilon_2(\omega) \quad (73)$$

Since this dielectric function is related to the reflectance, the differential changes in reflectivity can be expressed in terms of the perturbed complex dielectric function $\epsilon(\omega)$ in a simple manner as [61]:

$$\frac{\Delta R}{R} = \alpha\Delta\epsilon_1(\omega) + \beta\Delta\epsilon_2(\omega) \quad (74)$$

where $\Delta\epsilon_1(\omega)$ and $\Delta\epsilon_2(\omega)$ are real and imaginary components of the differential change in the complex dielectric function, $\Delta\epsilon(\omega) = \Delta\epsilon_1(\omega) + i\Delta\epsilon_2(\omega)$. The α and β are the Seraphin coefficients and are functions of the unperturbed dielectric function. In general, the α and β are nonzero quantities, but under special conditions, such as near the fundamental band gap of bulk material, $\beta \approx 0$, so that $\Delta R/R \approx \alpha\Delta\epsilon_1(\omega)$. In multilayer structures (QW's and SL's), however, interface effects become important so that the Seraphin coefficients are modified (β is no longer zero) and both $\alpha\Delta\epsilon_1$ and $\beta\Delta\epsilon_2$ have to be considered in Eq. (74).

Experimental setup Because modulation techniques take advantage of a small periodic perturbation applied to a physical property of the sample, the small change in the optical response (reflectivity or absorptivity) is detected by a phase sensitive technique, such as use of a lock-in amplifier by tuning the reference frequency to the modulating frequency. Fig. 14 shows a schematic of the PR experimental setup. Light from a halogen tungsten lamp was dispersed by a 0.25 m monochromator and then focused on the surface of the sample. In some cases, a cutoff filter was put at the exit slit of the monochromator to eliminate the effect of the second order of the light source. The reflected light from the sample was focused on a slit in front of the detector.

The modulating light, here a laser, passes through an optical chopper and is incident on the same spot of the sample surface as for the monochromatic light. The frequency of the chopper is used as the reference and is fed into the lock-in amplifier. An appropriate cut-off filter was put in the light path to block any

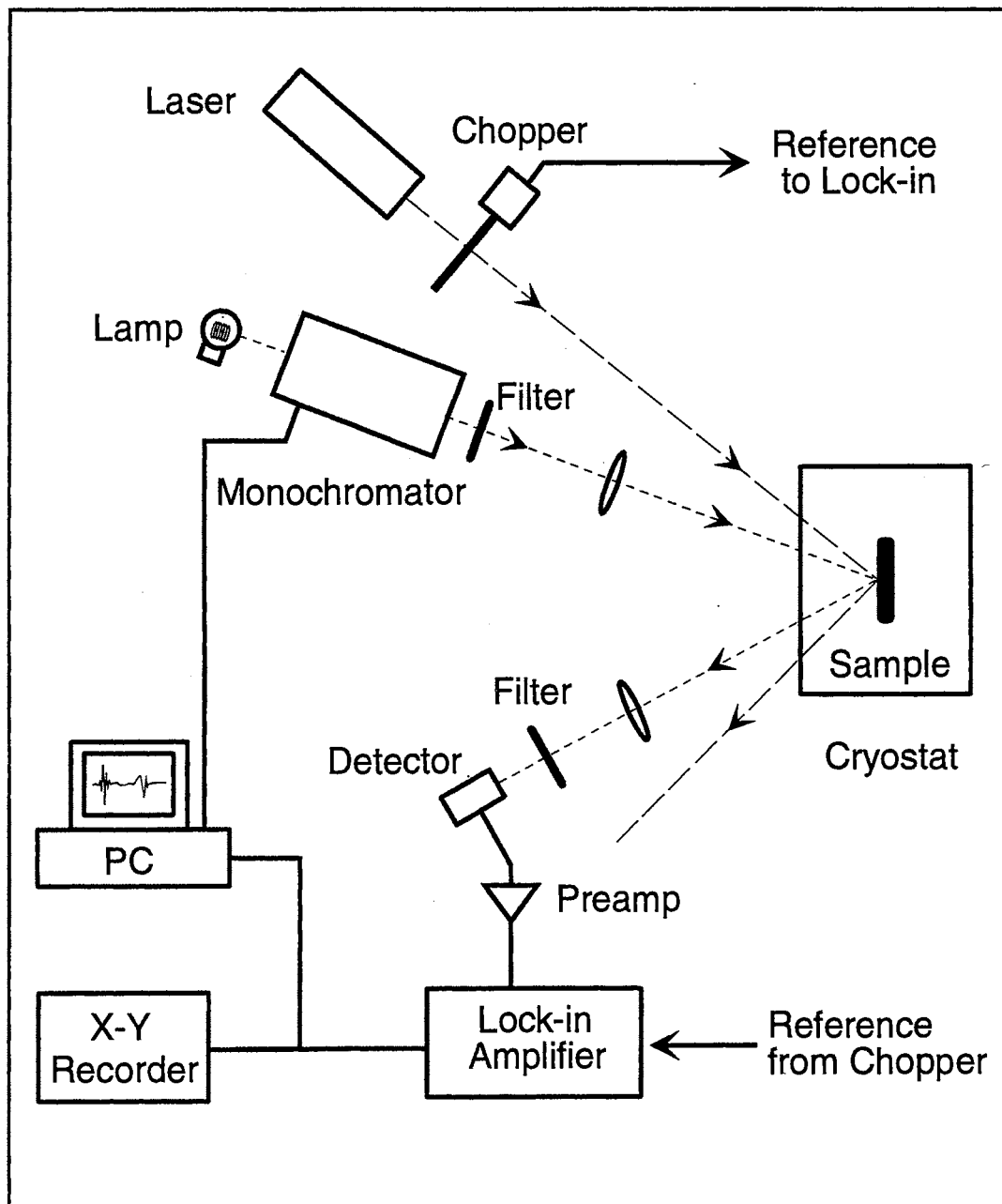


Figure 14. Experimental setup for the photoreflectance measurement. Different detectors were used for different spectral region for different samples.

scattered modulating light from the sample surface to avoid saturating the detector. The change in reflectivity associated with the creation of the surface potential of the sample was detected and amplified by the lock-in amplifier. The detectors used in this study are a Si -diode for visible and near infrared region, and a thermoelectrically cooled Ge detector (EG&G Judson, J16TE2) for the near infrared region ($0.8\sim 1.8\ \mu\text{m}$).

PR signal contains two components: a DC component or averaged value I_0R , and an AC component as a modulated signal $I_0\Delta R$. In order to get the quantity $\Delta R/R$ which is the quantity of interest, the common factor I_0 should be eliminated. This normalization can be accomplished in several ways. The simplest way is to measure R and ΔR independently and to divide the two quantities. Another way to get $\Delta R/R$ is to keep R constant electronically. In this method, a feedback servomechanism is used to keep the DC output of the detector constant by changing the gain of the detector. The most recent technique is to use a continuously variable neutral density filter placed after the monochromator to keep the DC intensity of the reflected light constant via a servomechanism [62]. In this method, the output of the lock-in amplifier will be proportional to $\Delta R/R$.

In the PR experimental setup, one of the important parts is filtering the stray laser light because it has the same chopping frequency as the signal of interest and can easily be detected. Furthermore, band gap luminescence induced by the laser illumination can be detected and can be greater in intensity than the signal of interest under certain conditions. This problem can be eliminated by using long-focal length optics or by using a second monochromator synchronized with the probe monochromator [58,63].

Photomodulated transmission (PT) is basically the same technique as the PR except PT measures a different parameter. That is, PT measures the change in the transmission while PR measures the change in reflectance. As shown in Fig. 15, the experimental setup for PT is just different in that the experimental configuration is in the transmission geometry.

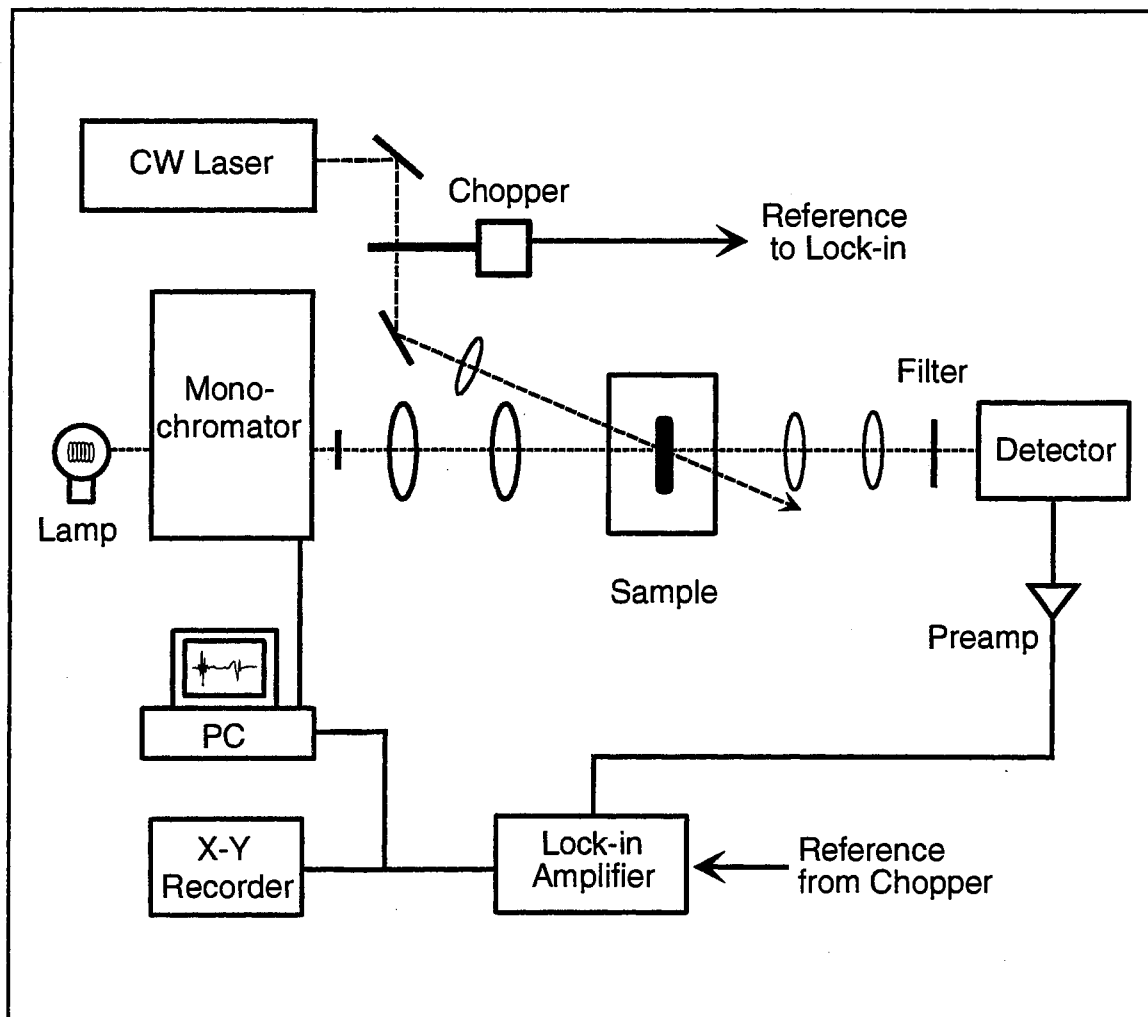


Figure 15. Experimental setup for the photomodulated transmission (PT) measurement.

Diamond anvil cell technique

Application of the hydrostatic pressure is a very powerful technique to study solid state materials because it does not change the crystal symmetry. Great improvement has been made both in expanding experimental applications and in designing pressure cells since the 1960's [64]. Among the various pressure cells used in these experiments, the diamond anvil cell (DAC) has been recognized as the most useful pressure cell for a variety of experiments, particularly optical experiments, utilizing the hardness and transparent properties of diamond. Since the first DACs [65,66], many improvements have been made both in technique and in application [64]. One of the great achievements is that this technique has been used for the study of semiconductors, especially the hydrostatic pressure effect on the band structure of the semiconductors. As discussed in the previous chapter, one particular example is that the band offset in the heterostructures can be directly determined by utilizing the different pressure coefficients of the conduction band edges.

Principle of diamond anvil cells

Fig. 16 shows the basic structure of a DAC. The major components of DAC are two diamond anvils, a stainless steel gasket with a hole at center, and metal housing to secure the pressure inside cell. The small polished flat surface ($\sim 1\text{mm}\phi$) at the tip of the diamond anvil is called the culet. The size of the hole in the stainless steel gasket is about $< 400\ \mu\text{m}$ in diameter and $< 300\ \mu\text{m}$ in depth and used as the pressure chamber where sample, ruby and the pressure medium are filled.

Even though a small sample size is required due to the size of the diamonds, the DAC technique has become very popular and a powerful tool for high-pressure optical experiments. The advantage of the DAC is that diamond is the hardest material known and is very transparent in a wide spectral range including UV,

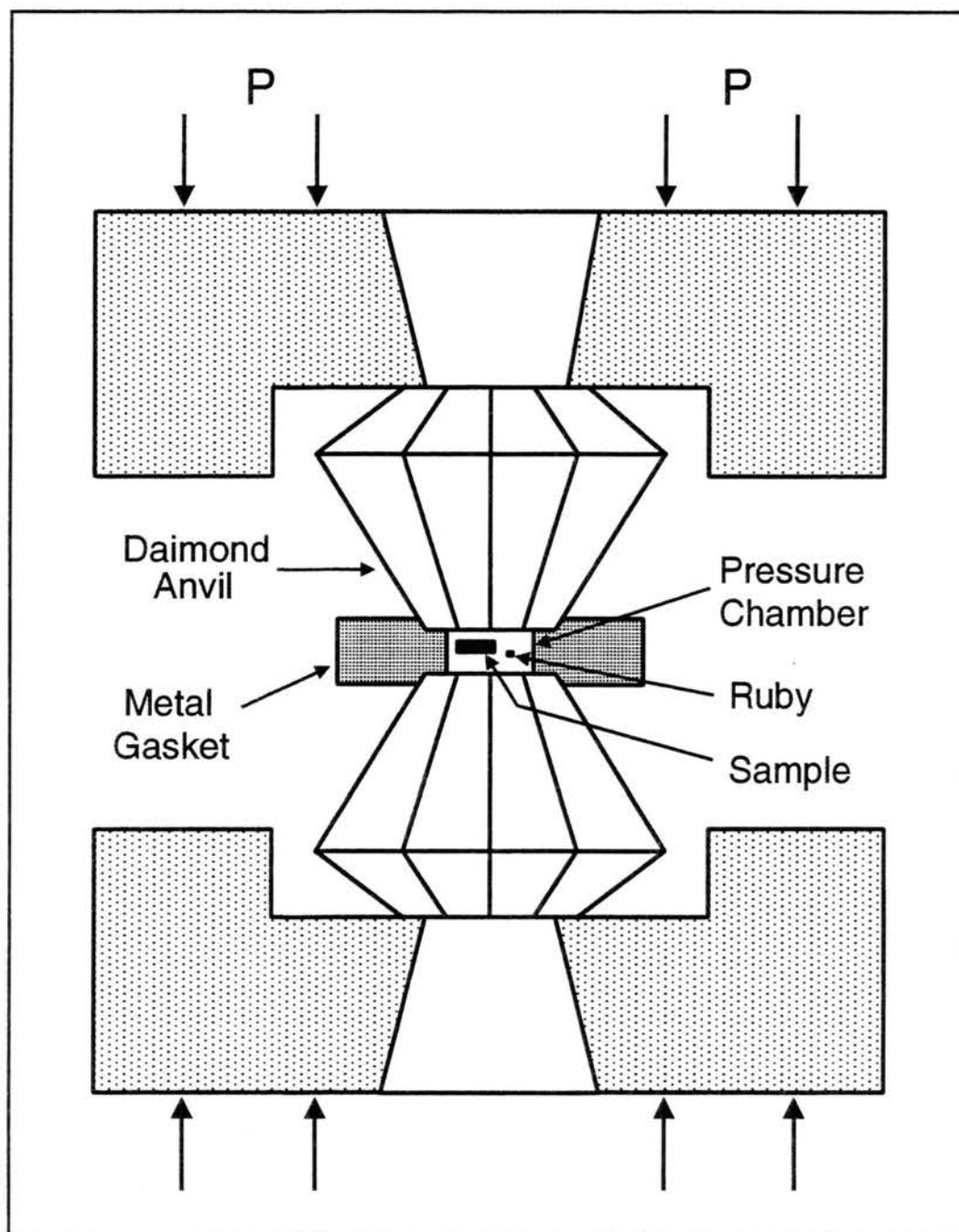


Figure 16. Schematic representation of a diamond anvil cell for the application of the hydrostatic pressure on a sample. A piece of sample is mounted inside a gasket (pressure chamber) between two diamonds along with a piece of ruby as pressure calibration. A methanol-ethanol mixture (4:1) is used for the hydrostatic pressure medium.

visible, mid infrared, and x-ray. Thus, using a DAC, optical spectroscopy can be performed over a very wide spectral range.

Pressure media

To apply hydrostatic pressure to the sample, it should be immersed in a hydrostatic pressure medium. Therefore, the most important requirement for the pressure medium is that it should have hydrostatic behavior in the range of pressure and temperature of interest. Depending on the experimental condition, a proper pressure media should be chosen. The most convenient pressure medium is a 4:1 methanol-ethanol mixture. This mixture has been shown to be a good hydrostatic pressure medium in a wide range of pressure and temperature. This methanol-ethanol mixture remains hydrostatic up to 104 kbar at 300 K [67]. Other than liquid media, liquidized gases including Ar, He, and Xe, have proved useful as hydrostatic media for pressures up to 500 kbar at room temperature. At low temperatures (cryogenic pressure), mostly Ar gas and the methanol-ethanol mixture have been used. He gas has also proved useful as a low temperature high pressure medium even when the pressure is changed at low temperature [68]. In this case, the DAC must have the capability of changing the pressure externally while it is inside the cryostat at low temperature [69,70]. In our experiments, a methanol-ethanol mixture was used as the hydrostatic pressure medium.

Sample preparation

Due to the small size of the pressure chamber of the DAC, samples must be small enough to be mounted along with a piece of ruby which is used for the pressure calibration. When the pressure is increased, the volume of the chamber decreases. Therefore, the size of the sample should be about $200 \times 200 \mu\text{m}^2$ to allow room for the hydrostatic medium to compress. The substrate was thinned by mechanical polishing to get the total sample thickness to $\leq 25 \mu\text{m}$. After clean the

sample with trichloroethylene, the sample was cleaved to proper size by tapping it with a needle in the methanol bath.

A stainless steel gasket was placed on the culet of the bottom diamond. A sample of proper size was placed into the hole (pressure chamber) along with a piece of ruby (see Fig. 16). Afterwards, a drop of the pressure medium was added to in the pressure chamber and the other diamond was placed on top. Then, the whole DAC was secured by tightening the outer screw-type DAC housing. The external pressure on the DAC was applied with a hydraulic jack and secured by tightening the outer DAC housing. For low temperature experiments, the DAC was attached to a cold finger in a closed-cycle cryostat and cooled down to desired temperatures.

Pressure calibration

The pressure inside the DAC was calibrated using the ruby R_1 fluorescence line which is the most widely used calibration method. The R_1 line of ruby is quite intense both at low and room temperatures. At atmospheric pressure and 300 K (10 K), the ruby has doublet R_1 and R_2 lines at 6928 Å (6935 Å) and 6942 Å (6950 Å), respectively. They shift linearly with pressure to longer wavelength at a rate of 0.365 Å/kbar. The pressure coefficient of the ruby lines has been found to be independent of temperature in the range from 4 K to 300 K at pressures up to 200 kbar [64].

The pressure applied inside the DAC is determined using:

$$P = \frac{\lambda - \lambda_0}{0.365} \text{ (kbar)}, \quad (75)$$

where λ and λ_0 are the wavelengths of ruby R_1 line from the PL at the pressure applied and at atmospheric pressure, respectively. For our system, the error in the pressure measurement is less than ± 0.5 kbar. The quality of the hydrostatic pressure can be monitored by the peak shape of the luminescence. Any distortion and/or broadening of the PL peak of the R_1 ruby line indicates that the pressure inside is no longer hydrostatic. This sometimes occurred in our experiments when

the ruby chip was in contact with the sample and the diamond surface causing a non-hydrostatic situation.

CHAPTER IV

GaAs/GaAs_{1-x}P_x STRAINED MULTIPLE QUANTUM WELLS

Introduction

The GaAs/GaAs_{1-x}P_x QW systems have a wide range of applications in diode lasers and MODFETs [71,72]. These systems are very different from the most widely studied QW structures, such as InGaAs/GaAs on a GaAs substrate and InGaAsP/InP on a InP substrate, where the well layers are subject to lattice mismatch induced strain. For GaAs/GaAs_{1-x}P_x heterostructures pseudomorphically grown on GaAs substrates, the GaAs_{1-x}P_x alloy barrier layers rather than the GaAs well layers are strained. Although some studies on the optical and electrical properties of GaAs/GaAs_{1-x}P_x QW's have been reported [18,19,21,22], these material systems are not well understood. In fact, the conduction and valence band offsets at the heterointerface are not available in the literature despite their crucial importance in device designs.

In this chapter, we present the results of low-temperature PL studies on three GaAs/GaAs_{1-x}P_x strained multiple quantum well (SMQW) samples ($x=0.24, 0.32,$ and 0.39) under hydrostatic pressures. We observed in these samples that the transitions between the lowest Γ -confined electron and hole states shifted towards higher energy as the pressure increased. The pressure coefficient of each transition was determined from the pressure dependence of the PL transition energy. All pressure coefficients of heavy-hole excitonic transitions were found to be significantly smaller than that of the bulk GaAs band gap, and to depend both on the alloy compositions and the QW structures. The pressure induced crossover between the

first Γ -confined electron level in the GaAs well and the (001) X -minimum conduction band in the $\text{GaAs}_{1-x}\text{P}_x$ barrier was observed in the $x=0.32$ SMQW sample. When this crossover occurred, the emission of the $\Gamma - \Gamma$ transition quenched and the emission with the characteristics of the X -minima took over. From the observation of the $\Gamma - X$ crossover, we were able to determine the valence band offset for the $\text{GaAs}/\text{GaAs}_{0.68}\text{P}_{0.32}$ QW structure. We also observed an emission arising from a deep center in the $\text{GaAs}/\text{GaAs}_{0.61}\text{P}_{0.39}$ SMQW sample.

Experimental details and results

Samples used in this work were grown on a semi-insulating (001) GaAs substrate at 580 °C by gas-source molecular beam epitaxy (GSMBE). A 1 μm -thick undoped GaAs buffer layer was grown prior to the growth of MQW structures. The SMQW structures consist of 15-periods of GaAs wells and $\text{GaAs}_{1-x}\text{P}_x$ barriers. Undoped GaAs cap layers of about 400 Å were grown to cover the SMQW samples. A schematic of the $\text{GaAs}/\text{GaAs}_{1-x}\text{P}_x$ SMQW sample structure is shown in Fig. 17. The layer thicknesses and phosphorus concentration in $\text{GaAs}/\text{GaAs}_{1-x}\text{P}_x$ were determined by computer simulations to X-ray rocking curves. Further details of the sample growth and structures can be found elsewhere [73,74].

The pressure dependent PL measurements at 10 K were performed on the samples in a backscattering geometry by using the 5145 Å line of an Ar^+ ion laser as the excitation source. The PL signal was dispersed by a 0.85 m double-grating spectrometer (SPEX 1403) and detected by a GaAs PMT (Hamamatsu) in conjunction with a photon counting system. PLE measurements were also performed at 10K.

Fig. 18 and Fig. 19 show PL spectra at different pressures taken from the GaAs (76.5 Å)/ $\text{GaAs}_{0.68}\text{P}_{0.32}$ (76 Å) and GaAs (87 Å)/ $\text{GaAs}_{0.61}\text{P}_{0.39}$ (88 Å) SMQW samples, respectively. Since the GaAs well layers are not strained in these SMQW samples, the heavy-hole band is the lowest valence band in the wells. Therefore, the lowest confined transition in these QW's is between the $n=1$ electron and the $n=1$ heavy-hole states. This transition and its energy will be denoted by

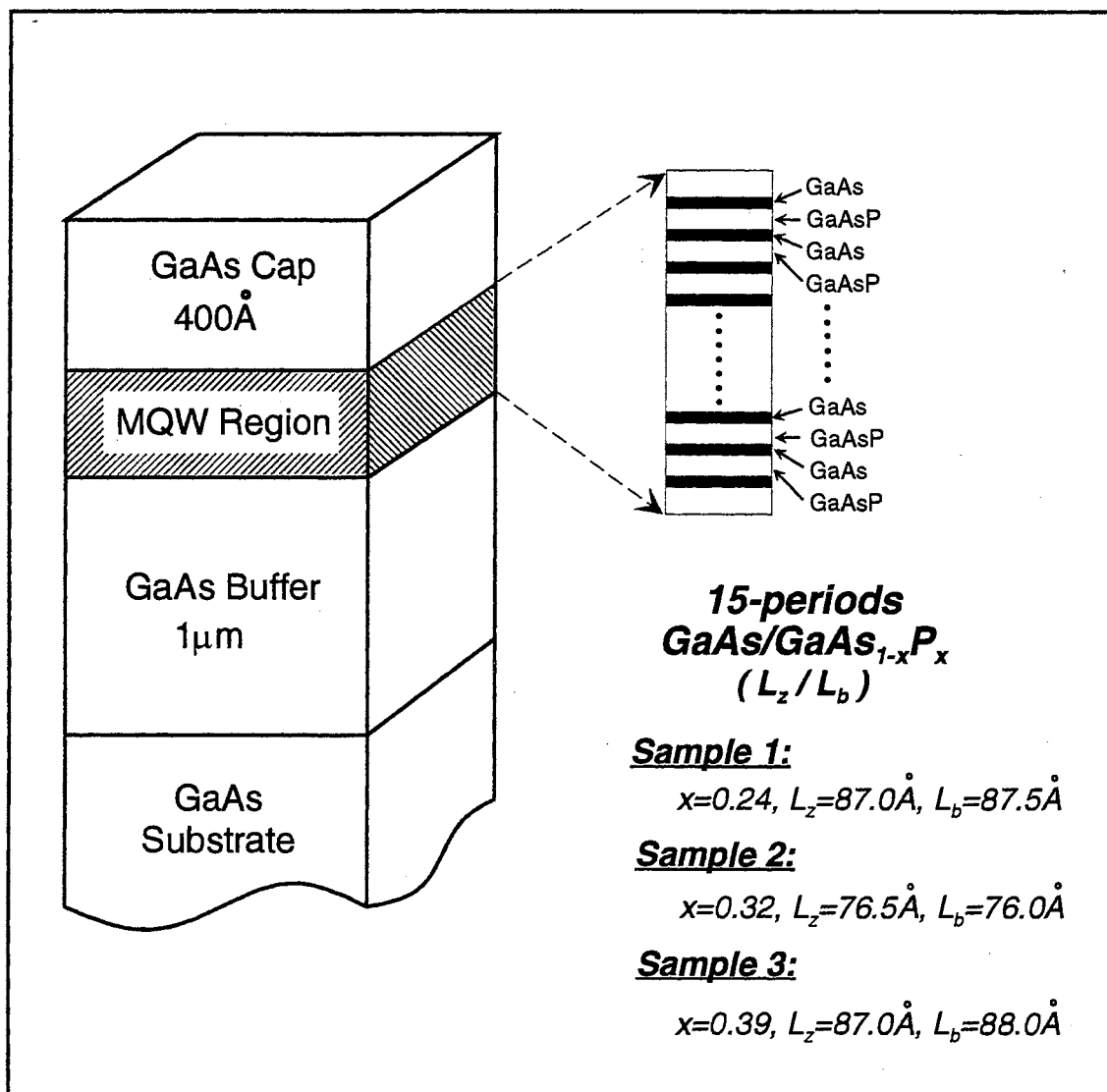


Figure 17. Schematic illustration of the GaAs/GaAs_{1-x}P_x MQW structure.

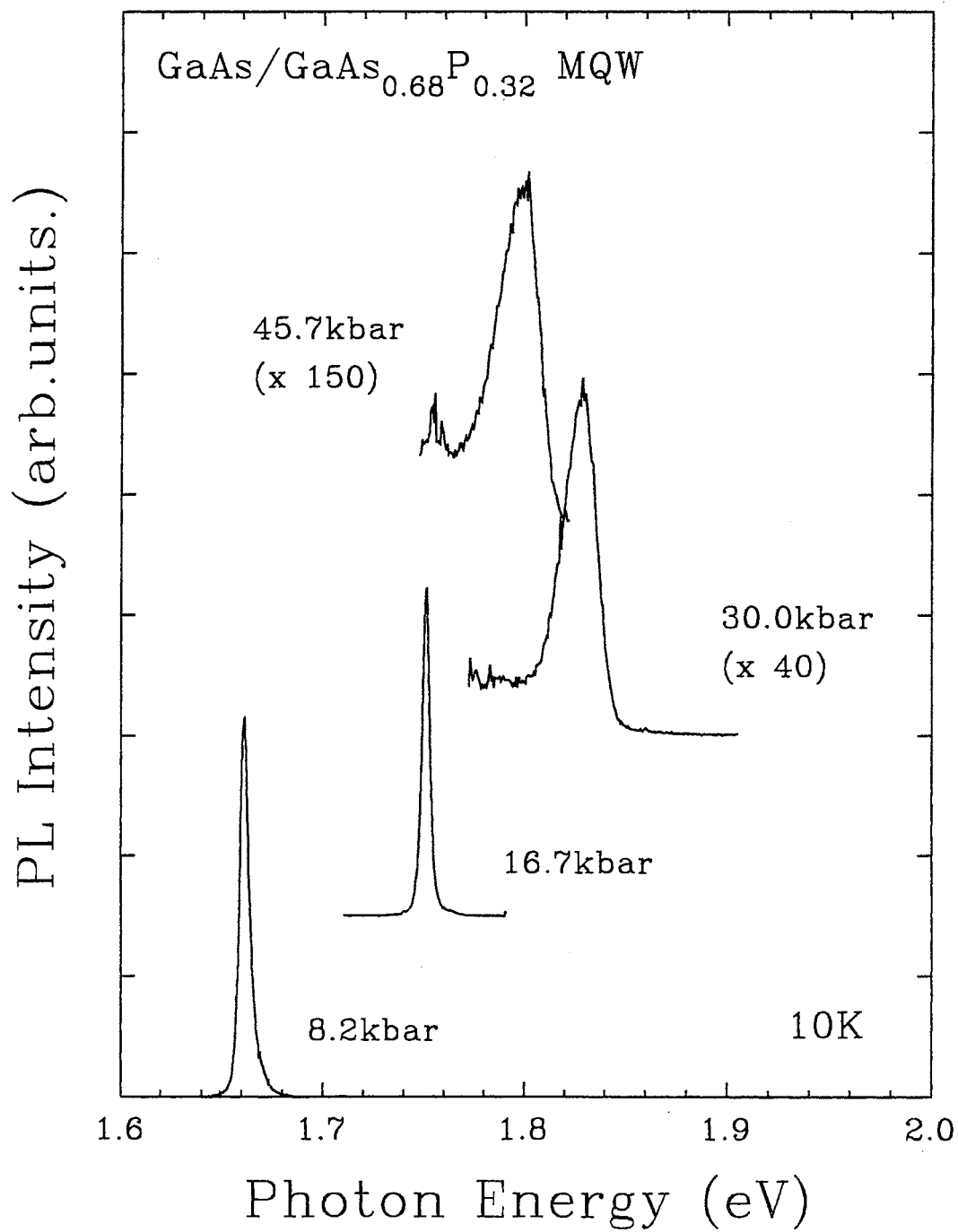


Figure 18. Photoluminescence spectra at 10 K of the GaAs/GaAs_{0.68}P_{0.32} MQW's at different pressures. The emission from the $\Gamma - \Gamma$ confined transition shifts to higher energy with pressure and diminishes around 26 kbar and the broadened emission from the $X - \Gamma$ transition takes over and moves down in energy as the pressure increases.

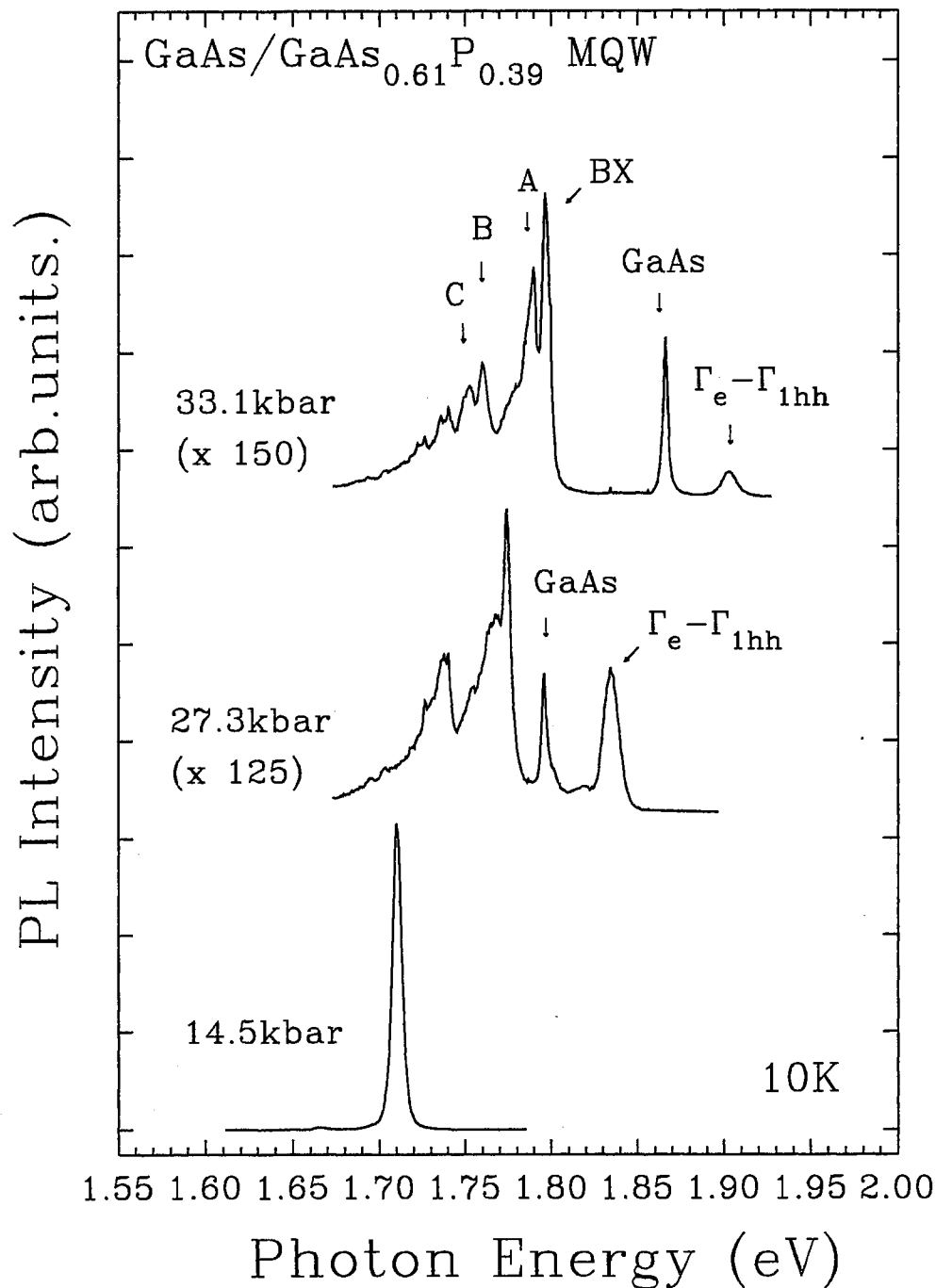


Figure 19. Photoluminescence spectra at 10 K of the GaAs/GaAs_{0.61}P_{0.39} MQW's at different pressures. The emission labeled by *BX* and its satellite sideband structures, marked with *A*, *B* and *C*, appear at pressures higher than 17 kbar. The emission from the Γ -band of the GaAs substrate could also be observed in this sample.

$\Gamma_{1e}-\Gamma_{1hh}$ and E_{11h} , respectively. As can be seen in the figures, typical $\Gamma_{1e}-\Gamma_{1hh}$ excitonic transitions are dominant in the low pressure range. The full width at half maximum (FWHM) of the $\Gamma_{1e}-\Gamma_{1hh}$ emission peaks at ambient pressure is about 6 meV.

The strong and sharp luminescence of the $\Gamma_{1e}-\Gamma_{1hh}$ transitions shifted towards higher energy as pressure was increased. For the GaAs/GaAs_{0.68}P_{0.32} SMQW as shown in Fig. 18, the PL peak begins to broaden and the emission intensity decreases sharply at a pressure around 26 kbar. At higher pressures, the emission associated with $\Gamma_{1e}-\Gamma_{1hh}$ transition quenches, and a broader and much weaker peak appears. This new broad peak moves down in energy as the pressure is increased, exhibiting *X*-band-like characteristics. As we discussed in an earlier chapter, what is happening might be related to the crossover of band edges in the conduction bands which results in a sharp decrease of the PL intensity and/or the appearance of a new transition which moves towards lower energy.

As shown in Fig. 19, a relatively strong emission peak (labeled *BX*) with a satellite sideband appeared at pressures higher than 17 kbar in the GaAs/GaAs_{0.61}P_{0.39} SMQW sample. The *BX* emission peak has a sharp high-energy cutoff and shifts to higher energy with pressure at a relatively small rate compared to the peak of the $\Gamma_{1e}-\Gamma_{1hh}$ transition. However, within the sensitivity of the detection system, no emission with pure *X*-like characteristics could be observed from this sample or from the GaAs(87 Å)/GaAs_{0.76}P_{0.24}(87.5 Å) SMQW sample.

In Fig. 20 and Fig. 21, we plot the energy position of the $\Gamma_{1e}-\Gamma_{1hh}$ transition as function of pressure from the GaAs/GaAs_{0.68}P_{0.32} and GaAs/GaAs_{0.61}P_{0.39} SMQW samples, respectively. The solid lines drawn through the data points are least-squares fits to the experimental data. The pressure dependence of the Γ and *X*-conduction band minima of bulk GaAs is also plotted for the comparison in Fig. 20. The onset of the unknown emission structure *BX* in Fig. 19 can be derived from the figure to be ~ 17 kbar.

Fig. 22 shows a PLE spectrum from a 15-period GaAs/GaAs_{0.61}P_{0.39} SMQW

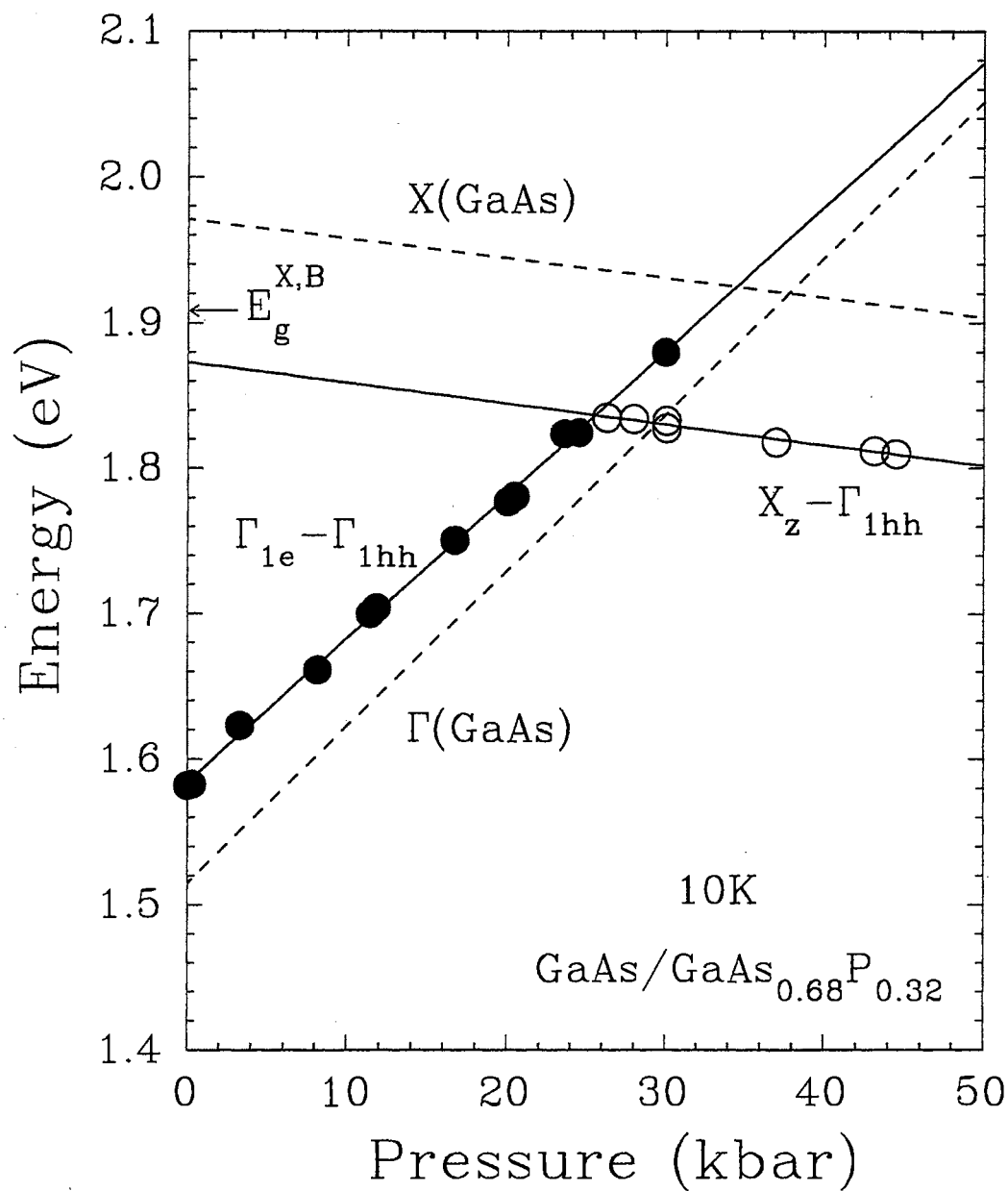


Figure 20. Pressure dependence of various photoluminescence peaks observed in the GaAs/GaAs_{0.68}P_{0.32} SMQW. The solid lines drawn through the points are least-squares fits to the experimental data. Also shown are the pressure dependence of the X conduction-band edges of GaAs. The energy position of the X_z minima of the GaAs/GaAs_{0.68}P_{0.32} barriers at ambient pressure, as indicated by $E_g^{X,B}$ in the figure, is 1.908 eV.

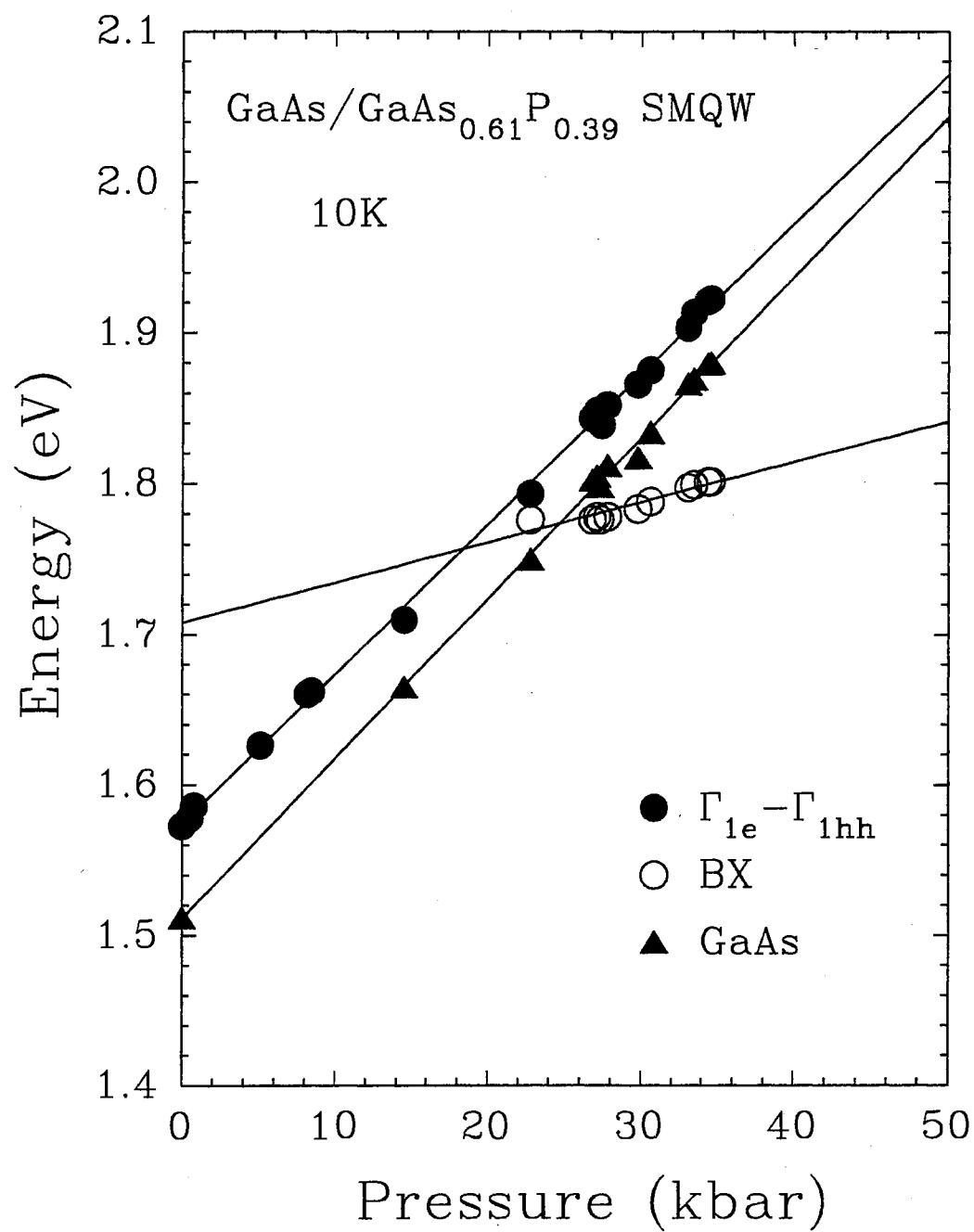


Figure 21. Pressure dependence of various photoluminescence peaks observed in the GaAs/GaAs_{0.61}P_{0.39} SMQW. The solid lines drawn through the points are least-squares fits to the experimental data.

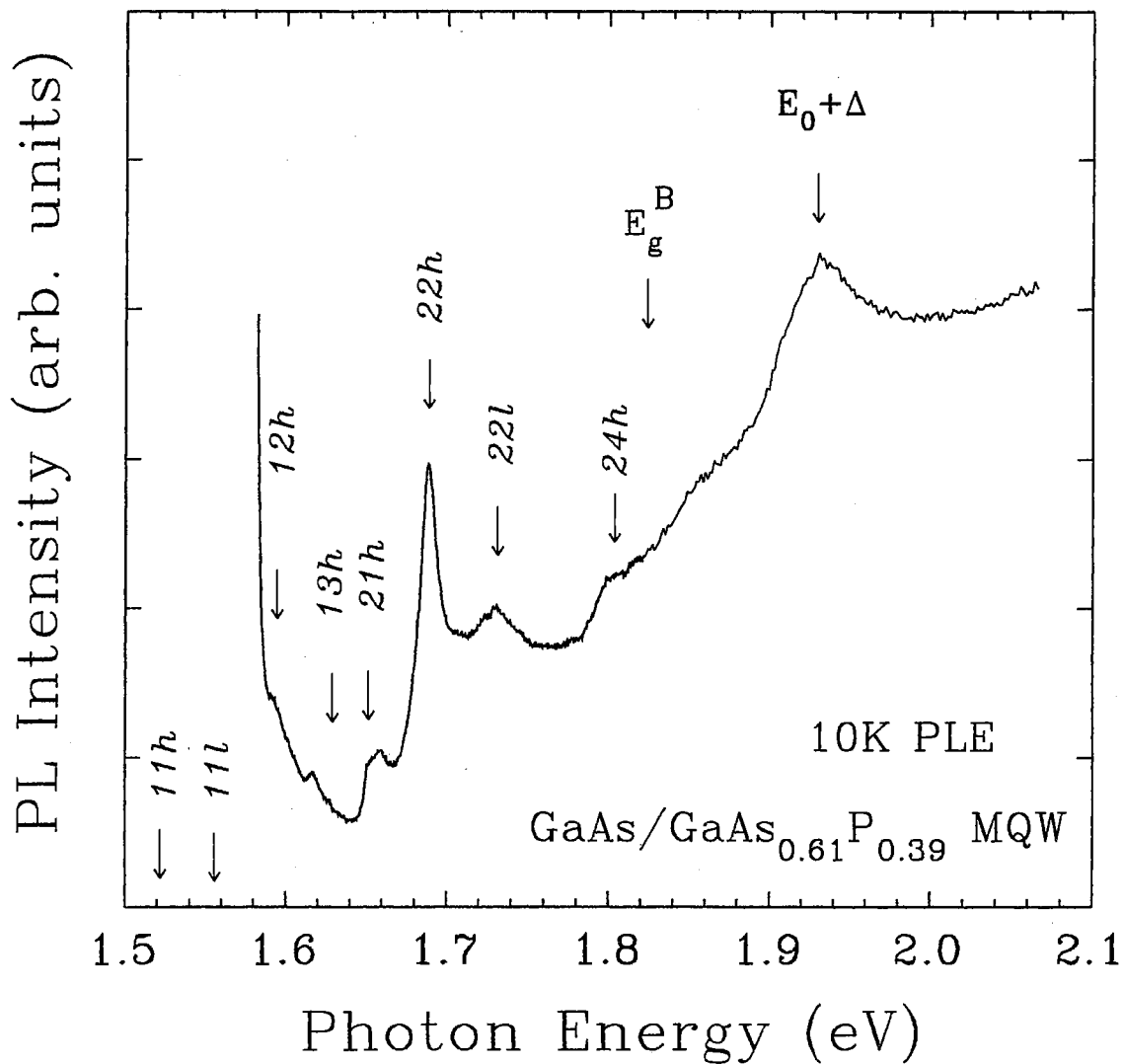


Figure 22. Photoluminescence excitation (PLE) spectra taken at 10 K from the GaAs/GaAs_{0.61}P_{0.39} MQW. The arrows corresponds to the calculated interband transitions. E_g^B is the energy gap of the GaAs_{0.61}P_{0.39} barrier.

sample taken at 10 K. The detection wavelength was set at the wavelength corresponding to the $\Gamma_{1e}-\Gamma_{1hh}$ transition energy. The excitonic transitions related to higher quantum confined energy levels are well resolved. The results are compared with the calculations based on the envelope function approximation.

Analysis and discussion

In the GaAs/GaAs_{1-x}P_x system grown commensurately on GaAs substrates, GaAs_{1-x}P_x layers are subject to a biaxial tensile strain due to the larger lattice constant in GaAs. Using Eq. (6), the built-in strains of GaAs_{1-x}P_x layers were estimated as 0.87, 1.16, and 1.42 % in the lattice mismatch for $x = 0.24, 0.32,$ and $0.39,$ respectively. As mentioned earlier, the effect of the built-in biaxial tensile strain on the GaAs_{1-x}P_x band structure at the Γ -point is to reduce the direct band gap and lift the degeneracy of the top of the valence band, where the light-hole band lies in energy above the heavy-hole band. The six equivalent X_1 bulk conduction band minima are split by (001) strain with the two equivalent band minima X_z (for k perpendicular to the interface, [001] singlet band) lower than the four equivalent band minima X_{xy} (for k along the interface, [100,010] doublet band). Fig. 23 shows a schematic representation of the band-edge energies for the strained GaAs/GaAs_{0.68}P_{0.32} heterostructure under the condition of biaxial tension. The x -dependence of the unstrained band gaps of GaAs_{1-x}P_x alloy are given as [75]

$$E_{\Gamma}^0(x) = 1.515 + 1.172x + 0.186x^2 \quad (\Gamma\text{-band, } T=2\text{K}), \quad (76)$$

and

$$E_X^0(x) = 1.9715 + 0.144x + 0.211x^2 \quad (X\text{-band, } T=2\text{K}). \quad (77)$$

As described in Chapter II, the confined energy levels in the well are calculated using the envelope function approximation with the band gap energy of the GaAs_{1-x}P_x barrier modified due to the strain. For this calculation for the confinement energies, we also need to have the band offsets in both conduction and valence bands. The band offset values will be obtained from the experimental

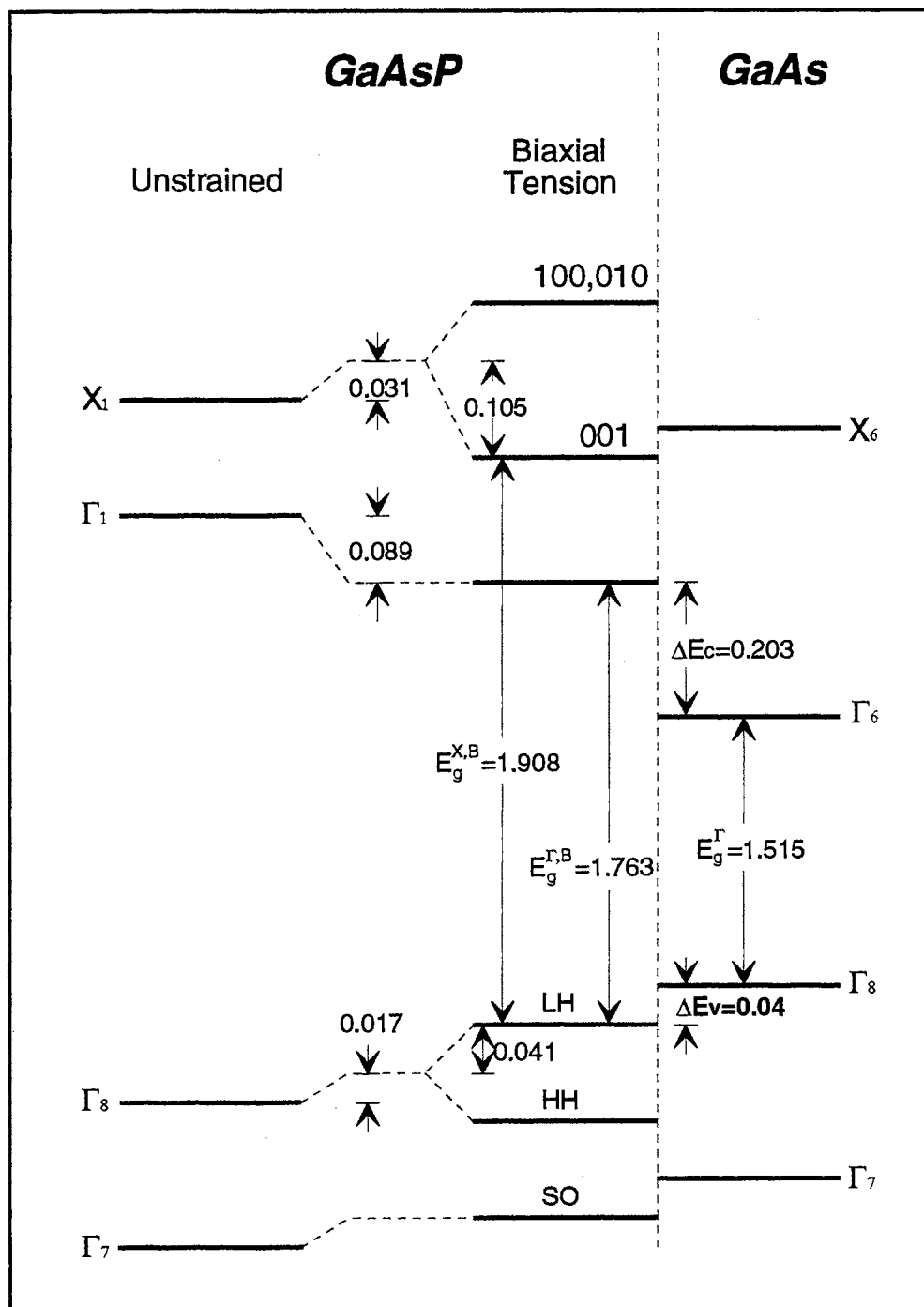


Figure 23. A schematic representation of the band-edge energies for the strained GaAs/GaAs_{0.68}P_{0.32} heterostructure under the condition of (001) tension. Light-hole band is above the heavy-hole band. The numbers are obtained from the deformation potential they described in Chapter II. The band offset values are from the experimental results discussed later.

results. Parameters used in the calculations are listed in Table I for GaAs and GaP.

Energy level crossover and valence band offset

There are two primary possible reasons for the reduction of the PL intensity associated with a direct QW transition as the pressure increases. First, the band gap of the well material itself becomes indirect by undergoing pressure induced $\Gamma^W - X^W$ conversion, while the QW structure still remains in Type-I. Second, the band gap of the well material still remains in direct gap, but the conduction band edge of the barrier material X^B crosses the lowest Γ -confined electron state of the well $1e$ thereby causing the QW to become indirect both in real and in momentum space (see Fig. 10b). If the critical hydrostatic pressures associated with conduction band crossing in both well and barrier material have been independently determined in bulk, then one can immediately determine whether the drop in the direct PL intensity from the QW structure is due to the first or second effect. If the sharp reduction of the PL intensity is caused by the second effect, one can obtain the information on the band alignment in QW structures.

Here $E_g^{X,B}$ is the energy of barrier X_z minima, E_{ex}^b is the exciton binding energy, and E_{1hh} is the confinement energy of the lowest heavy-hole state in the wells. Since the pressure coefficient of the X -minima of the $\text{GaAs}_{1-x}\text{P}_x$ alloy is not available at present, we use the values of E_{ex}^b and E_{1hh}^X at ambient pressure for estimating the band offset. The band offset calculation using the pressure induced $\Gamma - X$ crossover is illustrated in Fig. 24.

As seen in Fig. 20, the crossover pressure (~ 26 kbar) observed in GaAs/GaAs_{0.68}P_{0.32} sample is much lower than the Γ - X band crossing in the bulk GaAs (~ 40 kbar). This suggests that the applied pressure caused the lowest confined electron state in the GaAs wells Γ_{1e}^W to cross over the X -minima in the GaAs_{0.68}P_{0.32} barriers X^B (i.e., $X^B - \Gamma_{1e}^W$ transition) and resulted in a spatially separated Type-II indirect transition. Fig. 24 shows the band lineups for the GaAs/GaAs_{0.68}P_{0.32} SMQW before and after the pressure induced $\Gamma - X$ crossover. Therefore, the

TABLE I.

Parameters used for the calculations for GaAs/GaAs_{0.68}P_{0.32} SMQW. For the values of the GaAs_xP_{1-x} alloy layers are obtained using linear interpolation of values from GaP and GaAs.

Parameters	GaAs	GaP
a (Å)	5.6533*	5.4505*
C_{11} (10^{11} dyn/cm ²)	12.21*	14.39*
C_{12} (10^{11} dyn/cm ²)	5.7*	6.52*
a (eV)	-8.33†	-8.83†
b_v (eV)	-1.90†	-1.5†
a_X	1.0†	1.6‡
Ξ_u^X (eV)	-8.61*	-6.5‡
m_e^* (emu)	0.067*	0.0925*
m_{hh}^* (emu)	0.51*	0.45*
m_{lh}^* (emu)	0.082*	0.12*
γ_1	6.95*	4.05*
γ_2	2.25*	0.49†

*Ref. [75]

†Ref. [23]

‡Ref. [76]

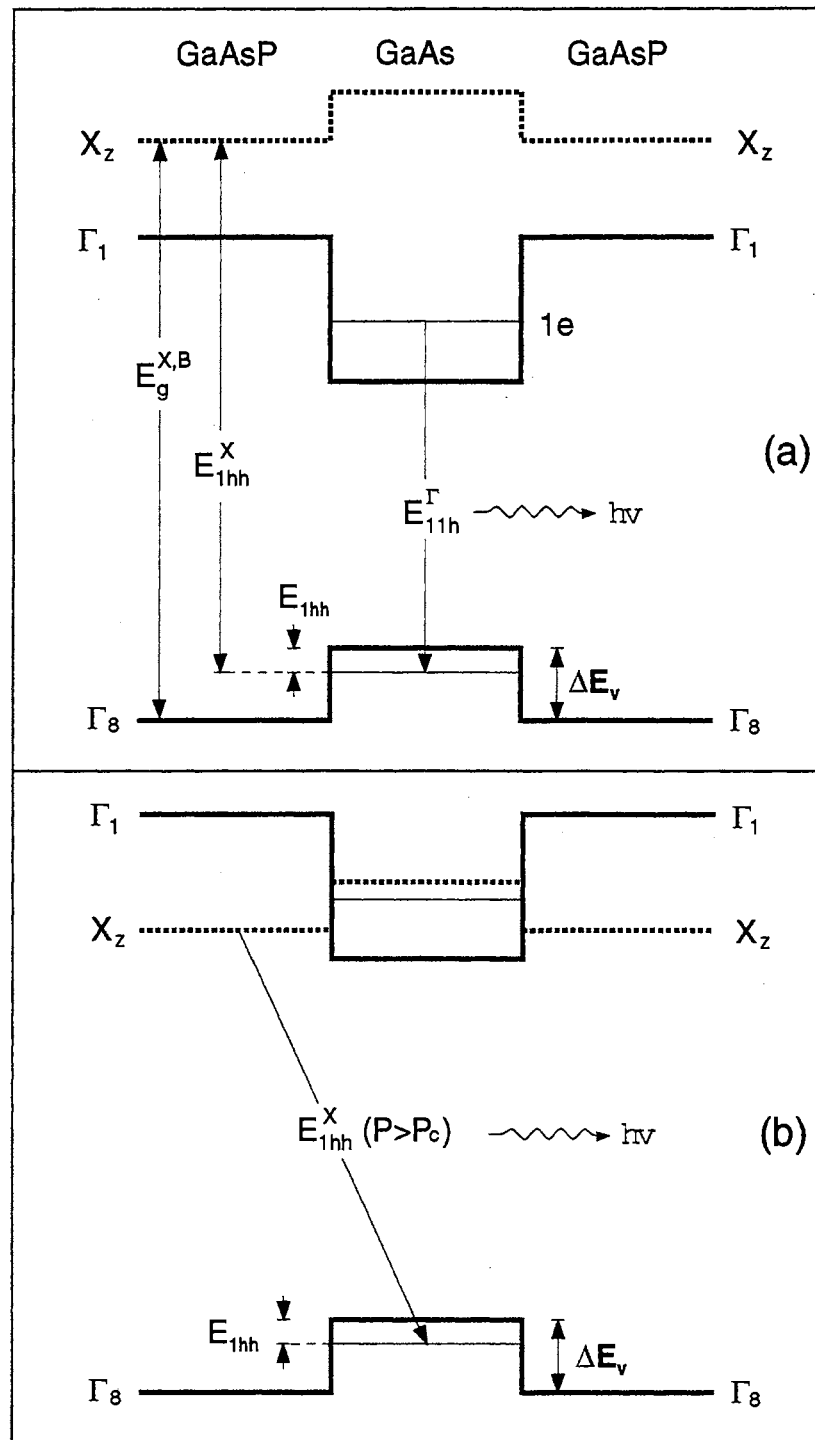


Figure 24. Band alignments of the strained GaAs/GaAs_{0.68}P_{0.32} quantum well (a) before and (b) after the crossover pressure, P_c . The direct Type-I transition with energy of E_{11h}^Γ shown in (a) converts to the spatially separated Type-II transition with the energy of E_{11h}^X shown in (b) at pressures $P > P_c$.

pressure induced $\Gamma - X$ crossover in the GaAs/GaAs_{0.68}P_{0.32} SMQW sample can be used to determine its valence band offset using the Eq. (70):

$$\Delta E_v = E_g^{X,B} - E_{PL}^X - E_{ex}^b + E_{1hh}, \quad (78)$$

where

$$E_{PL}^X = E_{1hh}^X - E_{ex}^b. \quad (79)$$

Here E_{PL}^X is the observed PL transition energy associated with X_z^B and Γ_{1hh}^W levels. The energy of the X_z -minima of the GaAs_{0.68}P_{0.32} barriers, $E_g^{X,B}$, was calculated to be 1.908 eV at ambient pressure. Since the pressure coefficient of the X -minima of the GaAs_{1-x}P_x alloy is not available at present, we use the values of E_{ex}^b and E_{PL}^X at ambient pressure for estimating the band offset. E_{PL}^X ($P = 0$) was estimated to be 1.87 eV by extrapolating the $X_z - \Gamma_{1hh}$ transitions observed above the crossover pressure back to the ambient pressure, as shown in Fig. 20. This indirect Type-II transition is almost impossible to observe at ambient pressure. The confinement energy of the lowest heavy-hole level (E_{1hh}) was found to be about 12 meV using the calculation based on the envelope function approximation. By considering that the binding energy for the $\Gamma_{1e} - \Gamma_{1hh}$ exciton was about 10 meV and that binding energy for the $X_z - \Gamma_{1hh}$ exciton would be even smaller due to the spatial separation of the electrons and holes [39,77], the $X_z - \Gamma_{1hh}$ exciton binding energy E_{ex}^b was estimated to be 5 meV. Using these data we were able to obtain the band discontinuity between the top of the valence band of the GaAs well and the light-hole valence band of the GaAs_{0.68}P_{0.32} barrier as $\Delta E_v \approx 0.045$ eV, where we have subtracted 5 meV to take into consideration the Stokes shift detected between the PL emission peak and the PLE emission peak. The uncertainty introduced in the calculations of the strain modified band structure of the GaAs_{0.68}P_{0.32} barrier and the confinement energy of the heavy hole in GaAs, as well as in estimating the exciton binding energy, was about 20 meV. As a result, this led to an unstrained free-standing band lineup with a valence-band offset of 0.09 ± 0.02 eV between GaAs and GaAs_{0.68}P_{0.32}. This is approximately a 75:25 distribution for the energy gap

difference in the conduction and valence bands, so that, the valence band offset ratio, $Q_v = \Delta E_v / \Delta E_g = 0.25$.

Although this method results in some uncertainties in the value of the valence band offset from the above estimation and the calculated confinement energies, it allows us to compare our results with earlier reported values by Gourly *et al.* [19] and Pistol *et al.* [22]. Pistol *et al.* chose the unstrained valence-band offset to be 5 meV per percentage of phosphorus in the GaAs/GaAs_{1-x}P_x QW's [22] and Gourly *et al.* chose the offset value to be a linear interpolation with x , within a value of 600 meV, between GaAs and GaP [19]. Using their data, one gets an unstrained valence band offset of 0.16 ~ 0.19 eV for the GaAs/GaAs_{0.68}P_{0.32} QW. Compared to our result of 0.09 eV, the deviation is rather large. The methods used in Refs. [19] and [22] were to fit PLE data by treating the band offset as a fitting parameter and/or to make an evaluation based on the model-solid theory [78]. Thus the results are indirect and model dependent. The pressure-optical method used in this work is a direct and more accurate measurement which does not introduce any model-dependent parameters, and has been widely used for the determination of band offsets in a number of III-V compound MQW systems [13,40,38,39,43]. This method allows a direct measurement of the $\Gamma - X$ band crossing between the lowest confined level in the Γ -band of the GaAs well and the X -conduction band edges of the GaAs_{1-x}P_x barriers. Since the bands cross in a narrow range of energies, this pressure-optical method provides more accurate data for deducing the band offset of MQW's. Since the electrical and electron-spectroscopic approaches such as the capacitance-voltage ($C-V$) profiling [79], current-voltage ($I-V$) measurement [80], and x-ray photoelectron spectroscopy (XPS) [81] usually require fairly thick heterostructures, the pressure-optical method is particularly suitable for strained semiconductor heterostructures where the sample thickness often must be very thin in order to ensure commensurate growth.

Pressure coefficients and identification of unknown transitions

In Fig. 20 and Fig. 21, the solid lines drawn through the data points are least-squares fits to the experimental data. The pressure dependence for the different PL transition energies observed in each sample can be obtained from the experimental data using linear least-squares fitting as expressed by

$$E_i(P) = E_i(0) + \alpha_i P, \quad (80)$$

where i denotes different transitions and the linear pressure coefficient $\alpha_i = dE_i/dP$. Also, $E_i(P)$ and $E_i(0)$ are transition energies at the pressure P and at ambient pressure, $P = 0$. The pressure dependence of the Γ and X -conduction band minima of bulk GaAs is also plotted in Fig. 20 for comparison. The onset of the unknown emission structure BX in Fig. 19 is found to be ~ 17 kbar. Table II lists the linear pressure coefficients of all transition energies for all the samples studied in this work as obtained from Eq. (80). It is noteworthy that the pressure coefficients of the Γ_{1e} - Γ_{1hh} transition in all three samples are significantly smaller than that of the GaAs bandgap and depend on the phosphorus compositions of the barriers and QW structures. Similar results have been reported and well discussed in the previous pressure dependent optical measurements on a variety of III-V compound QW structures [13,38,41–45,47]. As seen in Table II, the emission labeled as BX in the PL spectrum from the GaAs/GaAs_{0.61}P_{0.39} SMQW sample shown in Fig. 19 has a small positive pressure coefficient of 2.7 meV/kbar. This pressure dependence does not follow any known conduction-band edge in these bulk materials.

The energy separations of the satellite peaks marked by A , B , and C in Fig. 19 with respect to the main emission BX peak are about 10, 36.5 and 46.5 meV, respectively, which approximately agree with the TA^X (9.8 meV), LO^Γ (36.2 meV), and $LO^\Gamma + TA^X$ phonons of GaAs. The slight energy differences could be attributed to the effect of hydrostatic pressure. Pistol and Liu have studied the Raman shift for optical phonons of GaAs_{1-x}P_x in strained QW structures [22].

TABLE II.

Pressure coefficients of various PL transitions in the GaAs/GaAs_xP_{1-x} SMQW samples studied in this work. The pressure coefficients of the Γ and X bands are also listed for comparison (the units are in meV/kbar).

Samples	$dE_{\Gamma-\Gamma}/dP$	$dE_{X-\Gamma}/dP$	dE_{BX}/dP
GaAs(87Å)/GaAs _{0.76} P _{0.24} (87.5Å)	9.5(5)	-	-
GaAs(76.5Å)/GaAs _{0.68} P _{0.32} (76Å)	9.9	-1.4(5)	-
GaAs(87Å)/GaAs _{0.61} P _{0.39} (88Å)	9.9(5)	-	2.7
GaAs	10.7;10.73*	-1.34*	-

*Ref. [82]

The Raman spectra of the $\text{GaAs}_{1-x}\text{P}_x$ alloys exhibited a two-mode behavior and the frequency of GaAs-like LO phonon decreased with the increase of the alloy concentration. They also found that the GaAs-like LO phonon in the strained $\text{GaAs}_{1-x}\text{P}_x$ alloy layers shifted to lower frequency due to the strain effect.

Examining closely the satellite sidebands of the BX emission in the PL spectra, we could not observe any significant feature clearly related to the frequency red-shifted GaAs-like LO phonon in the $\text{GaAs}_{1-x}\text{P}_x$ barrier layers. This suggests that the deep donor centers reside in GaAs wells rather than in $\text{GaAs}_{0.61}\text{P}_{0.39}$ barriers. By extrapolating the experimental data to the ambient pressure as shown in Fig. 19, it is found that this donor-like deep center is a resonance with about 200 meV above the bottom of the conduction band.

The behavior of this deep center is in some ways similar to the so-called DX deep donor center in n -doped GaAs [83–87]. Where n -type substitutional dopants give rise to a shallow effective-mass level and a much more localized resonant level, an application of about 20 kbar hydrostatic pressure can shift DX from a resonant to a stable state. The pressure coefficient of the DX -like deep donors in S -doped bulk GaAs is reported by Liu *et al.* to be 1 meV/kbar [87] compared to 2.7 meV/kbar for the BX emission. If the centers responsible for the BX emission are DX -like, such a difference in the pressure coefficients could be attributed to deep centers that originate from different impurity species with different resultant energy positions and pressure dependence.

Detailed secondary-ion mass spectrometry (SIMS) analysis [88] revealed that there were carbon and silicon as well as oxygen impurities present in the samples which showed BX emission and its phonon sidebands. The concentration of each species was found to be less than 10^{15} cm^{-3} by the SIMS analysis. They were introduced into the SMQW samples mainly from the arsenic gas source (AsH_3) during the sample growth [88] and were most likely responsible for the presence of the resonant donor-like deep centers.

The presence of such deep centers could be the reason why the pure PL emission related to Type-II $X_z-\Gamma_{1hh}$ transition at pressures above Γ - X crossover could

not be observed in both GaAs/GaAs_{0.76}P_{0.24} and GaAs/GaAs_{0.61}P_{0.39} SMQW's. The localized deep centers can efficiently capture those cross-interface electrons with X -characteristics through nonradiative relaxation processes such as multiphonon emission since their wave functions derived from contributions of the entire Brillouin zone. This process will increase the k -space overlap of the wave functions of the spatially separated electrons and holes and results in a recombination via these deep centers which has a larger oscillator strength compared with the purely cross-interface indirect X - Γ recombination.

As shown in Fig. 22, the PLE spectrum from a 15-period GaAs/GaAs_{0.61}P_{0.39} SMQW sample was compared with the results of the theoretical calculations for the confinement energy for this sample. The valence band offset was used as the adjustable parameter in the calculation. The theoretical calculation results are indicated with arrows corresponding to the interband transitions of the QW. The notation $11h$ means the transition is between $n = 1$ electron state and $n = 1$ heavy-hole state. The notation h (l) is for a heavy-hole (light-hole). Another clear transition, denoted as $E_0 + \Delta$, is also observed in the PLE spectrum at 1.93 eV, which is higher than the band gap of the barrier marked by E_g^B at 1.82 eV. This transition is attributed to the transition between the lowest confined electron subband and the top of the spin-orbit split-off band in the GaAs well.

Conclusions

Low-temperature photoluminescence measurements have been performed on GSMBE grown GaAs/GaAs_{1-x}P_x SMQW samples to investigate the effect of pressure on the properties of various transitions using a diamond anvil high-pressure cell. In general, the transitions between the lowest confined electron and hole levels ($\Gamma_{1e} - \Gamma_{1hh}$) for all the samples studied in this work are found to depend on pressure in a way similar to the GaAs band gap but with smaller pressure coefficients. The observation of the pressure induced Γ_{1e} - X_z crossover allows a direct determination of the valence-band offset for the GaAs/GaAs_{0.68}P_{0.32} SMQW sample. The

unstrained valence-band offset has been determined to be 0.09 ± 0.02 eV which corresponds to roughly a 75:25 band offset ratio of conduction band to valence band and yields a Q_v value of 0.25. We have also observed an emission associated with a deep center in the GaAs/GaAs_{0.61}P_{0.39} SMQW sample. By analyzing the pressure dependence of this emission and its phonon sidebands, we suggest that the deep center is a donor-like localized state inside the GaAs well layer with a resonant energy position at about 200 meV above the bottom of the conduction band at ambient pressure. These deep centers, by acting as capture centers for the cross-interface electrons, could be the major reason for not observing the Γ - X crossover in GaAs/GaAs_{1-x}P_x SMQW samples with $x=0.24$ and 0.39 . Further more, we can not directly obtain crossover pressures for the other GaAs/GaAs_xP_{1-x} samples because the pressure coefficients and transition energies at ambient pressure for those GaAs_xP_{1-x} barriers are unknown. However, the drastic decrease of the emission intensity in a certain range of pressures may indicate the occurrence of the $\Gamma - X$ crossover for these samples.

CHAPTER V

InAs_xP_{1-x}/InP STRAINED MULTIPLE QUANTUM WELLS

Introduction

In_{1-x}Ga_xAs_yP_{1-y} quaternary alloys grown on InP have been extensively studied as promising materials for optoelectronic device applications such as light emitting diodes and detectors operating in the 1.3~1.6 μm wavelength range [89-92,74]. This material system is also of great interest for both theoretical and experimental studies, particularly concerning the lattice mismatch induced strain. However, there have been relatively few studies on the optical properties in the pseudomorphic InAs_xP_{1-x}/InP system which is a special case of the InGaAsP/InP system [93-96].

In this chapter, we present an investigation of the optical transitions between confined states in InAs_xP_{1-x}/InP strained multiple quantum wells (SMQW) using low temperature PL and PLE, and room temperature PT measurements under pressure. The observed excitonic interband transitions were compared with calculations based on the envelope function approximation [5,6], and phenomenological deformation potential theory [23,76]. The band nonparabolicity and strained induced valence band mixing were included in the calculations, which enabled identification of spectral structures related to the high-order ($n \geq 2$) optical transitions.

Experiments

Sample preparations

Two $\text{InAs}_x\text{P}_{1-x}/\text{InP}$ SMQW structures were grown by gas-source molecular beam epitaxy (GSMBE) on (100) Fe-doped semi-insulating InP substrates after a 1 μm -thick InP buffer layer (see Fig. 25). A 400 Å InP cap layer was grown on the SMQW structure. The sample parameters, such as the well alloy compositions and dimensions, were characterized by cross-sectional transmission electron microscopic (TEM) images and high resolution x-ray rocking curves [97]. As shown in Fig. 25(b), sample 1 has a simple MQW structure of 16-periods of $\text{InAs}_{0.6}\text{P}_{0.4}$ alloy as wells (78 Å) and InP as barriers (144 Å). Sample 2, on the other hand, has a more complicated structure for the well. As shown in Fig. 25(c), sample 2 has 15-periods of $[\text{InAs}/\text{InP}](76 \text{ Å})/\text{InP}(162 \text{ Å})$ QW's. The well layer in sample 2 has the InAs/InP short-period superlattice structure which is 5-periods of 2.5-monolayer InAs and 2.5-monolayer InP. The short-period superlattice well layer can be considered as an equivalent to $\text{InAs}_x\text{P}_{1-x}$ alloy with effective As concentration by averaging the thicknesses of the well and barrier. For our sample case, since the short-period superlattice well layer has same thicknesses of well and barrier, the well can be considered as $\text{InAs}_x\text{P}_{1-x}$ alloy well with $x = 0.5$. If the short-period superlattice well layer has different thicknesses of well and barrier, then the effective alloy concentration x will be different from 0.5. For convenience, the short-period SL well layer will be denoted as the $\text{InAs}_{0.5}\text{P}_{0.5}$ alloy layer. Detailed growth conditions and sample structures can be found elsewhere [97]. The sample parameters for both samples are summarized in Table III.

Experimental technique

PL and PLE measurements at low temperature, and PT measurements under hydrostatic pressure at room temperature were employed to study the interband transitions in these samples. A 15 mW He-Ne laser was used as an excitation source

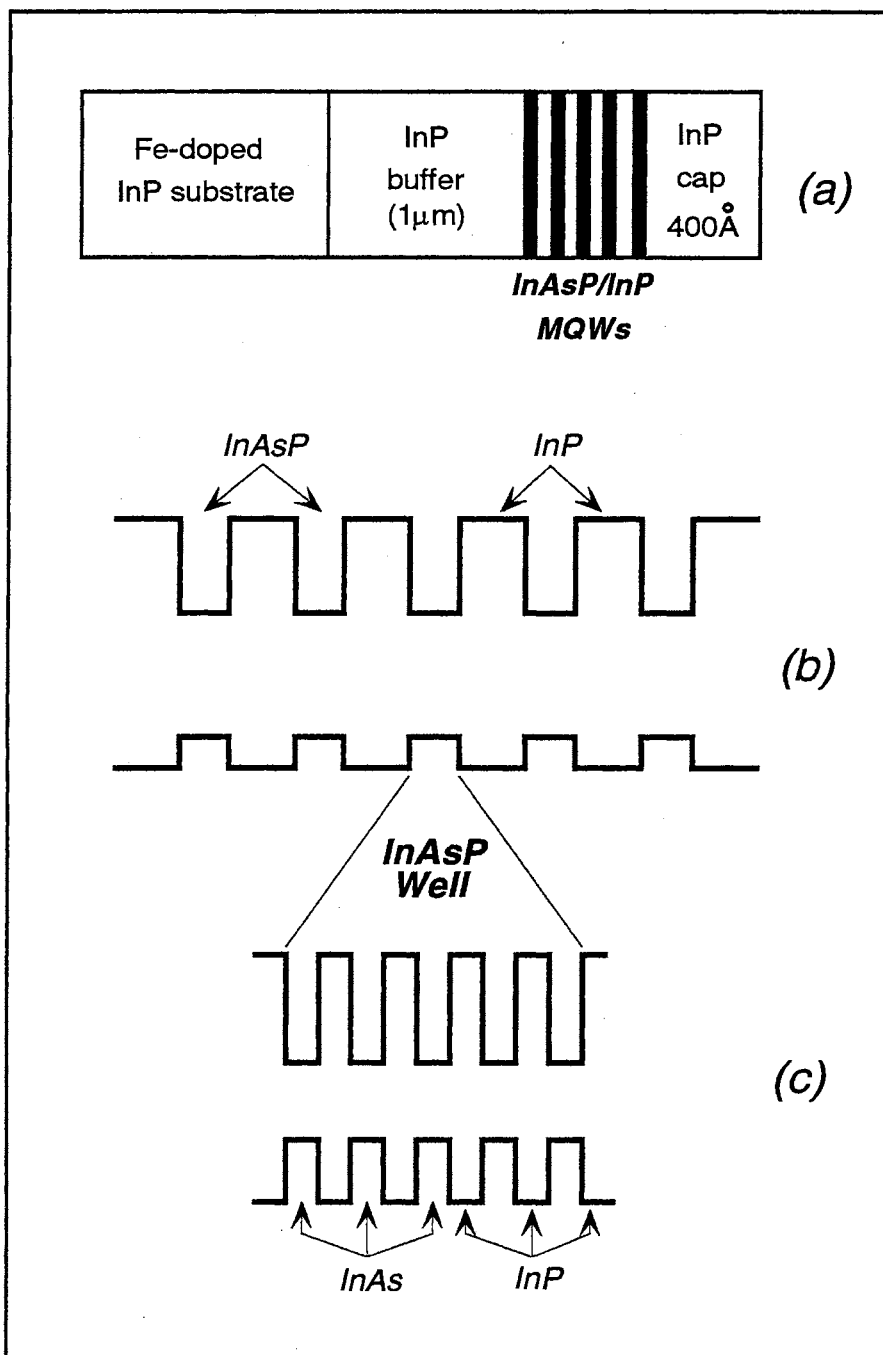


Figure 25. Schematic representation of $\text{InAs}_x\text{P}_{1-x}/\text{InP}$ strained multiple quantum well (SMQW) structure. Sample 1 has normal InAsP alloy as the well layer (b), but sample 2 has short-period superlattice structure as the well layer (c). This short-period SL structure is composed of 5 period of alternating 2.5 ML-InAs and 2.5 ML-InP layers by resulting the SL layer as the same as $x = 0.5$ of the $\text{InAs}_x\text{P}_{1-x}$ alloy layer.

TABLE III.

Sample parameters of InAsP/InP strained multiple quantum wells.

Parameters	Sample 1	Sample 2
Well structure	InAsP alloy	InAs/InP short-period SL*
InAsP well width	78 Å	76 Å
InP barrier width	144 Å	162 Å
As concentration	0.6	0.5 (averaged)
MQW period	15	16

$$*\text{InAs/InP short-period SL} = [\text{InAs}(2.5 \text{ ML})/\text{InP}(2.5 \text{ ML})] \times 5$$

for the PL measurement and also as a modulation source for the PT measurement. Continuous light from a 250 W quartz tungsten halogen lamp dispersed by a 0.25 m monochromator (CVI 250) with a 600 gr/mm grating was used as a tunable excitation source for both PLE and PT measurements. For the PL measurement, a 0.5 m monochromator (Aries IS/MS 550) was used for collecting signals from the samples. Both luminescence and transmission signals were detected by a thermoelectrically cooled Ge photodiode detector (EG&G Judson, 0.8-1.8 μm) followed by a lock-in amplifier and data acquisition system.

Results and discussion

Fig. 26 shows PL and PLE spectra of these two samples taken at 10 K. As shown in the figure, sharp and intense PL peaks were observed with the full width at half maximum (FWHM) of ~ 9 and ~ 20 meV for $\text{InAs}_{0.6}\text{P}_{0.4}/\text{InP}$ and $\text{InAs}_{0.5}\text{P}_{0.5}/\text{InP}$ SMQW samples, respectively. These transitions are attributed to the transition between the lowest confined electron and heavy-hole states in the

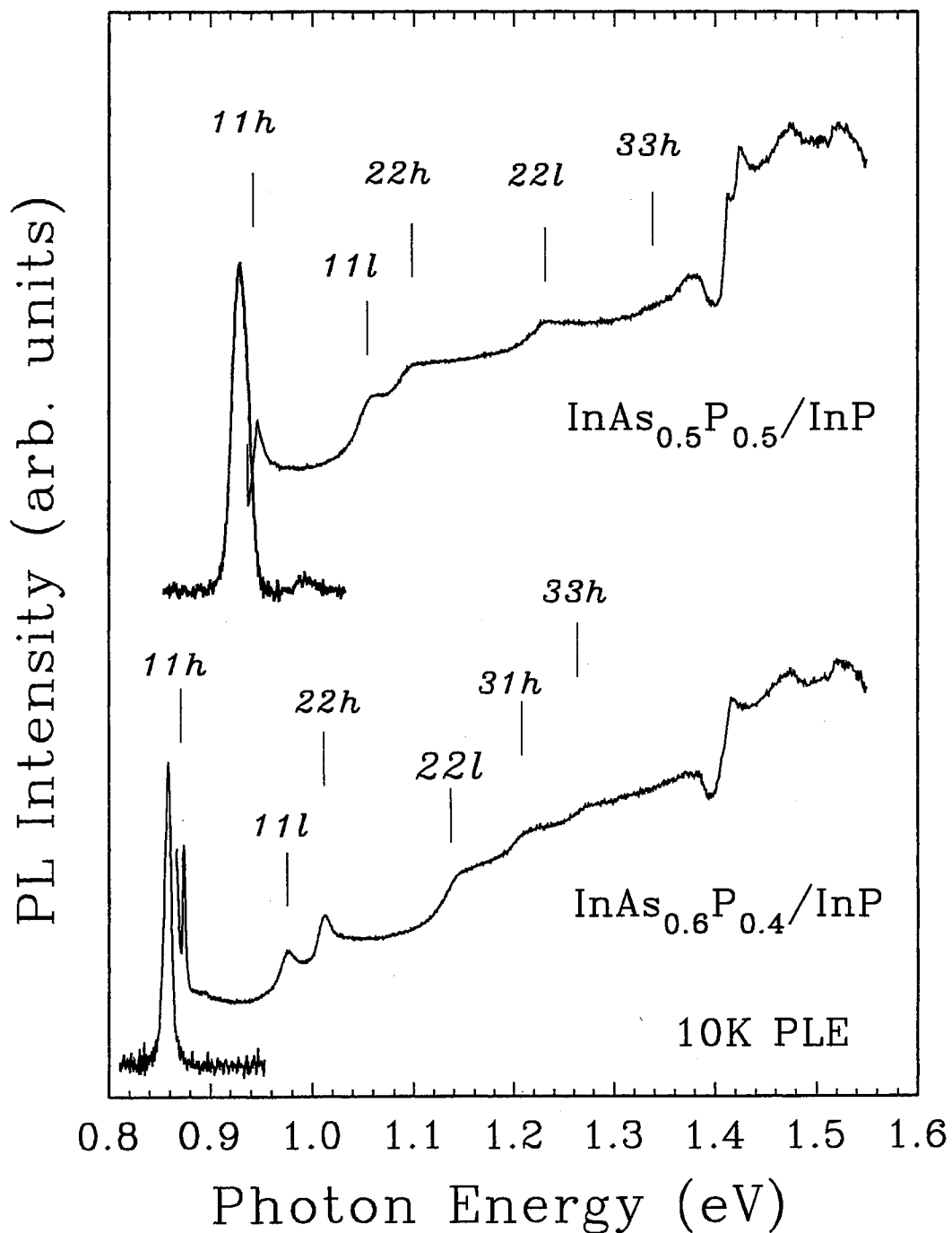


Figure 26. Photoluminescence and excitation spectra at 10K for the two $\text{InAs}_x\text{P}_{1-x}/\text{InP}$ SMQW samples. For the PLE measurement, the detector was set at the wavelength of PL transition for each sample. The labels refer to the identifications for spectral features and the vertical bars indicate calculated interband transitions. 11h(11l) is refer to the transition between $n=1$ electron and $n=1$ heavy-hole (light-hole) subbands.

well. PLE spectra show clearly other interband transitions related to the higher confined states which indicates the good quality of the samples. In order to identify the observed transitions, we have performed calculations based on the envelope function approximation and phenomenological deformation theory discussed in chapter II.

When $\text{InAs}_x\text{P}_{1-x}/\text{InP}$ QW's are grown commensurately on a (100) InP substrate, only the $\text{InAs}_x\text{P}_{1-x}$ well layers will be tetragonally distorted due to the larger equilibrium lattice constant compared to that of InP, resulting in built-in biaxial compressive strain in the $\text{InAs}_x\text{P}_{1-x}$ layers. Using Eq. (6), the built-in biaxial compressive strains in the $\text{InAs}_x\text{P}_{1-x}$ layers were calculated to be about 1.94% and 1.62% of the lattice mismatch for $\text{InAs}_{0.6}\text{P}_{0.4}/\text{InP}$ and $\text{InAs}_{0.5}\text{P}_{0.5}/\text{InP}$ SMQW samples, respectively. Fig. 27 shows the schematic representation of the effect of the biaxial compressive strain on the band edges of the $\text{InAs}_x\text{P}_{1-x}$ alloy. The parameters for the $\text{InAs}_x\text{P}_{1-x}$ alloys were evaluated by linear interpolation between values of InAs and InP [75]. The band gap for unstrained $\text{InAs}_x\text{P}_{1-x}$ alloy layers depends on the As composition as follows [75]:

$$\begin{cases} E_g^0(x) = 1.417 - 1.36x + 0.36x^2 & (10\text{K}), \\ E_g^0(x) = 1.351 - 1.315x + 0.32x^2 & (300\text{K}) \end{cases} \quad (81)$$

Furthermore, it induces the coupling of the light-hole band ($\frac{3}{2}, \pm\frac{1}{2}$) and the spin-orbit split-off band ($\frac{1}{2}, \pm\frac{1}{2}$), which results in a nonlinear correction to the light-hole valence band by moving the edge towards the heavy-hole band as seen in Fig. 27. The effective mass of the light-hole band edge should also be modified accordingly as a result of the mixing between the light-hole band and the split-off band [98,99]:

$$\Delta \left(\frac{1}{m_{lh}^*} \right) = \frac{1}{2} \left(\frac{1}{m_{lh}^*} - \frac{1}{m_{hh}^*} \right) \times \left(\frac{1 + 9\delta E_S/\Delta_0}{(1 + 2\delta E_S/\Delta_0 + (\delta E_S/\Delta_0)^2)^{1/2}} \right). \quad (82)$$

The calculation results were compared with the PLE spectra as shown in Fig. 26. The first number in the notation shown in the figure refers to the confined electron levels, the second number refers to the confined hole levels, and $h(l)$ denotes the transition involving a heavy- (light-) hole subband. For example, $11h$ means the

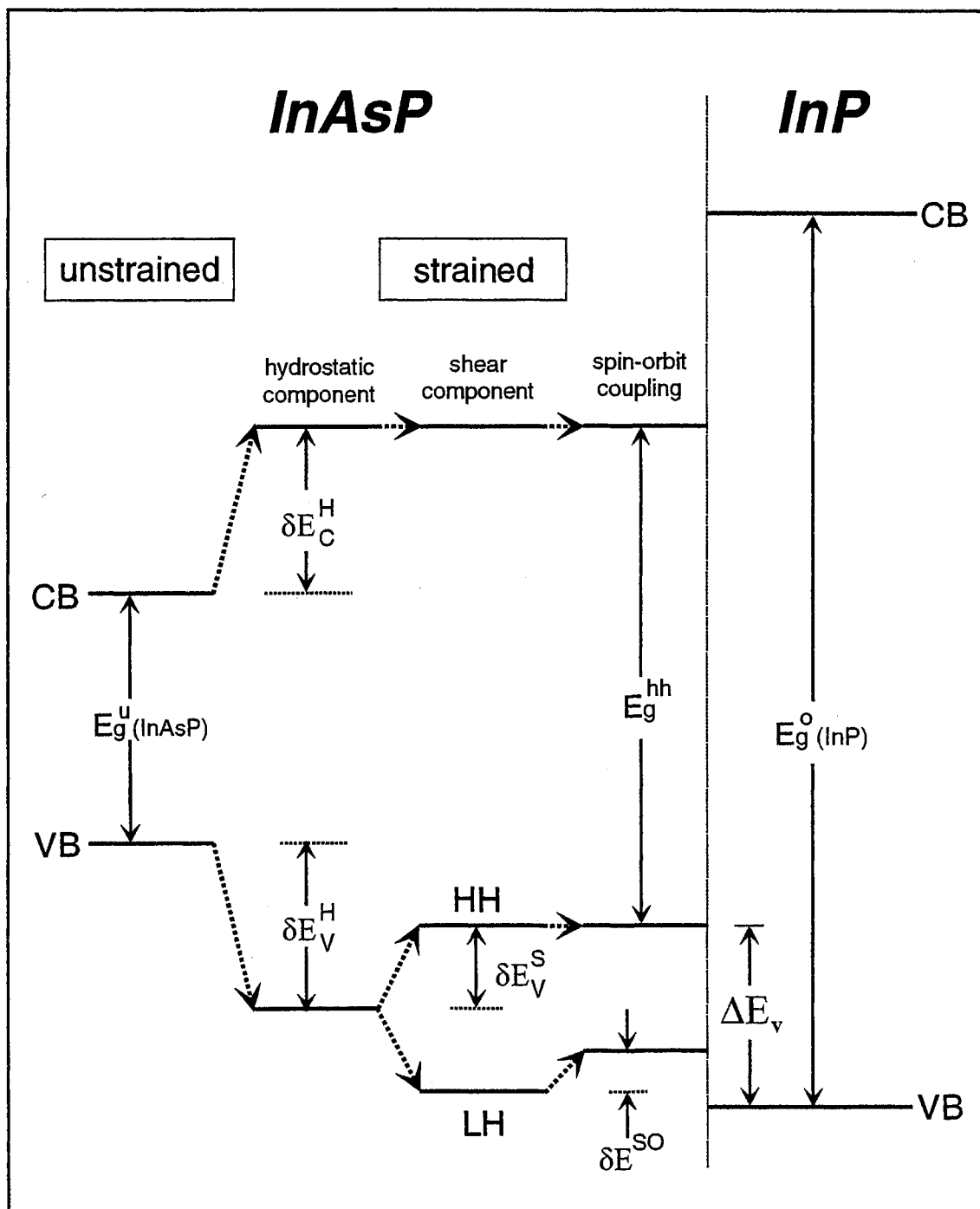


Figure 27. Schematic representation of effects of the biaxial compressive strain on the $\text{InAs}_x\text{P}_{1-x}$ layers. The coupling between light-hole band and spin-orbit split-off band moves the light-hole band edge towards the heavy-hole band. This effect was noticeable in the calculation results for the interband transition energies related to the higher order confined light-hole states ($n \geq 2$).

transition between $n=1$ electron and $n=1$ heavy-hole subbands. The transition near 1.39 eV corresponds to the onset of absorption by acceptor impurities in the InP layers, and the peak at 1.42 eV is the InP band edge absorption.

It is important to take into account the effects of band nonparabolicity and strain induced valence band mixing on the carrier effective masses in calculating the energy levels of the confined states, especially for higher order ($n \geq 2$) confined energy levels. The variations in the carrier effective masses induced by those effects substantially influence the higher quantum number transition energies for the light-hole subbands. For instance, only one light-hole subband was found to be confined instead of two if the correction for the light-hole effective mass was included in the calculation. In the calculation for the interband transition, the valence band offset was used as the major fitting parameter. The best fitting results were obtained with the unstrained valence band offset ratio as $Q_v = \Delta E_v / \Delta E_g \sim 0.3$.

Shown in Fig. 28 is a comparison of a PLE spectrum and a PT spectrum for the $\text{InAs}_{0.6}\text{P}_{0.4}/\text{InP}$ SMQW sample. The room temperature PT spectrum was taken at a hydrostatic pressure of 6.5 kbar. This applied pressure increases the band gap by about 60 meV in energy in a way analogous to the change in band gap with temperature. In general, the spectral features are seen to coincide with each other except for the structure (indicated by Δ) located around 1.072 eV in the PT spectrum. Note that $11l$ and $22h$ transitions could not be separately resolved from the PT spectrum due to thermal broadening. The structure marked by Δ was not observed in the PLE measurements and could not be assigned to the transitions involving the confined heavy-hole or light-hole bands in the $\text{InAs}_x\text{P}_{1-x}$ layers by our calculations. This structure is most likely related to the transition between the top of the spin-orbit split-off valence band and the lowest confined electron state. Though the values of split-off Δ_0 for InAs (0.381 eV) and for InP (0.110 eV) are well known and the difference is fairly large, the bowing effect for the Δ_0 band for $\text{InAs}_x\text{P}_{1-x}$ alloy system is not clear at present. By fitting our experimental data, Δ_0 was estimated to be about 0.20 eV for unstrained $\text{InAs}_{0.6}\text{P}_{0.4}$. Also the

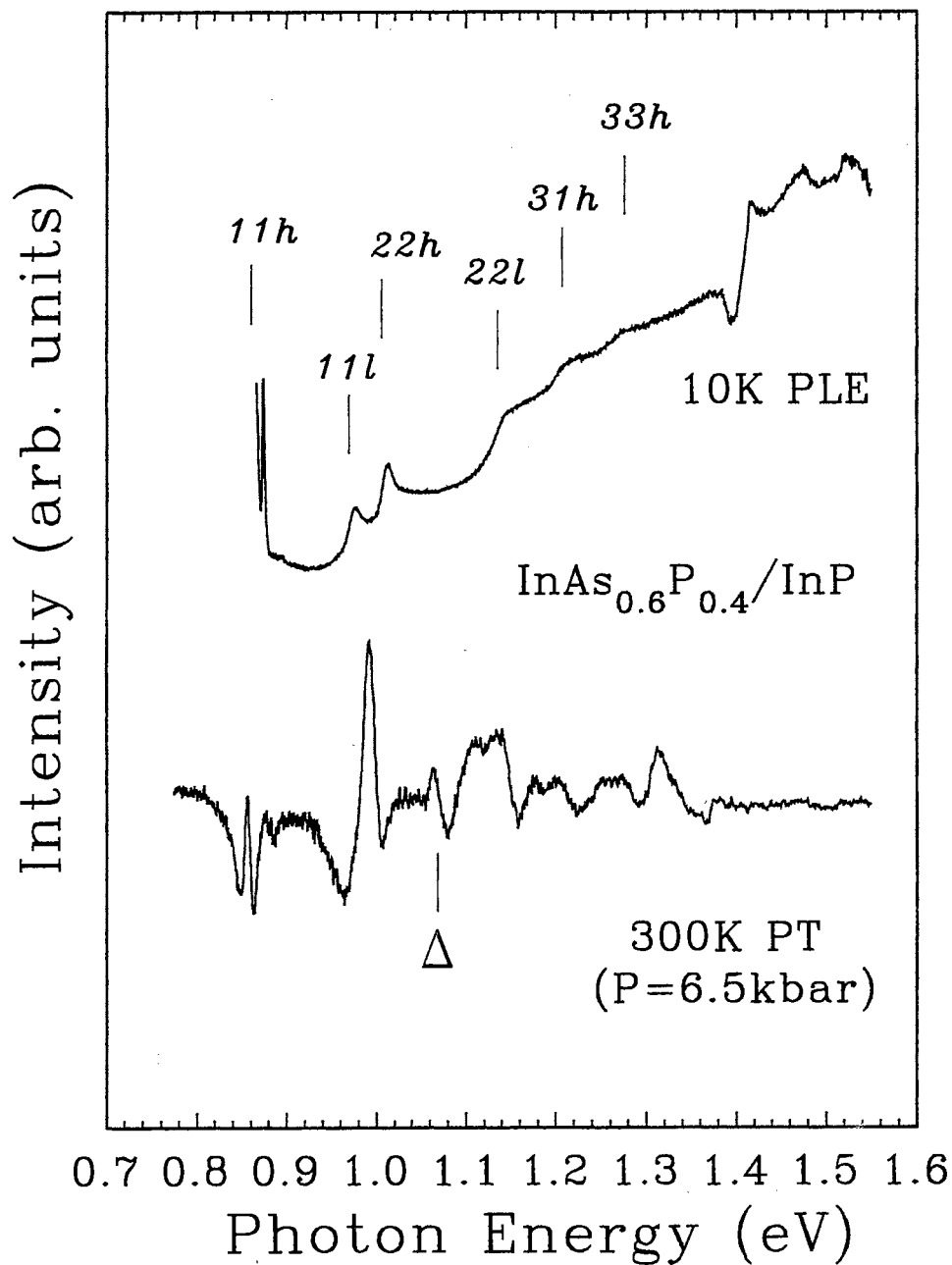


Figure 28. Comparison of PLE spectrum at 10K and PT spectrum at room temperature for the $\text{InAs}_{0.6}\text{P}_{0.4}/\text{InP}$ SMQW. The PT spectrum was taken at the hydrostatic pressure of 6.5 kbar. The structure indicated by Δ in the PT spectrum is attributed to the transition from first confined spin-orbit split-off subband to electron subband.

first confined spin-orbit split-off state was found to remain near the same energy position as the ($J = \frac{3}{2}$) valence band edge of InP barriers.

Generally, in PLE, as the excitation source is tuned and the photoluminescence is measured at a given energy wavelength, peaks appear in the spectrum as a result of an increase in the absorption coefficient. Contributions to PLE peaks depend on the efficiency of relaxation and/or coupling to the luminescence level under observation. In this work, the observation level was set close to the $11\hbar$ transition. It can be seen from Eq. (23) that there is no coupling between the heavy-hole band and the spin-orbit split-off band. A large number of photoexcited holes could then resonantly tunnel into the barriers rather than relax down to the lowest confined heavy-hole level in the wells. Therefore, the optical transition from confined spin-orbit split-off band to confined electron levels could not be observed from the overall PLE measurement. In contrast, the PT measurements probe directly the photoexcitation of different levels and derivative-like spectral features appear in the spectrum as a result of the external perturbation on the two-dimensional carrier density of states. The high sensitivity of modulation spectroscopy ensures observation of the transition from confined spin-orbit split-off subband to the confined electron states in the conduction band.

As seen in Fig. 26, the linewidths of PL and PLE spectra of the $\text{InAs}_{0.5}\text{P}_{0.5}/\text{InP}$ SMQW sample are broader than those of the $\text{InAs}_{0.6}\text{P}_{0.4}/\text{InP}$ SMQW. For example, the FWHM of the PL peak of the $\text{InAs}_{0.5}\text{P}_{0.5}/\text{InP}$ SMQW (9.5 meV) is about twice as large as the peak of the $\text{InAs}_{0.6}\text{P}_{0.4}/\text{InP}$ SMQW (5 meV). Since linewidth broadening usually reflects the quality of the sample, the quality of the short-period strained superlattice layers tends to decrease due to the inhomogeneities and layer thickness fluctuations. The linewidth broadening in PL and PLE spectra also indicate that compositional inhomogeneities are present in the well materials. Marzin *et al.* have reported similar results of their PL and PLE measurements on the $\text{InGaAlAs}/\text{InGaAs}$ MQW system using $(\text{InAs})_2\text{ML}(\text{GaAs})_2\text{ML}$ short-period strained

superlattices as well materials [100]. In addition, the intralayer thickness fluctuations could lead to variations of confined energies resulting in broadening of PL and PLE spectra as well.

Conclusions

Low-temperature PL and PLE measurements, and room temperature PT measurement under hydrostatic pressure were performed to study the excitonic interband transitions in $\text{InAs}_x\text{P}_{1-x}/\text{InP}$ SMQW samples. To identify the interband transitions in the experimental spectra, the theoretical calculations were performed using the envelope function approximation and phenomenological deformation potential theory by taking into account the band nonparabolicity and the strain-induced valence band mixing between light-hole and split-off bands. From the best fit of the PLE data to the interband transitions, the valence band offset ratio $Q_v (= \Delta E_v / \Delta E_g)$ was obtained as ~ 0.3 . Our result indicate that it is important to consider the effects of strain induced mixing between the light-hole and spin-orbit split-off bands both on the valence band edges and on the light-hole effective mass in order to identify the higher order light-hole transitions ($n \geq 2$) in PLE spectra. In addition to well resolved spectral features associated with the transitions from confined heavy-hole and light-hole energy levels, the spectral structure attributed to the transition between the spin-orbit split-off band and the lowest confined electron state was observed. The observed linewidth broadening of PL and PLE spectra from the MQW sample with the InAs/InP short-period superlattice is found to result from compositional inhomogeneities and intralayer thickness fluctuations of well materials.

CHAPTER VI

HIGHLY STRAINED CdSe/ZnSe QUANTUM WELLS

Introduction

Wide band gap II-VI semiconductor heterostructures have attracted much attention in recent years for their scientific and technological importance in blue-green optoelectronic devices, such as semiconductor laser diodes and light-emitting diodes. The ZnSe-based QW structures are among the most extensively studied heterostructures [101]. In the past few years, great progress has been made with the demonstration of blue laser action and electroluminescence from ZnSe based QW devices [102–106]. Recently, all-binary II-VI compound heterostructure systems such as ZnSe/ZnS, CdTe/ZnTe, and CdSe/ZnSe have attracted much attention due to their many device applications and large optical nonlinearity [107]. Among them, the CdSe/ZnSe system is of particular interest because it is grown utilizing two constituent materials with different bulk crystal structures [12,108–114]. Although the normal crystal structure of CdSe is hexagonal wurtzite, single crystal zinc blende CdSe and CdZnSe alloy thin films have been successfully grown on (100) GaAs substrates using MBE [110–112,114–116] and MOCVD [108] growth techniques.

In this chapter, we present the results of a study on the optical properties of CdSe/ZnSe QW's grown by MBE on GaAs substrates. A variety of CdSe/ZnSe single quantum well (SQW) and MQW structures with different well widths were grown. PL, PLE, and PR measurements were performed at low temperatures to characterize quantum confinement effects in these samples and to evaluate sample quality by monitoring the excitonic emissions from the QW's. Hydrostatic

TABLE IV.

Sample structures of CdSe/ZnSe QW's.

Samples	# of samples	Structures
SQW's	4	ZnSe/(CdSe) _n /ZnSe, $n = 1, 2, 3, 4$ ML
MQW's	2	1 ML MQW: [CdSe(3 Å)/ZnSe(163 Å)] x 50 periods 2 ML MQW: [CdSe(7 Å)/ZnSe(167 Å)] x 25 periods
fractional SQW	1	a sample with a series of submonolayer CdSe wells ZnSe/(CdSe) _n /ZnSe, $n = 1/4, 1/2, 3/4, 1$ ML

pressure-dependent PL measurements were also performed at low-temperature on 1-4 ML SQW samples at pressures up to 50 kbar.

Experimental details and results

Sample preparations

All CdSe/ZnSe QW samples used in this study were grown by MBE using GaAs substrates. A 2 μm thick ZnSe buffer layer was grown on a (100) GaAs substrate under optimal growth conditions [12,117]. Then, a ~ 1000 Å ZnSe cladding layer was deposited as the cap layer after the QW structures were grown. Three groups of QW structures are summarized in Table IV.

Fig. 29 schematically illustrate the CdSe/ZnSe QW structures. For the four SQW samples, a CdSe layer with 1 to 4 ML was grown for the QW region. For MQW samples, 50-periods of 1 ML QW's and 25-periods of 2 ML QW's were grown for the QW region. Total thickness of the MQW sample was kept to be the same in both samples by changing number of MQW periods. As illustrated in Fig. 30, the fractional CdSe/ZnSe SQW sample was grown by alternating the

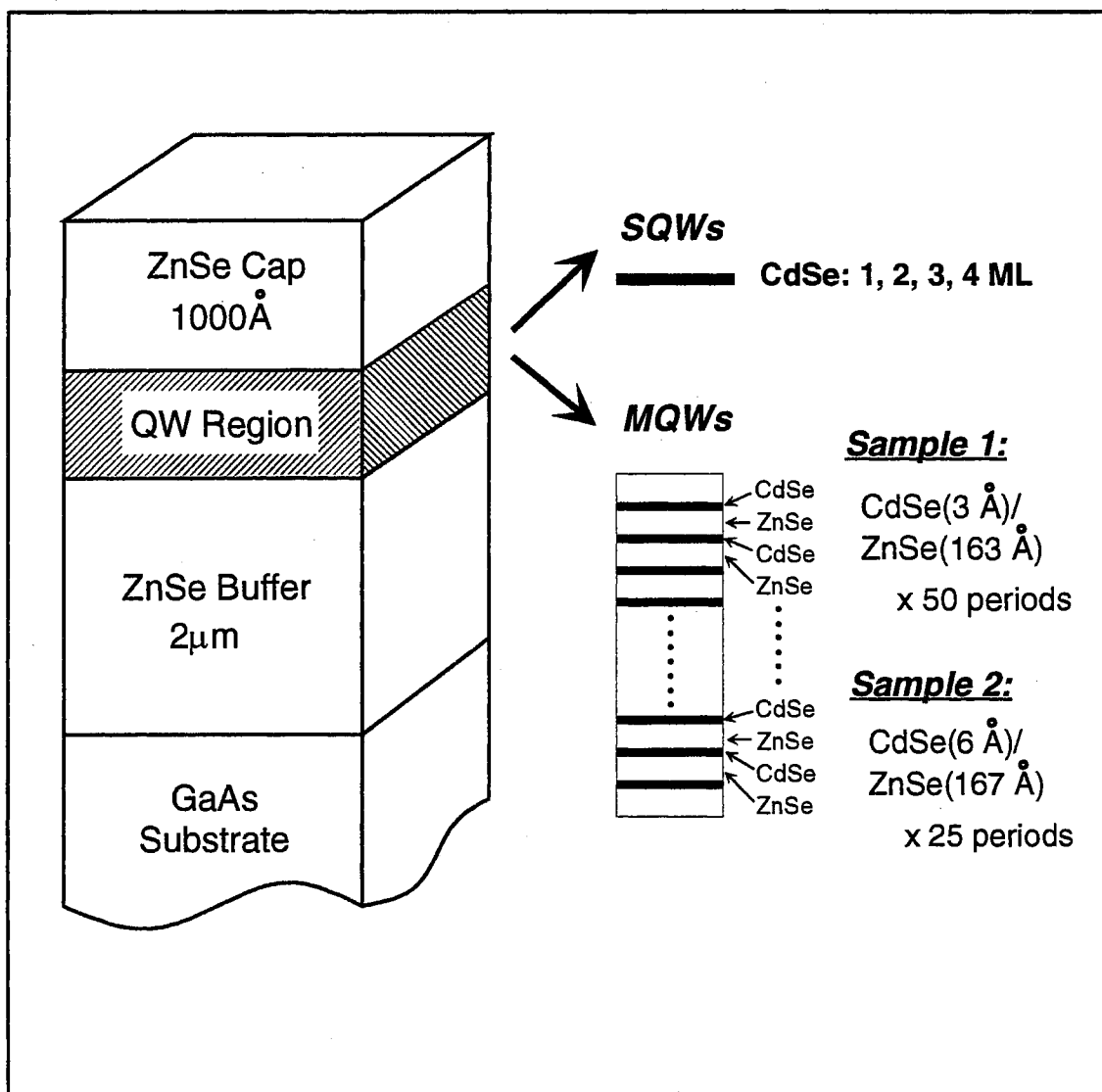


Figure 29. Schematic illustration of the CdSe/ZnSe QW structure. For SQW samples, a CdSe layer with 1 to 4 ML was grown for the QW region. For MQW samples, 50-periods of 1 ML QWs and 25-periods 2 ML QWs were grown in the QW region to keep the total thickness of the MQW samples the same for both samples.

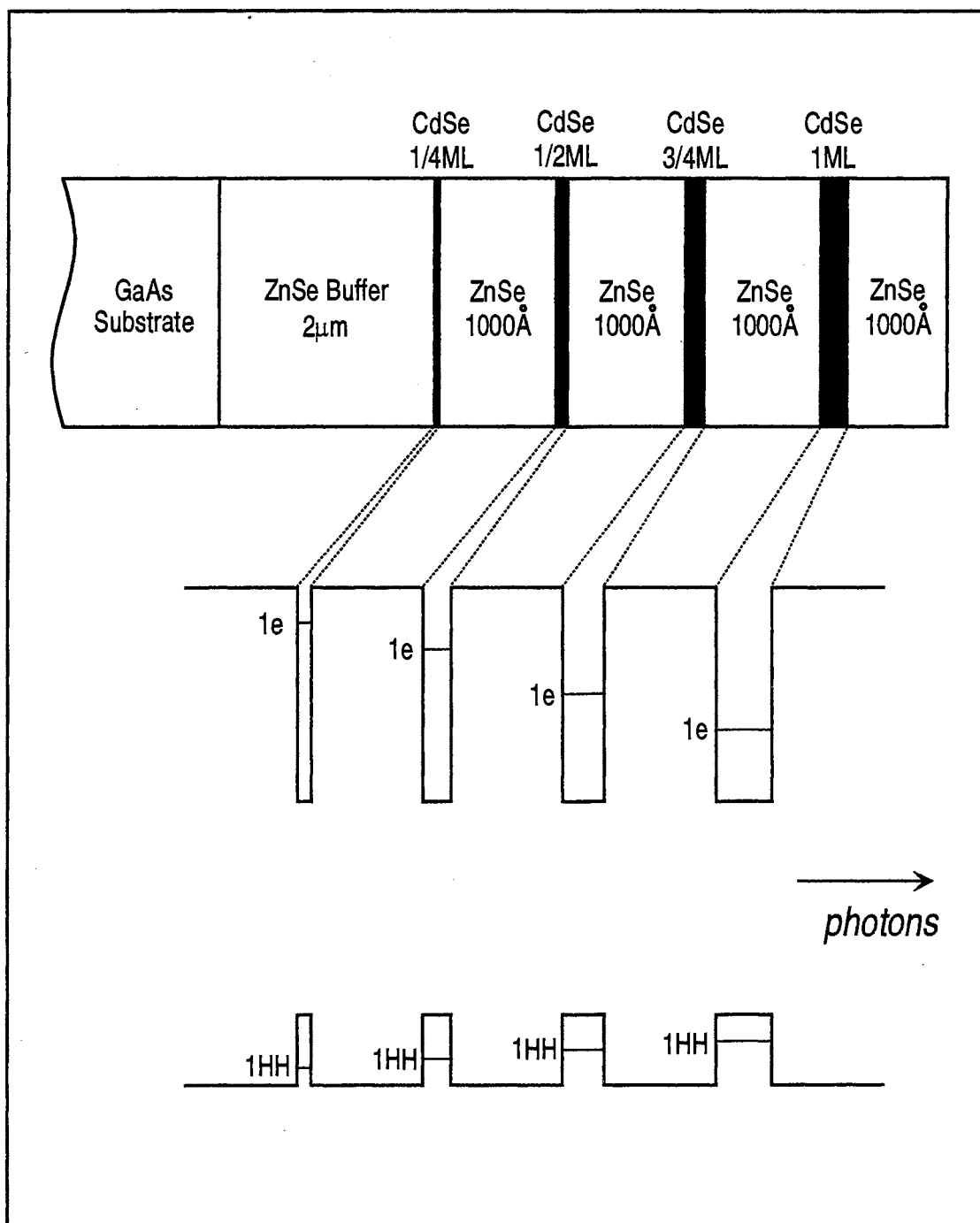


Figure 30. Schematic illustration of the CdSe/ZnSe submonolayer SQW structure. The whole sample structure is shown on top and its corresponding QW band diagram is shown at the bottom. $1e$ and $1hh$ denote the quantum confinement levels for the electron and heavy-hole bands. The confinement energies are different in the four wells due to the different well widths.

CdSe layers of less than one monolayer and ZnSe of 1000 Å. At the top, the whole sample structure is shown, and at the bottom, its QW band diagram is shown. The quantum confinement energies are different due to the different well widths. $1e$ and $1hh$ denote the quantum confinement levels for the electron and heavy-hole bands. The thickness of the CdSe layers was controlled by the shutter time of the MBE machine. The deposition times for the CdSe well layers onto ZnSe surfaces were 1, 2, 3, and 4 seconds of the MBE shutter times for opening the Cd source, which correspond to roughly 1/4, 1/2, 3/4, and 1 ML thicknesses of the CdSe layers, respectively [12,117]. The barrier and well thicknesses of the CdSe/ZnSe MQW samples were measured by x-ray diffraction measurements and the results showed that the samples had a fine multilayer structure [118].

Experimental technique

Low temperature PL, PLE and PR measurements were performed to characterize quantum confinement effects in these samples. For all four SQW samples, hydrostatic pressures up to 50 kbar were applied to study the effects of hydrostatic pressure on the direct interband transitions by the low temperature PL measurements.

For the PL measurements, a HeCd laser at 3250 Å was used as the excitation source. The PL signals were sent through a 0.85 *m* double-grating monochromator (SPEX 1403) and were detected by a GaAs PMT (Hamamatsu, R943-02) in conjunction with a photon counting and data acquisition system .

For the PLE measurement, continuous light from a 250 W tungsten halogen lamp dispersed by a 0.25 *m* monochromator (SPEX 1681) was used as a tunable excitation source. The detection spectrometer was set at the wavelength corresponding to the PL peak position for each sample. The PLE signals were detected in a way similar to that of the PL measurement using a 0.5 *m* monochromator (Chromex 500IS/SM).

For the PR measurements, the 3250 Å He-Cd laser beam chopped with a frequency of 200 Hz was used to provide a repetitive modulation to the samples

and continuous light from a 250 W tungsten halogen lamp dispersed by the 0.5 m monochromator was used as the probe beam. The collected luminescence and reflectance signals were detected by a UV enhanced Si photodiode followed by a lock-in amplifier and data acquisition system.

Experimental results

The PL spectra exhibit a single excitonic emission line for all the samples used in this study except the sample with four submonolayer SQW's. Fig. 31 shows the PL spectra from 1, 2, 3, and 4 ML CdSe/ZnSe SQW samples at 10 K and atmospheric pressure. The PL signals from all samples exhibit a single emission peak with the characteristic of a typical lowest confined Γ - Γ excitonic transition. Since the heavy-hole band edge is higher than the light-hole band edge in this CdSe/ZnSe QW system due to the compressive strain in CdSe well layers, this transition is associated with the lowest confined electron and heavy-hole states, Γ_{1e} - Γ_{1hh} . The full width at half maximum (FWHM) of the Γ_{1e} - Γ_{1hh} emission is about 15 meV for the 1 ML SQW sample and about 35-40 meV for the other three. Under the same excitation conditions, the PL intensity of the 4 ML SQW sample decreases by a factor of 10 compared to the other three SQW samples with narrower wells.

In Fig. 32, the PL spectrum taken from the 'fractional' SQW sample with nominal submonolayer QW's is shown. Although the emission lines from the four wells in the sample overlap, the PL spectral structures associated with 1/4 and 1 ML wells can be well resolved. The FWHM is about 5 meV for the emission line corresponding to the nominal 1/4 ML well in the sample. The relative difference in intensities from different wells in this sample is due to the structure of the sample. Since the sample was grown with wide wells on the top of narrow wells as shown in Fig. 30, the 325 nm excitation source is absorbed by the wider wells near the surface and by the ZnSe barriers resulting in a decrease in excitation intensity for the narrower wells which are deeper in the sample. The PL intensity

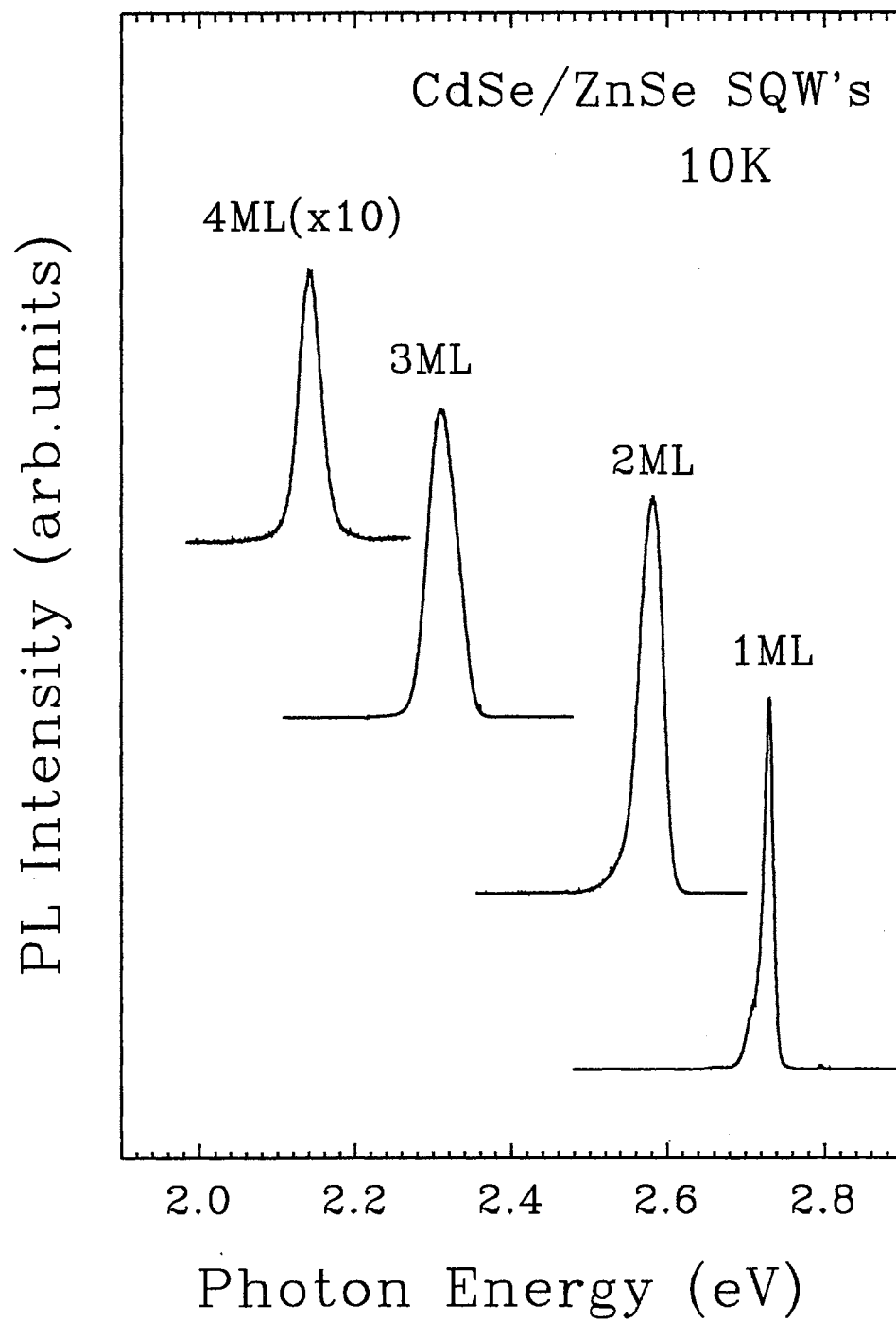


Figure 31. Photoluminescence spectra taken from CdSe/ZnSe SQW's with different well widths. The curves are vertically displaced for clarity.

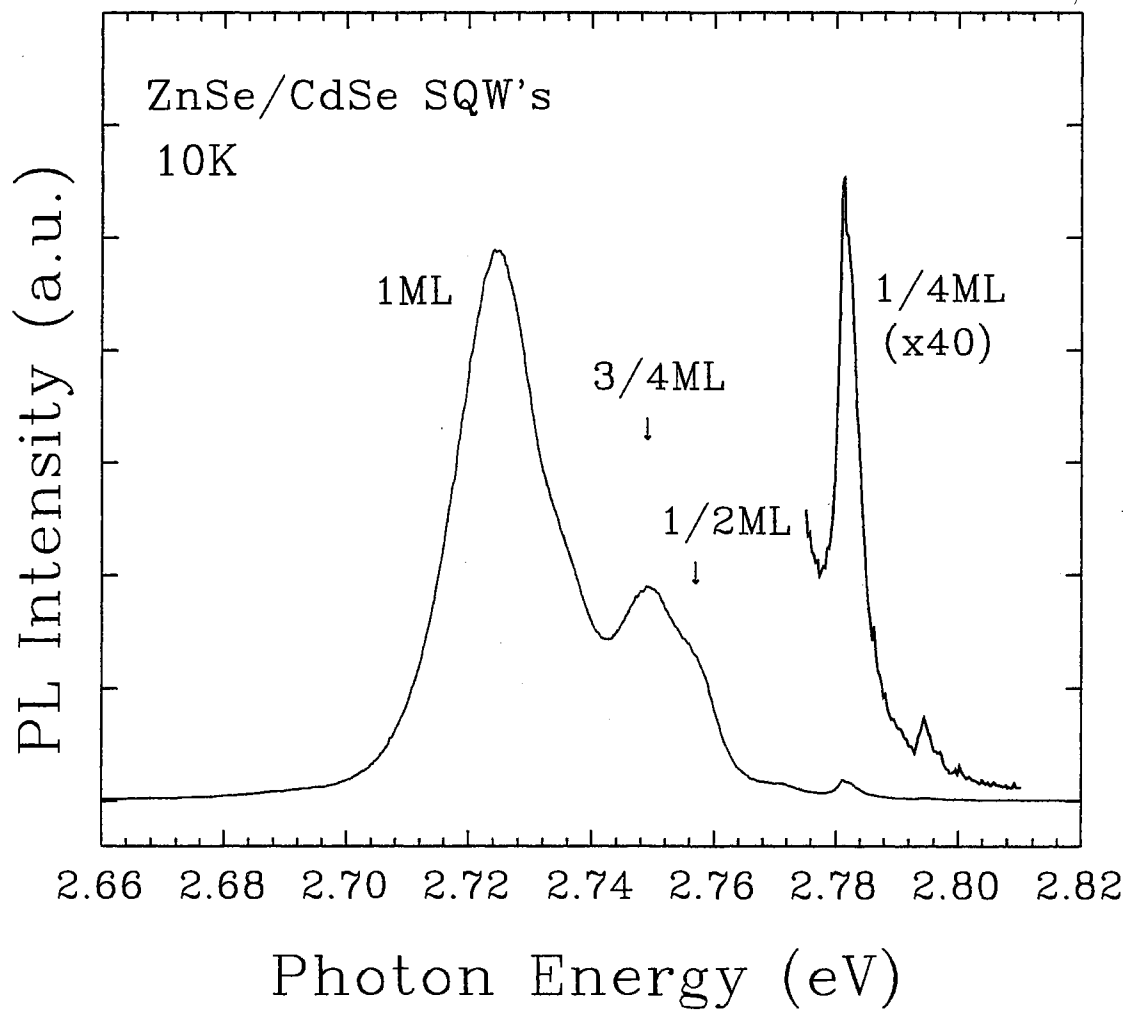


Figure 32. Photoluminescence spectrum of the CdSe/ZnSe SQW sample with nominal submonolayer CdSe wells. The major reason of the weak intensity for narrower well is that signal from narrower wells will be reabsorbed by wider wells (see the band diagram in Fig. 30).

from the narrower wells could be further reduced due to the reabsorption of their luminescence by the wider wells.

Fig. 33 shows the comparison of PL and PR spectra at 80 K obtained from the CdSe(3 Å)/ZnSe(163 Å) MQW's. Both PR and PL spectra show the lowest confined transition, $\Gamma_{1e}-\Gamma_{1hh}$. The other spectral structure at around 2.8 eV is the transition associated with the ZnSe barriers and the buffer layer. In the PR spectrum, the other transition around 2.65 meV is related to the light-hole in the ZnSe barrier. This will be shown from the calculation result for the confinement energies in this system. The FWHM of the $\Gamma_{1e}-\Gamma_{1hh}$ emission lines observed in the MQW samples are more than twice as broad as that from the SQW samples with the same well widths, mainly due to the layer thickness fluctuations in the MQW's. In these two MQW's, the energy positions of the $\Gamma_{1e}-\Gamma_{1hh}$ emission line are significantly lower than their counterparts in the SQW's.

The experimentally observed energy positions of $\Gamma_{1e}-\Gamma_{1hh}$ transitions from the all samples studied in this work are plotted in Fig. 34 as a function of the well width (number of monolayers). As shown in the figure, the difference in energy positions between the $\Gamma_{1e}-\Gamma_{1hh}$ transitions from SQW's and MQW's with identical CdSe layer thickness is quite large. From this figure one can also see that the experimentally obtained PL spectral range (450-577 nm) from the CdSe/ZnSe QW's used covers virtually the entire blue-green region as the CdSe layer thickness varies from nominal 1/4 ML to 4 ML's. This suggests that the all-binary CdSe/ZnSe system is promising in the development of optoelectronic devices operating at the short wavelength range of the visible region.

Analysis and discussion

When a CdSe layer is coherently grown on a ZnSe buffer layer, the CdSe layer will experience a compressive biaxial strain on the plane perpendicular to the growth direction due to the larger lattice constant of bulk cubic CdSe compared to that of the bulk ZnSe. The lattice constants are 6.052 Å and 5.668 Å for bulk cubic CdSe and bulk ZnSe, respectively [75]. The calculated strain on the CdSe

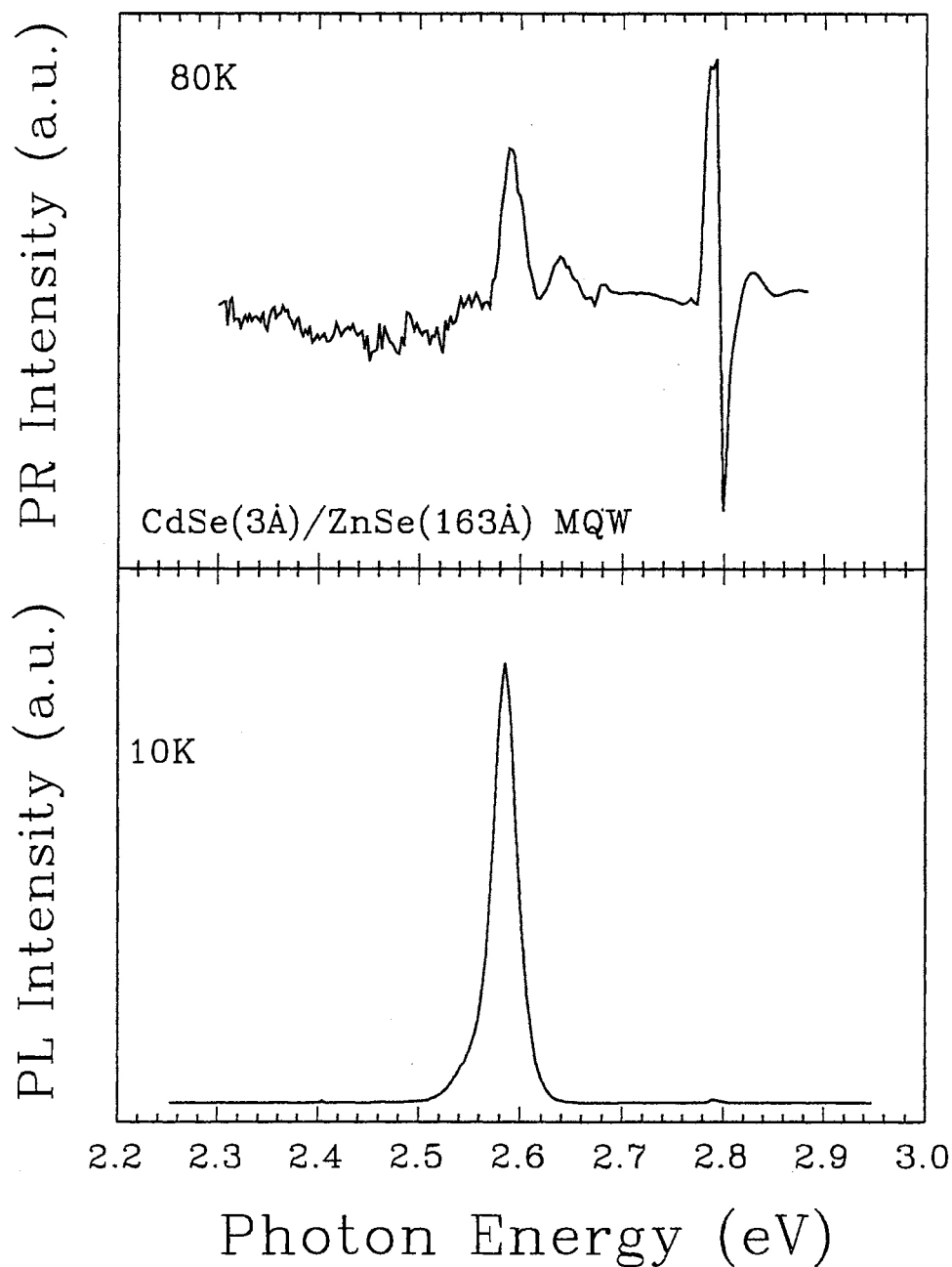


Figure 33. Photoreflectance (top) and photoluminescence (bottom) spectra from the CdSe(3 Å)/ZnSe(163 Å) MQW sample. Both PR and PL spectra show the lowest confined transition, $\Gamma_{1e}-\Gamma_{1hh}$. The other spectral structure at around 2.8 eV is the transition associated with the ZnSe barriers and the buffer layer. In PR, the transition around 2.65 meV is related to the light-hole. The FWHM of the lowest confined transition is about 30 meV which is twice as large as that of SQW.

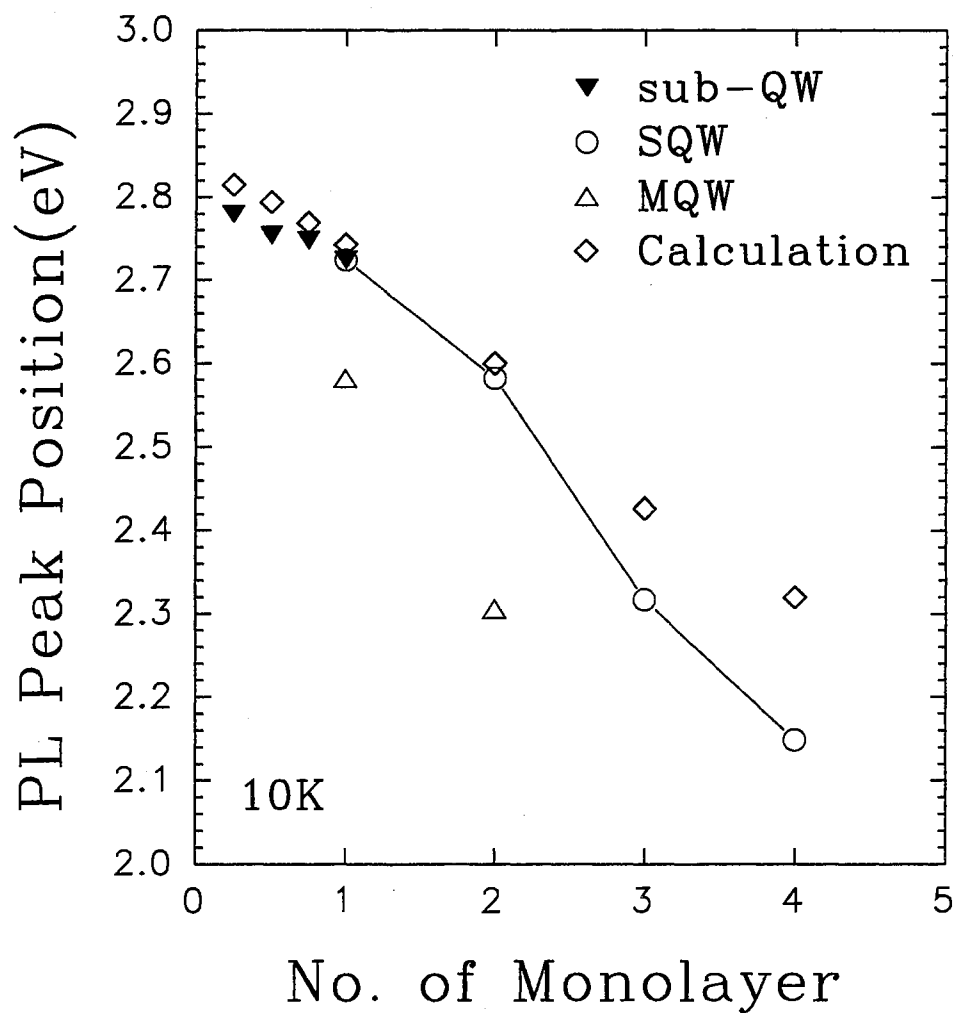


Figure 34. Experimentally obtained energy positions of $\Gamma_{1e}-\Gamma_{1hh}$ transitions of CdSe/ZnSe QWs as a function of CdSe well thickness in number of monolayers. Theoretical calculations using simple squared QW model for the lowest confined transition are compared. Detail explanations for the calculation will be given in the text.

using Eq. (6) in this CdSe/ZnSe system is about 6.78 %. Using the deformation potential theory, the effects of the compressive strain on the CdSe band structure at the Γ -points are shown in Fig. 35.

The transition energies between the lowest confined electron and heavy-hole states in SQW's were calculated by both a simple square potential well model and an envelope function approximation. In the calculation, the SQW's with a well width less than one monolayer were assumed to form a $\text{Cd}_x\text{Zn}_{1-x}\text{Se}$ alloy with an effective thickness of 2 ML as suggested by Zhu *et al.* [12]. Then, the alloy composition can be estimated depending on the nominal thickness of submonolayers. For example, 1/4 monolayer is equivalent to $x=0.125$ and one monolayer is equivalent to $x=0.5$. The numerical results are compared with experimental data in Fig. 34. After considering the exciton binding energy of ~ 20 meV [12], which was not included in the calculations, calculated results agree well with experiments for narrow QW's. However, a larger deviation exists between the calculation and the experiment for wider well samples. The reasons for this deviation might be that parameters for bulk CdSe are not well known and that our calculation might be somewhat simple for this structure. The confinement energy calculations showed only one confined electron level for all QW samples. The calculations also indicated that Type-II QW structure was formed for the light-hole band as shown in Fig. 35. Parameters used for the calculation of the strain effect and confinement energies in CdSe/ZnSe QW system are listed in Table V.

We observed a considerable decrease of PL intensity in the 4 ML SQW sample. The other SQW samples with narrower well widths (1, 2, and 3 ML) exhibit about the same emission intensity. It is well known that the decrease of PL intensity in a QW, particularly in a strained QW, usually indicates poor sample quality. Since CdSe/ZnSe is a highly lattice-mismatched strained system, the considerable decrease of the PL intensity in the 4 ML SQW sample (Fig. 31) is most likely due to the partial relaxation of the built-in strain. This occurs when the CdSe layer thickness exceeds the critical limit for the coherent growth of the strained layers. Misfit dislocations will be generated when this happens.

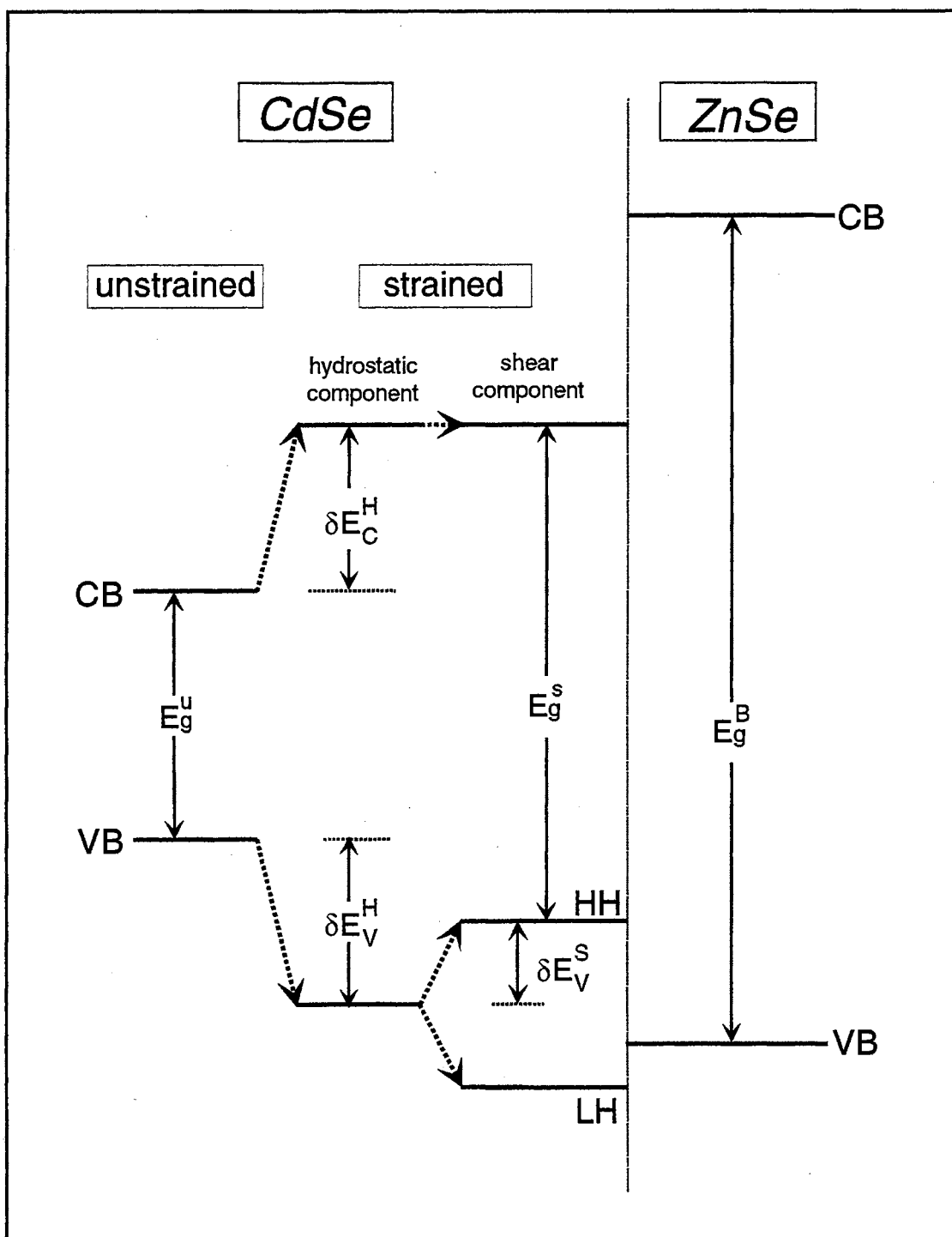


Figure 35. Schematic representation of the effects of compressive strain on the CdSe band edges. The confinement energy calculations show that a Type-II QW structure is formed for the light-hole while a Type-I QW structure is formed for the heavy-hole.

TABLE V.

Parameters used for the theoretical calculations for CdSe/ZnSe QWs. Lattice constant, a ; elastic stiffness constants, C_{ij} ; hydrostatic and shear deformation potential, a and b ; effective masses, m^* ; split-off bandgap energy, Δ .

Parameters	CdSe	ZnSe
a (Å)	6.052*	5.668*
E_g (eV)	1.765*	2.821*
$C_{11}(10^{11} \text{dyn/cm}^2)$	6.67*	8.26*
$C_{12}(10^{11} \text{dyn/cm}^2)$	4.63*	4.98*
a (eV)	-3.66†	-5.82†
b (eV)	-0.8†	-1.2†
m_e^* (emu)	0.13*	0.16*
m_{hh}^* (emu)	0.45*	0.6*
m_{lh}^* (emu)	0.12*	0.15*
Δ (eV)	0.416*	0.403*

* *Landolt-Borstein* [75]

† Pollak [23]

‡ People *et al.* [76]

Effects of hydrostatic pressure

Fig. 36 shows a typical low temperature PL spectra of the 2 ML CdSe/ZnSe SQW taken at different pressures. The strong excitonic emission associated with the $\Gamma_{1e}-\Gamma_{1hh}$ transition shifts towards higher energy as pressure increases. Other SQW samples showed similar behavior in the PL spectra under hydrostatic pressure. The effect of hydrostatic pressure on the $\Gamma_{1e}-\Gamma_{1hh}$ transitions in the 1-4 ML SQW's is shown in Fig. 37. The experimental data (symbols) were fit by the least-squares method (lines). The 1 and 2 ML SQW samples show a typically linear dependence of the $\Gamma_{1e}-\Gamma_{1hh}$ transition on pressure, while an appreciably smaller pressure dependence with considerably strong sublinear behavior was obtained for the 3 and 4 ML SQW samples. The experimental data were fit using equations:

$$\begin{cases} E(P) = E(0) + \alpha P, & \text{for 1 and 2 ML SQW's} \\ E(P) = E(0) + \alpha P + \beta P^2, & \text{for 3 and 4 ML SQW's,} \end{cases} \quad (83)$$

where $E(0)$ is the $\Gamma_{1e}-\Gamma_{1hh}$ transition energy at ambient pressure. The linear and quadratic pressure coefficients are denoted by α and β . In Table VI, the resulting pressure coefficients for these samples are listed along with values of ZnSe and wurtzite CdSe in bulk form. The $\Gamma_{1e}-\Gamma_{1hh}$ transition energies at ambient pressure are also given in the Table VI.

As clearly shown in Table VI, the pressure coefficients are dependent on the well width. The linear pressure coefficients of the $\Gamma_{1e}-\Gamma_{1hh}$ transitions decrease with increasing well width. Such a phenomenon can be attributed to a combination of several competing mechanisms [122,123,38,44,41,45,42]. Application of pressure on a QW induces a change of the barrier height of the QW due to the different pressure coefficients of the band gaps of the barrier and well materials. In CdSe/ZnSe QW's, the pressure coefficient of bulk ZnSe is greater than that of CdSe resulting an increase of the barrier height with increasing pressure. This increase of the barrier height with pressure results in increasing confinement energy and eventually increases the pressure coefficients. The pressure also decreases the lattice constant and consequently reduces the well width resulting in an increase in the confinement

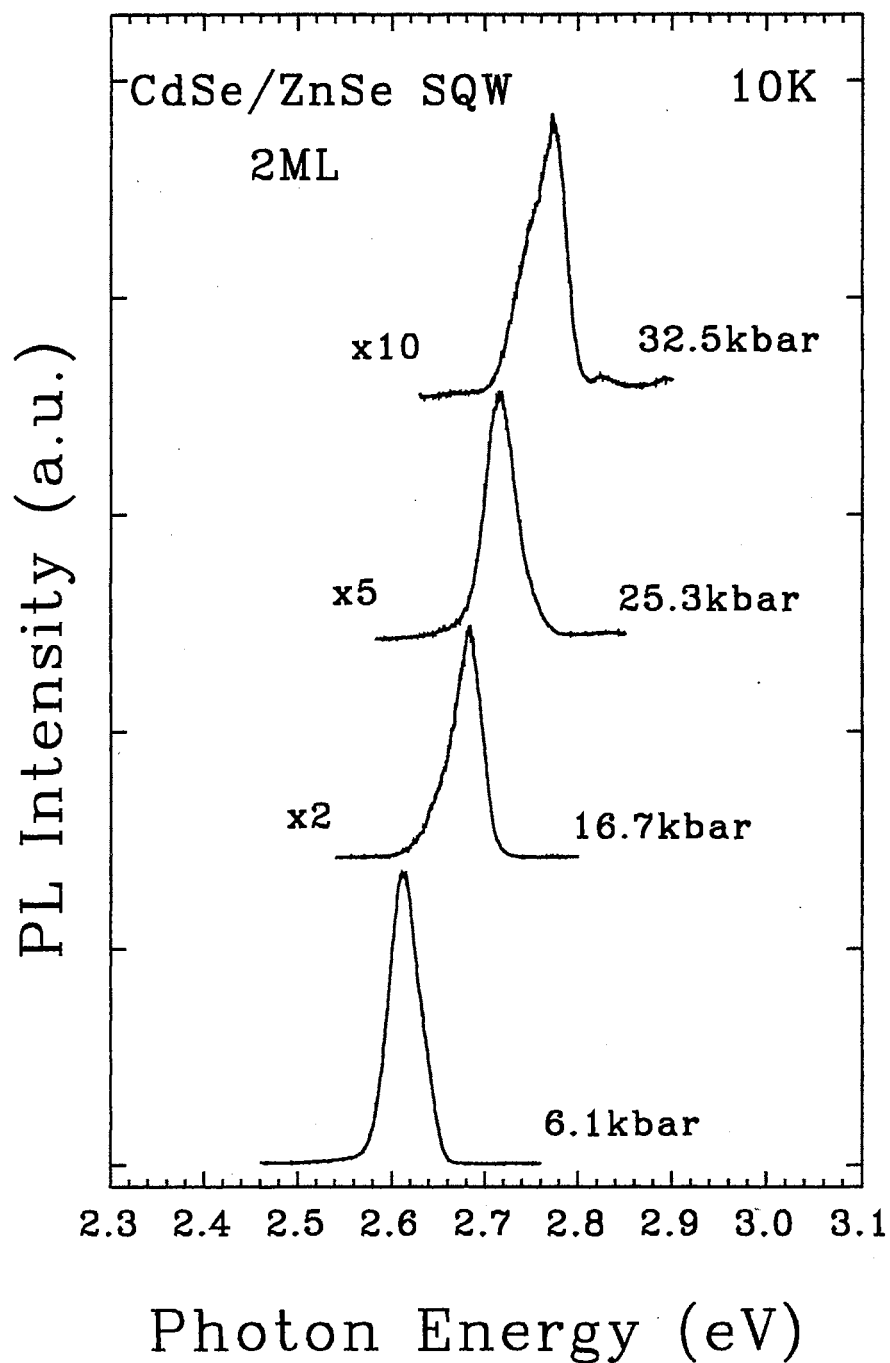


Figure 36. Typical 10 K PL spectra taken at different pressures from the 2 ML CdSe/ZnSe SQW. The strong excitonic emission associated with $\Gamma_{1e}-\Gamma_{1hh}$ transition shifts towards higher energy as pressure increases. The same phenomenon of pressure dependence of the PL spectra was observed in all other SQW samples.

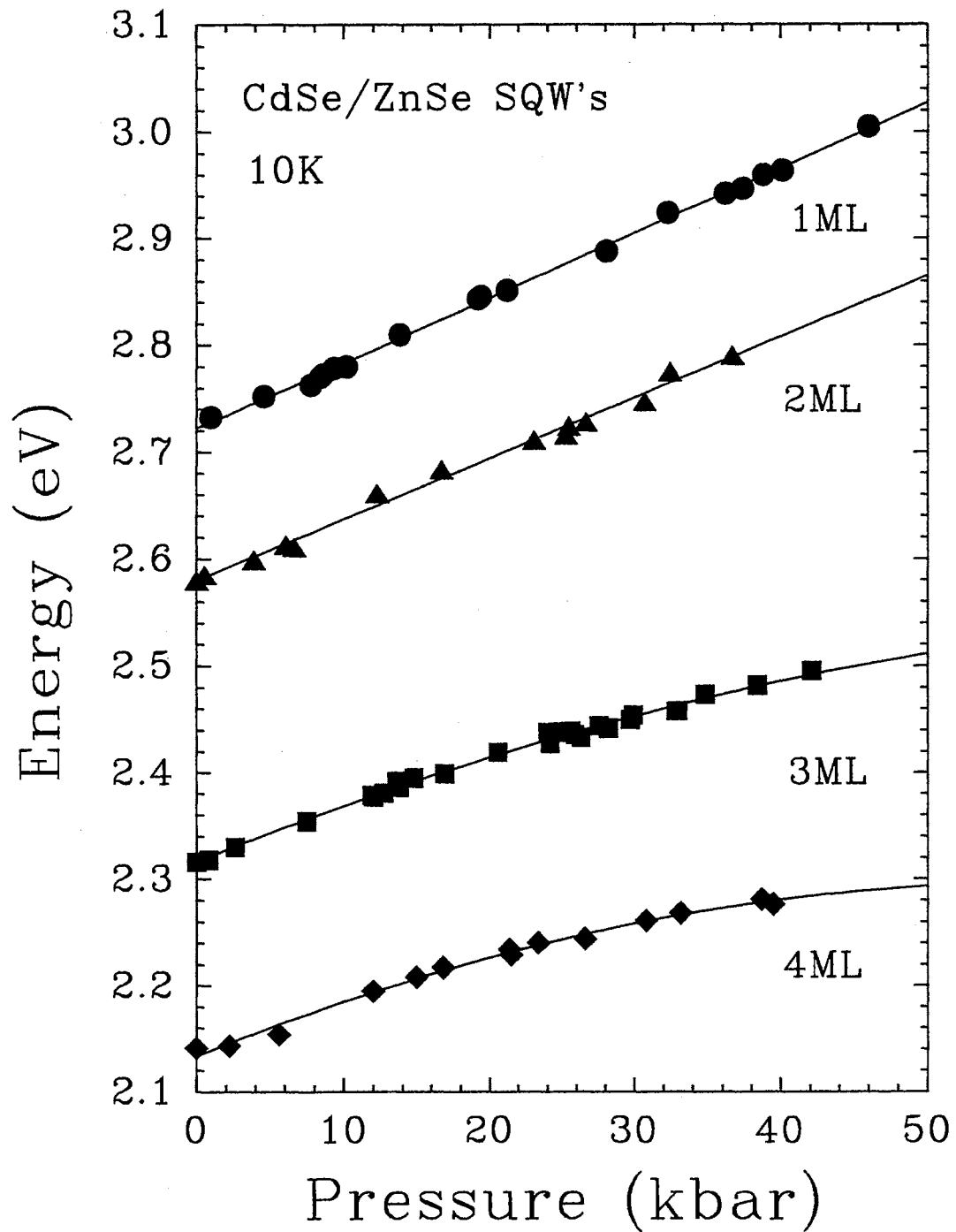


Figure 37. Pressure dependence of $\Gamma_{1e}-\Gamma_{1hh}$ transitions in monolayer SQW samples measured by PL at 10 K. The strong sublinear pressure dependent behavior of the 3 and 4 ML samples is considered to be caused by the strain relaxation under applied pressure.

TABLE VI.

Energy positions of the Γ_{1e} - Γ_{1hh} emissions and their pressure dependence obtained from CdSe/ZnSe SQW's. The Pressure coefficients of cubic and hexagonal CdSe bulks are also listed.

Samples	$E(0)(eV)$	$dE/dP(meV/kbar)$	$d^2E/dP^2(meV/kbar^2)$
1 ML	2.723	6.1	-
2 ML	2.580	5.7	-
3 ML	2.316	5.6	-3.3
4 ML	2.134	5.4	-4.3
ZnSe	2.812 *	6.6 †	-1.5 †
CdSe	1.738 ‡	5.8 ‡	-

*Shahzad *et al.* [119]

†Ves *et al.* [120]

‡Mei *et al.* [121]

energy in a QW. The pressure also increases the electron effective mass reducing the confinement energy and consequently affecting the exciton binding energy [123].

In a QW, the confinement energy increases as the well width decreases. This means that the confinement level is getting close to the band edge of the barrier. For the narrow well, therefore, the wave functions in the well will be more delocalized into the barrier. This delocalization makes the pressure coefficient follow that of the barrier material. For the CdSe/ZnSe system, the pressure coefficients of the lowest confined transitions are expected to be close to that of bulk ZnSe. Therefore, the pressure coefficient of the lowest confined transitions will increase with decreasing well width. As the well width increases, the pressure coefficient is expected to be close to that of bulk cubic CdSe. Despite the many factors for the reduction of the pressure coefficients with well width, the delocalization of the wave functions into the barrier is expected to be the major factor for the change in the pressure coefficient because our CdSe/ZnSe samples have very narrow wells (< 4 ML).

Strain relaxation in the 3 & 4 ML SQW's It is worthwhile to note the substantial sublinear pressure dependence of the Γ_{1e} - Γ_{1hh} transitions from the 3 and 4 ML SQW's. This pronounced sublinearity of the pressure dependence of the Γ_{1e} - Γ_{1hh} transitions observed from 3 and 4 ML SQW's can be attributed to the permanent relaxation of the built-in strain in these two samples as discussed below.

The elastically accommodated strained layer on a substrate can be relaxed if external pressure applied on the heterostructure induces misfit stress larger than the misfit-dislocation line tension. Even though the external pressure is hydrostatic, lattice relaxation can happen with a small applied pressure when the strength of the two forces are comparable. This phenomenon may happen in the 3 ML CdSe/ZnSe SQW sample. If the highly strained CdSe layer in the 3 ML SQW is at the margin of the critical thickness, the built-in strain in the CdSe on the ZnSe can start to relax with applied pressures. Dislocations then appear at the heterointerfaces as a result of pressure induced lattice relaxation. The short-range

potentials of the dislocations will perturb the wave functions of quantum states confined to the well and give rise to variations of the pressure dependence of those states. This gives a reduction of the pressure coefficient of the $\Gamma_{1e}-\Gamma_{1hh}$ transition and produces a significantly strong sublinear pressure dependence in the 3 and 4 ML SQW samples.

The evidence of the strain relaxation in the 4 ML SQW sample can be demonstrated by comparing PL and PLE spectra from all CdSe/ZnSe SQW samples taken at atmospheric pressure. As shown in Fig. 31, the reduction of PL emission intensity in the 4 ML sample may indicate its poor quality. Further demonstration of the strain relaxation in the 4 ML SQW can be achieved from PLE results in the energy region of the ZnSe band gap as shown in Fig. 38. For the 3 ML SQW sample, a huge increase of PL emission intensity occurs when the excitation photon energy is above the ZnSe band gap due to the significant change of the density of states, whereas such an increase is almost completely washed out for the 4 ML sample. The diffusion of photoexcited carriers created inside the ZnSe buffer layer towards the QW region is drastically decreased by numerous nonradiative defects such as dislocations induced by the strain relaxation. These nonradiative defects result in a significant reduction of the PL emission intensity and in the quenching of the PLE signal in the 4 ML sample. The PL and PLE spectra taken from the 3 ML sample at atmospheric pressure do not show significant differences from those of the samples with narrower well widths. This implies that 3 ML of CdSe layer in the CdSe/ZnSe SQW is still less than the critical thickness. Thus, strain relaxation is at least partially responsible for the substantial sublinear pressure dependence of interband transitions in the 3 and 4 ML CdSe/ZnSe SQW's. All our experimental results imply that the critical thickness of the CdSe layer in the CdSe/ZnSe QW's is less than 4 ML.

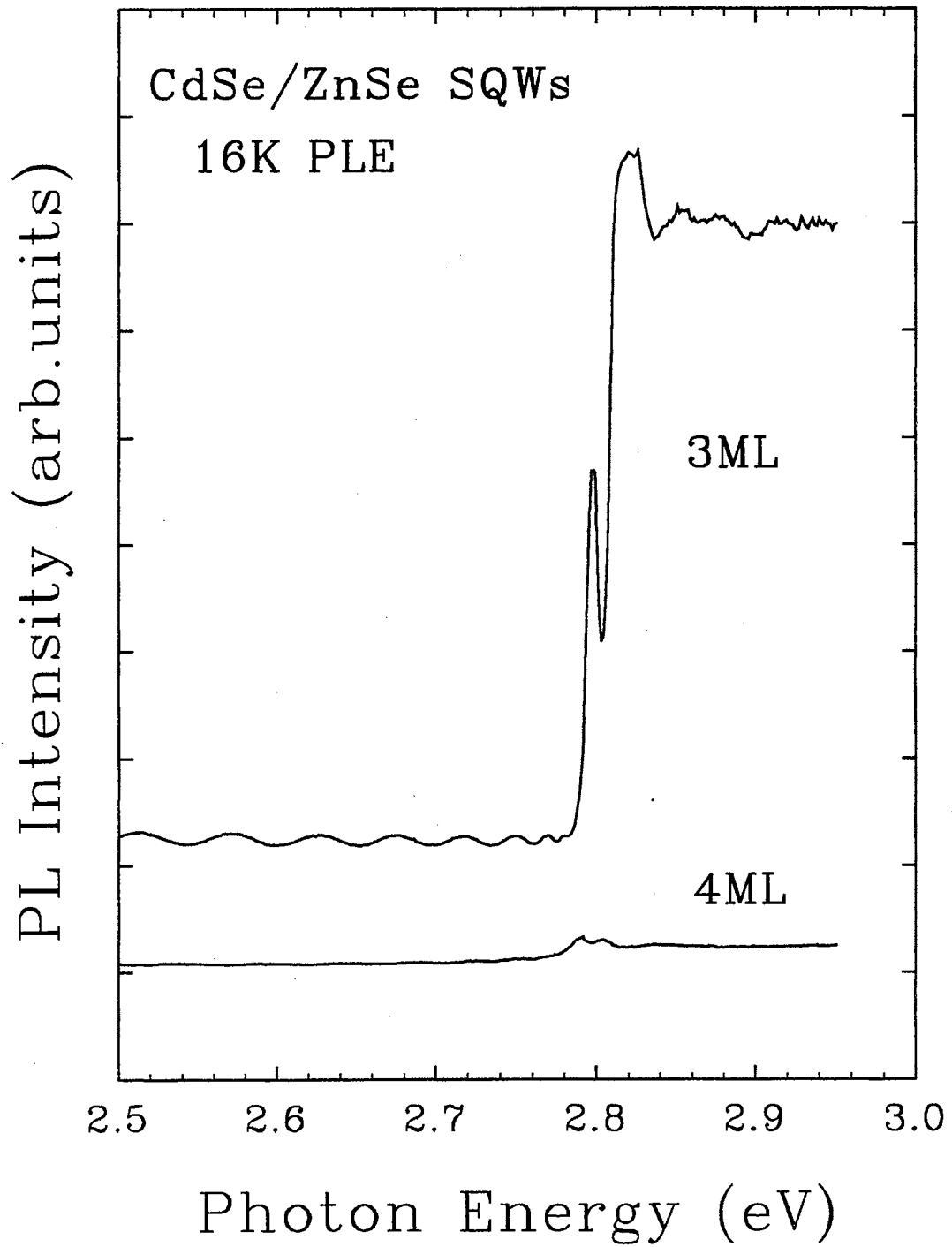


Figure 38. PLE spectra obtained near the ZnSe band gap for 3 ML and 4 ML SQW samples at atmospheric pressure.

Estimation of critical thickness

As shown in Fig. 6, there is a limited thickness of a strained epilayer grown commensurately on a substrate without the generation of any lattice-relaxed dislocations. There have been numerous theoretical estimates of the critical thickness of epilayers using various approaches, such as equilibrium of forces [11,124] and energy equilibrium conditions [40]. By considering the balance between the force exerted by the misfit strain and tension in the dislocation line, the critical thickness h_c , for the formation of misfit dislocations can be calculated by the self-consistent equation [124]

$$h_c = \frac{b(1 - \nu \cos^2 \theta)}{2\pi(1 + \nu)\epsilon \cos \lambda} \ln \left(\frac{h_c}{b} + 1 \right), \quad (84)$$

where b is the length of the Burgers vector of the dislocation. The Poisson ratio of the mismatched layer is denoted by ν . ϵ is the strain in the layer obtained by Eq. (6). The angle between the dislocation line and its Burgers vector is denoted by λ , and θ is the angle between the slip direction and that direction in the plane of the layer which is perpendicular to the line of intersection of the slip plane and interface. The values of these parameters are; $b = 0.04nm$, $\nu = 0.38$, $\epsilon = 0.067$, $\lambda = \pi/3$, $\theta = \pi/3$ [11].

The critical thickness evaluated using Eq. (84) is valid for a single epitaxial strained layer with one interface. For a strained layer with a cap layer, such as the QW structure, the value of the critical thickness will be twice as large because dislocations can be formed at both interfaces. For the case of a SL with both strained layers, the value will be four times larger than the case of single strained epilayer. In these multilayer cases, the growth rate of the epitaxial layers should be high enough that the strained layer does not have time to relax before the next layer starts to form [124]. If the lattice constant of the substrate or buffer layer is same as one of the layer material, only other layers will have strain. Therefore, when we consider that ternary and quaternary alloys with intermediate lattice constants can usually be grown, it is apparent that an enormous range of material combinations are available for commensurate strained layer structures.

By considering that two dislocations will be formed, one at each of the QW interfaces, the estimated critical thickness of the CdSe layer in a CdSe/ZnSe QW grown on ZnSe is about 16 Å, which corresponds to ~ 5 ML. The discrepancy between the critical thicknesses derived from the experiment and the theoretical estimation could be due to the imperfections in the sample.

MQW and SQW

We also note that the Γ -confined transition energies obtained from both MQW's are about 100 meV lower than those from SQW counterparts. Similar observations were reported by Zajicek *et al.* [113]. It is known that for strained superlattice and QW structures to be coherent with the substrate or buffer layer the individual layers must be thinner than their own critical thicknesses and the overall thickness of the structure as a whole must be also lower than some critical value [125,100]. When a well layer thickness or the thickness of the whole structure is greater than the critical value, the built-in strain will relax and arrays of dislocations will appear. As a result, a red shift of the photoluminescence peak can be observed with respect to the completely strained system. Since CdSe/ZnSe is a highly strained system with about 6.78 % of lattice mismatch, the whole MQW's thickness might be over the critical limit for a coherently strained structure. The lower PL emission position observed in MQW's compared to SQW's suggests that the MQW samples are at least partially relaxed. This can be qualitatively demonstrated by the PLE spectra in the energy region of the ZnSe bandgap as shown in Fig. 39, where a comparison of the 1 ML MQW with the 1 ML SQW is given. The increase of the PL emission observed in the SQW with the excitation energy above the ZnSe bandgap is almost completely washed out in the MQW's. This occurs because the number of carriers created in the buffer layer which diffuse into the MQW region are severely decreased by numerous nonradiative defects such as dislocations at and near the interface between the MQW structure and the ZnSe buffer layer.

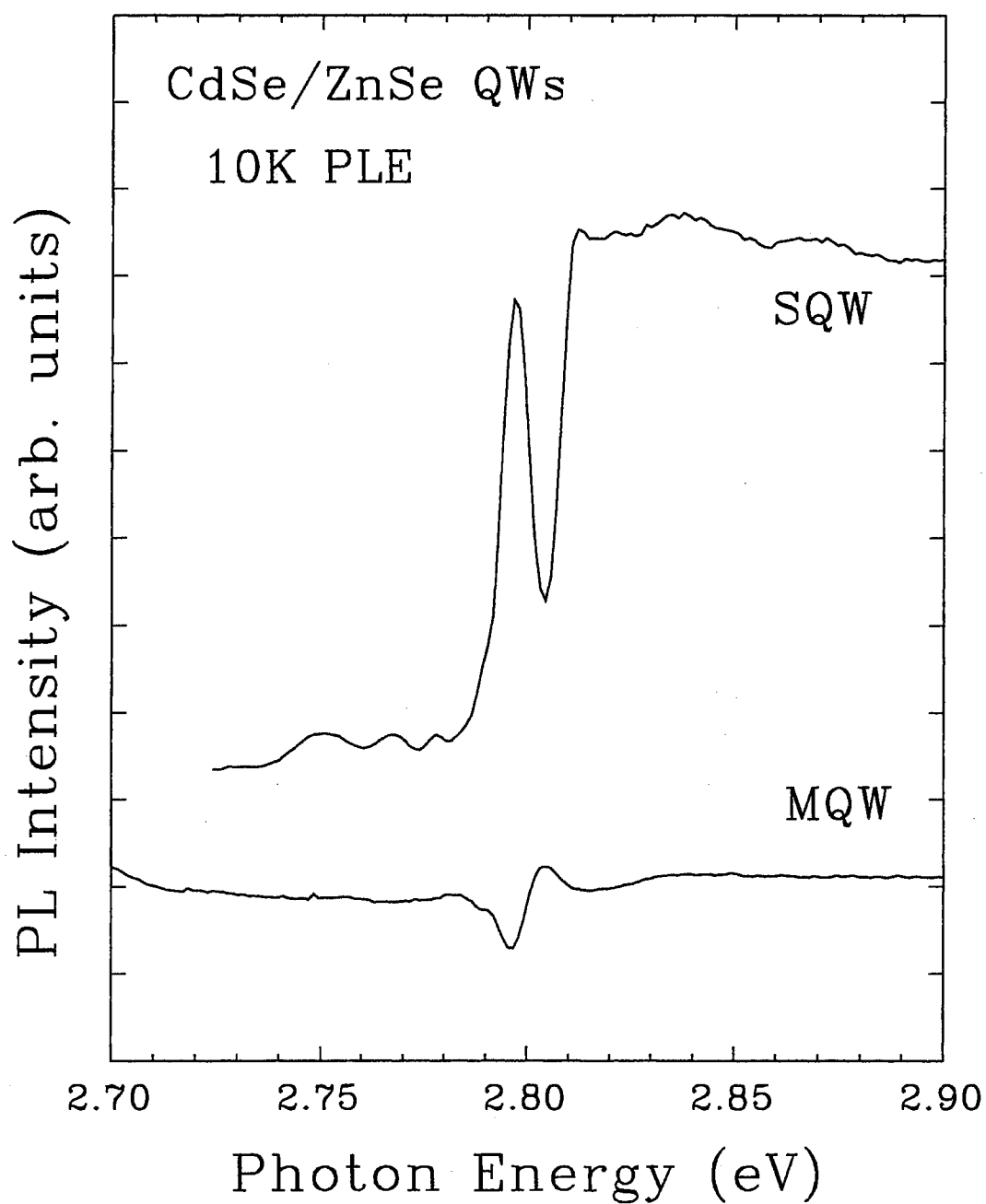


Figure 39. Photoluminescence excitation spectra obtained near the ZnSe band gap for 1ML SQW and MQW samples. The detection wavelengths were set to the respective PL peak positions of the samples.

Franz-Keldysh oscillation

Finally, as shown in Fig. 40, some oscillatory structures were observed in PLE spectra for all SQW samples. These structures are probably not related to higher confined levels in these QW's because the well width of samples are so narrow that theoretical calculation predicted only one confined electron level for all SQW samples. The possibility of this oscillatory structure as thin film interference was also eliminated because the periodic pattern didn't satisfy the formula for the interference. Also, the positions of the extrema in the oscillatory structures remained unchanged when the incident angle of the excitation light source was changed. Furthermore, since the energy differences between peaks are not the same and those peaks are not sharp, these peaks are not related to any phonon replicas.

When an electric field is built-in a QW or an electric field is externally applied on a QW, the electric field will change the shape of the quantum well destroying the symmetry of the quantum well structure and consequently changing the selection rules in the QW. In the presence of an electric field, previously unallowed transitions can be observed by destruction of the inversion symmetry of the QW. For example, the transition associated with 1s exciton is not allowed in the two-photon absorption in a symmetric QW with the polarization perpendicular to z-direction [126]. From the two-photon PLE spectra from these SQW samples, the transition associated with the $n = 1$ heavy-hole 1s exciton was observed, implying the destruction of the selection rules in the symmetric QW [127]. This suggests that there may be a built-in field in these SQW samples resulting in the oscillatory behavior in the PLE spectra.

If so, this built-in field may modulate the subband edges producing the oscillatory pattern in the absorption spectra. This phenomenon is known as Franz-Keldysh effect. From the extrema of this oscillation, we may be able to estimate the built-in field in the CdSe/ZnSe QW's. The extrema in FKO are given by [53]

$$m\pi = \varphi + \left(\frac{4}{3\pi}\right) [(E_m - E_g) / \hbar\theta]^{3/2}, \quad (85)$$

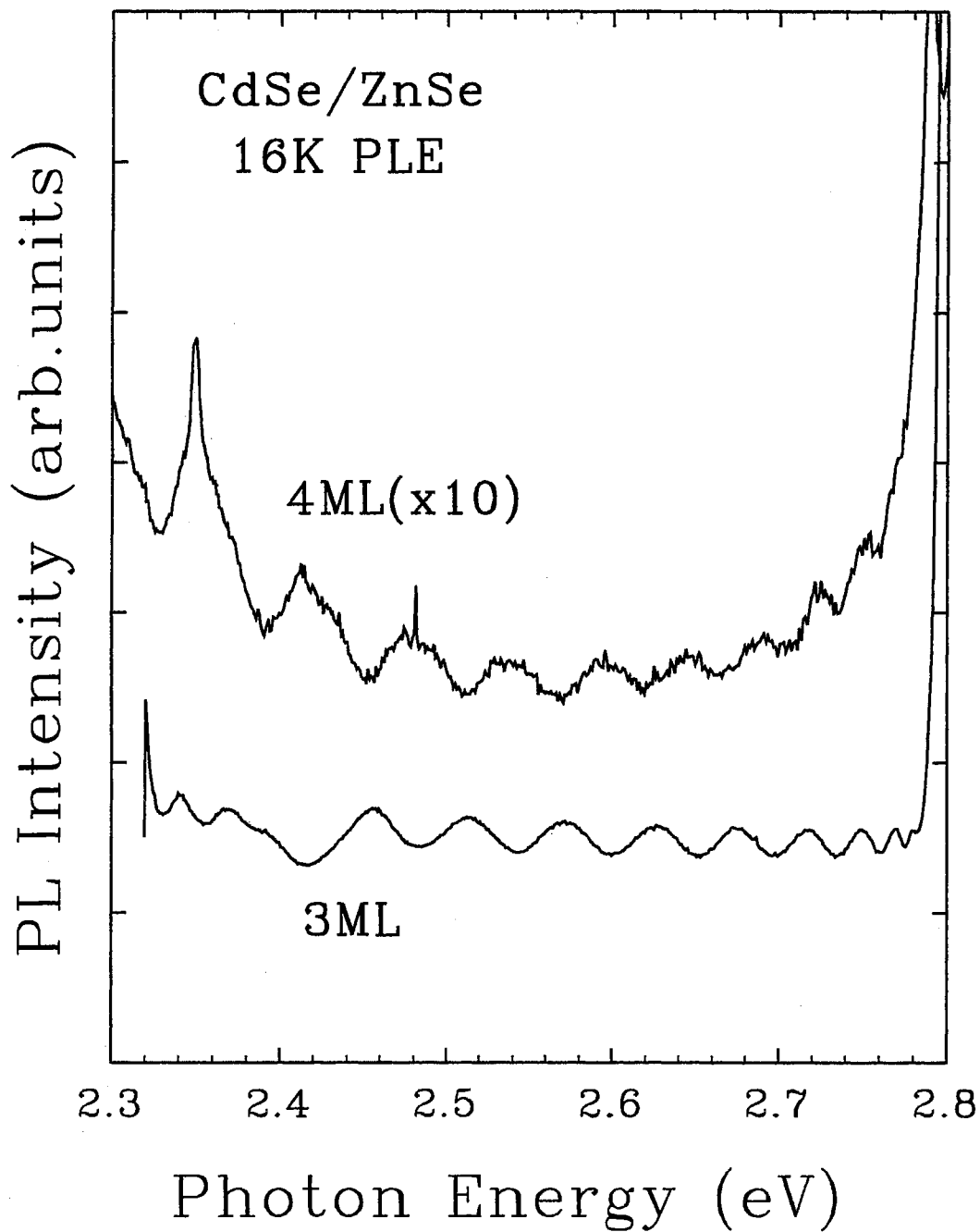


Figure 40. PLE spectra obtained from 3 ML and 4 ML CdSe/ZnSe SQWs at atmospheric pressure. The oscillatory structures were observed in PLE spectra of all SQW samples. The oscillation is shown not to be the interference pattern but to be Franz-Keldysh oscillation due to the built-in field.

where m is the index of the m^{th} extrema, φ is an arbitrary phase factor, E_m is the photon energy of the m^{th} extrema, E_g is the energy gap (here, E_{PL}), and $\hbar\theta$ is the electro-optical energy:

$$(\hbar\theta)^3 = e^2 \hbar^2 F^2 / 2\mu \quad (86)$$

where μ is the reduced interband effective mass for the electron and heavy-hole pair in the direction of electric field F :

$$\frac{1}{\mu} = \frac{1}{m_e^*} + \frac{1}{m_h^*}. \quad (87)$$

Plotted in Fig. 41 is the quantity $(4/3\pi)(E_m - E_g)^{3/2}$ as a function of m for the 3 and 4 ML CdSe/ZnSe SQW samples. The solid lines are least squares fits to Eq. (85). The slope of the solid line will be values of $(\hbar\theta)^{3/2}$. Thus, using Eqs. (85) and (86), the built-in field F can be obtained by

$$F = \frac{\sqrt{2\mu}}{e\hbar} (\hbar\theta)^{3/2}. \quad (88)$$

The calculated built-in field in the CdSe/ZnSe QW's are 1.36×10^5 and $1.35 \times 10^5 V/m$ for 3 ML and 4 ML samples, respectively. This field may be generated by the strain induced polarization. However, the reason for the built-in electric field in CdSe/ZnSe QW's is not clear at this moment, because it is known that the strain-induced piezoelectric field in a QW structure grown in [001] is zero, although it can be obtained in the strained QW's grown in the other directions such as [111] direction [128].

Conclusions

We have studied the optical properties of a variety of MBE grown highly strained CdSe/ZnSe QW samples (6.78 % of lattice mismatch) using low temperature PL, PLE, and PR measurements. High pressure photoluminescence measurements have also been performed to study the effect of hydrostatic pressure on strained CdSe/ZnSe SQW's with 1-4 ML of CdSe well width.

In general, the direct interband transitions from samples with well widths from 1/4 to 4 ML are found to vary in energy from 2.15 to 2.78 eV (450-577 nm),

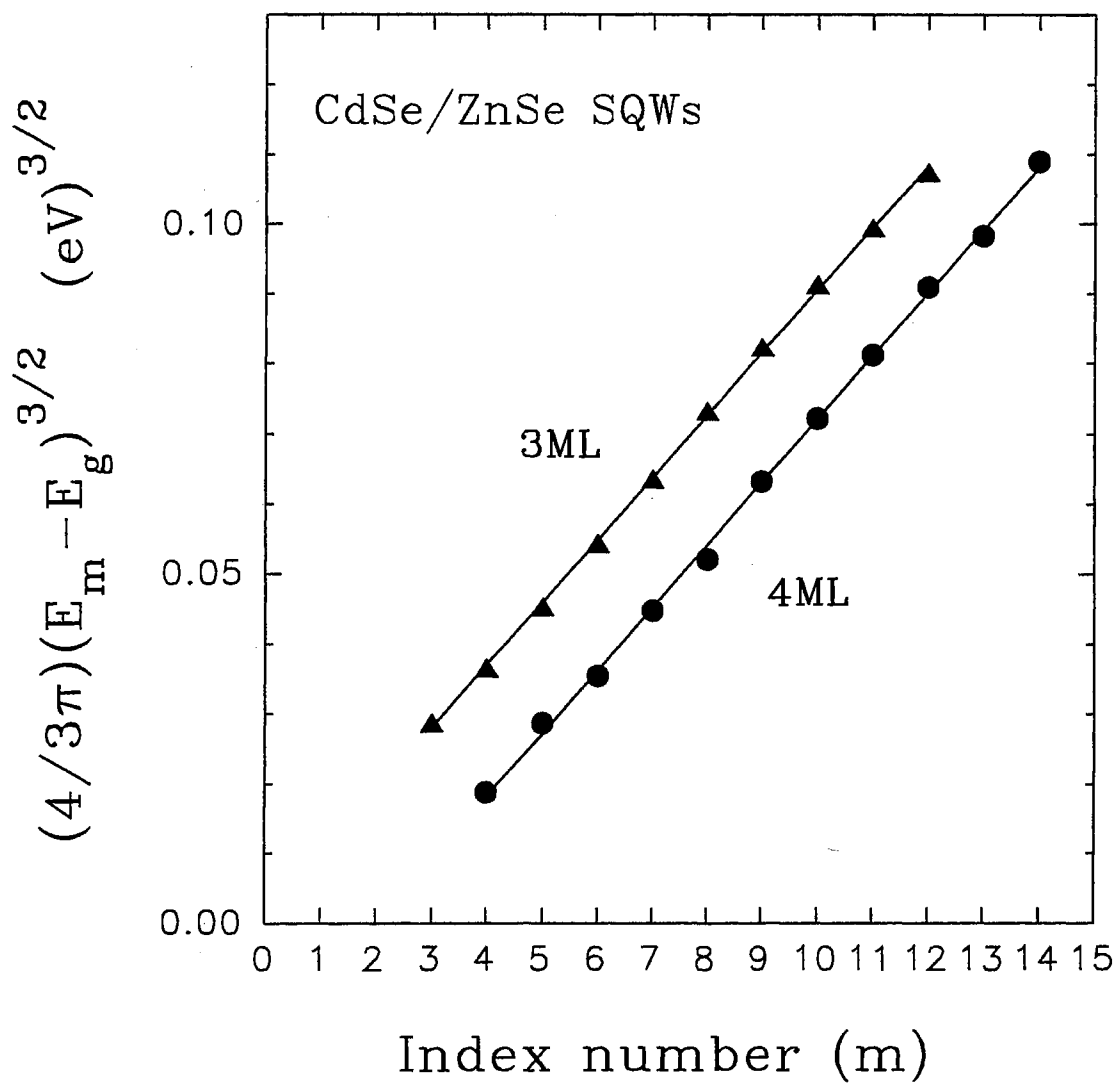


Figure 41. Quantity $(4/3\pi)(E_m - E_g)^{3/2}$ as a function of the index number m for 3 and 4 ML CdSe/ZnSe SQW samples. The solid lines are least-squares fits and the slope of this line yields $(\hbar\theta)^{3/2}$.

which covers almost the entire blue-green color range useful for optoelectronic device operation. Under applied pressure, the lowest confined excitonic transition peaks shifted to higher energy and their pressure coefficients are found to depend on the CdSe layer thickness. In particular, the excitonic interband transitions in the samples with 3 and 4 ML CdSe wells are found to show strong sublinear pressure dependence. A significant decrease in both the observed PL intensity and PLE signal level near the ZnSe band gap in the 4 ML sample indicates relaxation of the built-in strain has occurred. From this observation, it can be further inferred that the maximum number of monolayers of CdSe layer to be pseudomorphically grown on ZnSe to form a coherent QW structure should be less than four. The theoretically estimated the critical thickness of the this QW system was about 5 ML giving a good agreement.

The theoretical calculations for the strain effects on the band edges in this CdSe/ZnSe QW structure indicated that the light-hole band is formed as Type-II while the heavy-hole band edge is Type-I. The results of the confinement energy level calculations showed that these wells in these samples have only one confined electron and hole bands.

The discrepancy in the energy positions of interband transitions between the SQW and MQW samples with the same CdSe layer thickness is attributed to the strain relaxation occurring from the overall thickness of the MQW structure as a whole surpassing the critical limit for pseudomorphic growth of coherent strained MQW's.

The interesting observation of the oscillatory behavior in the PLE spectra for SQW's seems to be the Franz-Keldysh oscillation which might be due to the large strain induced built-in field. The estimated field is of the order of 10^5 V/m. The origin of the field is not clear at this point.

CHAPTER VII

CUBIC GaN EPILAYER GROWN ON A GaAs SUBSTRATE

Introduction

Recently, the wide band gap III-V nitrides have attracted enormous attention because of their importance in the science and technology of high temperature electronics and light-emitters operating in the blue and ultraviolet wavelength range [129]. There have been many efforts devoted to the preparation of high quality GaN crystals and epitaxial films using a variety of growth techniques on different substrates [130–137]. Although the normal crystal structure of GaN is wurtzite (hexagonal), GaN thin films have been successfully grown on semiconductor substrates with zinc blende structure by molecular beam epitaxy (MBE) and chemical vapor deposition (CVD) techniques [131,134,135,137]. Theoretical calculations predict that zinc blende GaN has a direct band gap at the center of Brillouin zone (Γ_1^c - Γ_{15}^c) [129,138,139]. So far, there have been a number of reports on the optical properties of GaN samples grown with different techniques [135,140–143]. It has been generally found that the PL spectra from GaN samples at atmospheric pressure, especially for GaN in the cubic phase, are quite complicated with multiple peaks near the band gap superimposed upon each other. It has been suggested that these spectral features are associated with various recombination processes such as free electron-bound hole (FB) and donor-acceptor (DA) pair transitions [135,141]. Even though the values are controversial, some physical properties for cubic and wurtzite GaN are listed in table VII. In this chapter, for the first time, the results are presented of the hydrostatic pressure dependence of low-temperature PL from

TABLE VII.

Some physical properties of the cubic and hexagonal GaN [144].

	zinc blende GaN	wurzite GaN
Band gap energy		
T=300 K	3.30±0.02 eV 3.45 eV 3.2 eV 3.231±0.008 eV*	3.39 eV
T=1.6 K	3.302±0.004 eV*	3.50 eV
Lattice Constant		
T=300K	a=4.42-4.55 Å a=4.54 Å a=4.531 Å a=4.5 Å a=4.52±0.005 Å	a=3.189 Å c=5.185 Å

*Ref. [145]

a zinc blende GaN epitaxial thin film grown on a (100) GaAs substrate by MBE over a pressure range up to 50 kbar.

Experimental results and discussion

The GaN thin film sample used in this work was grown on a semi-insulating (100) GaAs substrate by MBE [146]. Before the growth of the GaN epilayer, a GaAs buffer layer about $0.5 \mu\text{m}$ thick was grown to provide a clean and defect-free surface for the GaN deposition. The GaN was grown at approximately 620°C . The thickness of the GaN film is about $1.8 \mu\text{m}$. X-ray rocking curves were taken from the sample to verify the zinc blende crystal structure [146]. PL measurement was performed at 10 K on the GaN sample under hydrostatic pressure. The 3250 \AA line of a HeCd laser was used as the excitation source. The PL signal was collected in the backscattering geometry, dispersed by a 0.85 m double-grating spectrometer (SPEX1403) and measured using a photon counting system and a data acquisition system. The S-20 PMT was used for a detector.

There are a variety of possible transitions in a bulk semiconductor, as shown in Fig. 42. Some representative PL spectra of the cubic GaN measured at different pressures are shown in Fig. 43. The PL spectra show several resolved emission peaks which are indicated by arrows and labels of **a**, **b**, **c**, and **d** in the order of descending energy. The energy positions of those peaks measured at atmospheric pressure are (a) 3.472, (b) 3.268, (c) 3.199, and (d) $3.115 \pm 0.005 \text{ eV}$, respectively. At lower energies a few more spectral structures are observed, however, their energy positions could not be reliably obtained due to the weak signal level. Under applied pressure, all the spectral features shift to higher energy, which indicates that all the transitions are associated with the GaN band structure. The luminescence intensity of each individual structure in the spectrum decreases and the overall line shapes broaden as the applied pressure is increased. As shown in Fig. 43, a decrease of about a factor of five in intensity was observed at the highest pressure employed.

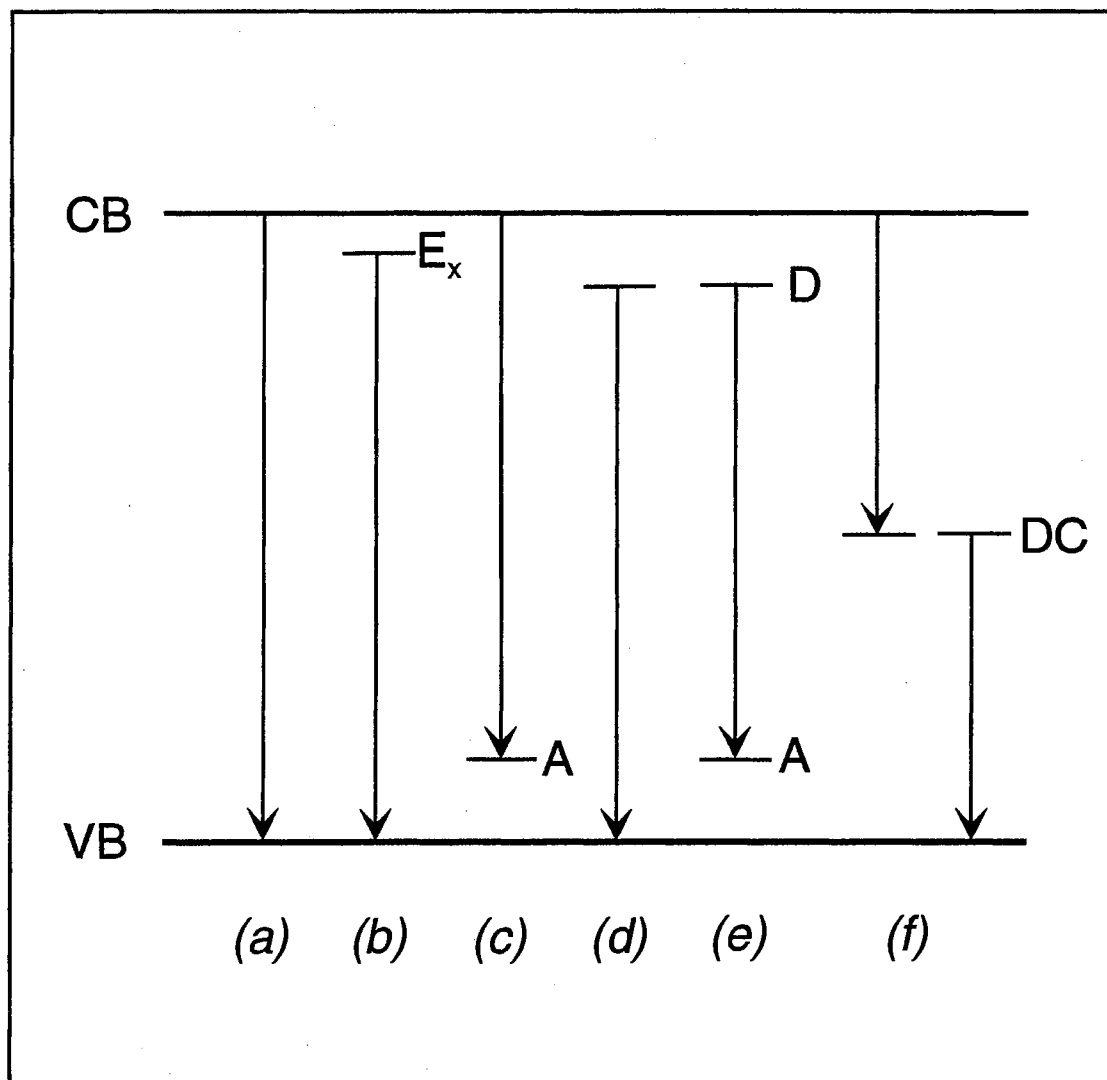


Figure 42. Schematic representation of various transitions in a bulk semiconductor. Transitions are associated with (a) band to band, (b) exciton, (c) free electron-bound hole, (d) bound-free hole, (e) donor-acceptor (DA) pair, (f) deep center (DC). E_x , D , and A are states of exciton, donor, and acceptor, respectively.

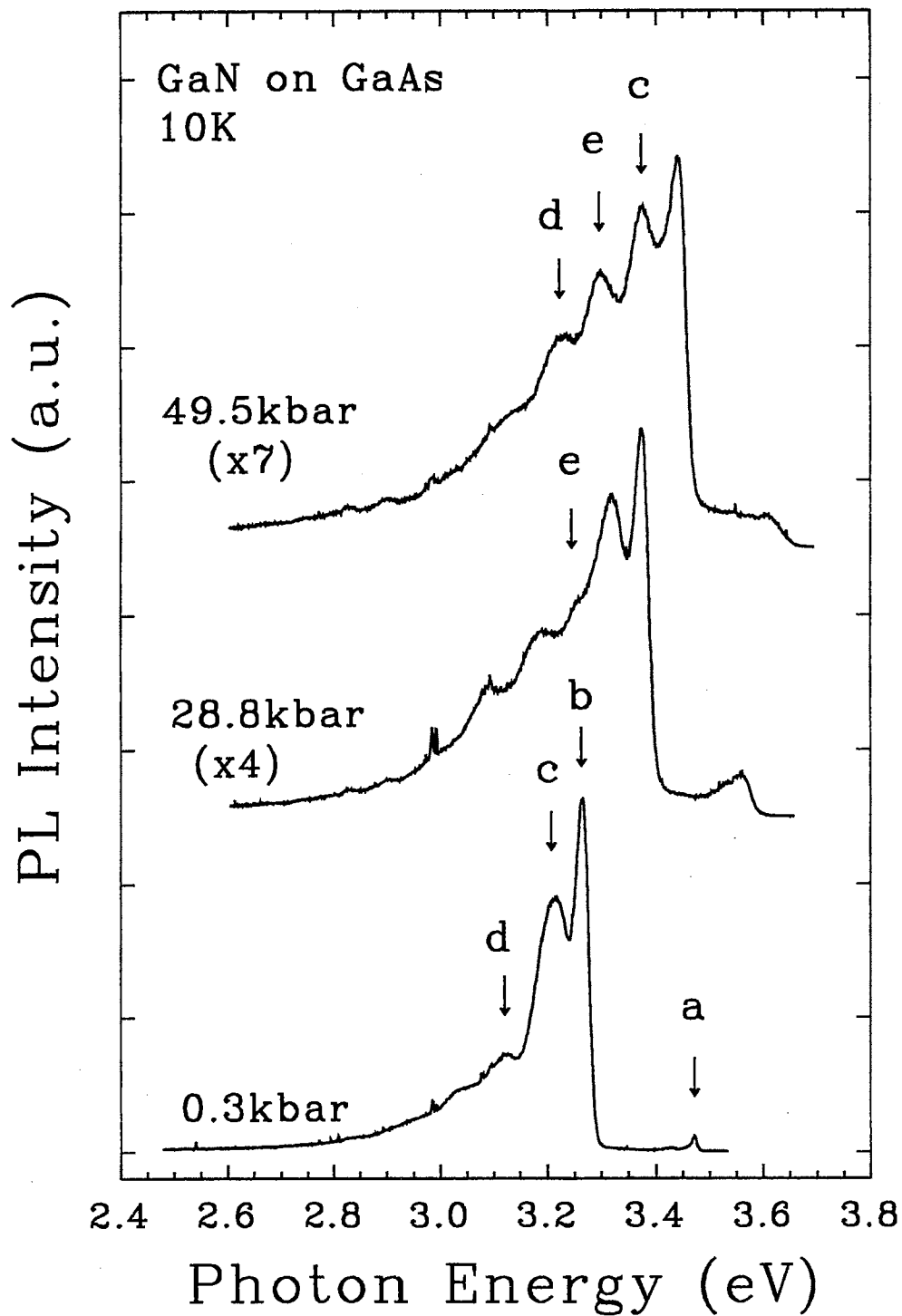


Figure 43. PL spectra of the GaN sample at several different pressures. The resolved luminescence peaks are indicated by arrows with different labels. An additional peak labeled by e shows up at pressures higher than 25 kbar.

The spectral feature **a** broadens and the signal-to-noise ratio decreases gradually with increasing pressure and finally becomes unresolvable. A very weak phonon-replica-like spectral structure with an energy 50 meV below the peak can also be observed in the PL spectrum measured at atmospheric pressure. This peak has been attributed to the luminescence from wurtzite GaN clusters formed in the cubic GaN thin film [146–149]. The strong sublinear pressure dependence of this peak, as shown in Fig. 45, and its broadened line shape at high pressure can be attributed to nonuniform local stress on wurtzite GaN domains. The predominant emissions **b** and **c** most likely originate from the radiative recombination associated with free electron-bound hole (FB) and donor-acceptor (DA) pair transitions, respectively [135,139,143].

We have performed a temperature dependent PL measurement on the sample to provide more information for the identification of these transitions. Fig. 44 shows PL spectra taken at different temperatures. As the temperature is increased, the luminescence intensity of peak **c** is found to drop drastically relative to that of peak **b**. Also, the line shape of peak **c** becomes slightly narrowed at higher temperatures before the peak disappears. This behavior of peak **c** is a characteristic of donor-accepted pair luminescence [150]. Peak **b** becomes the predominant feature of the whole spectrum at temperatures above 100 K. The significant decrease in the PL intensity of peak **c** at temperatures above 100 K is presumably due to the quenching of DA emission by thermal ionization.

One interesting observation as a result of the application of pressure on the sample is that another luminescence structure, marked by **e** in Fig. 43, emerges in between peaks **c** and **d**, gradually becoming well resolved at pressures above 30 kbar. Apparently this new structure could not be observed at atmospheric pressure since it is weak and superimposed on the other spectral features.

In Fig. 45, the change in energy position for each marked peak is plotted as a function of applied pressure. The solid lines drawn through the experimental points represent least-squares fits using the quadratic equation

$$E_i(P) = E_i(0) + \alpha_i P + \beta_i P^2, \quad (89)$$

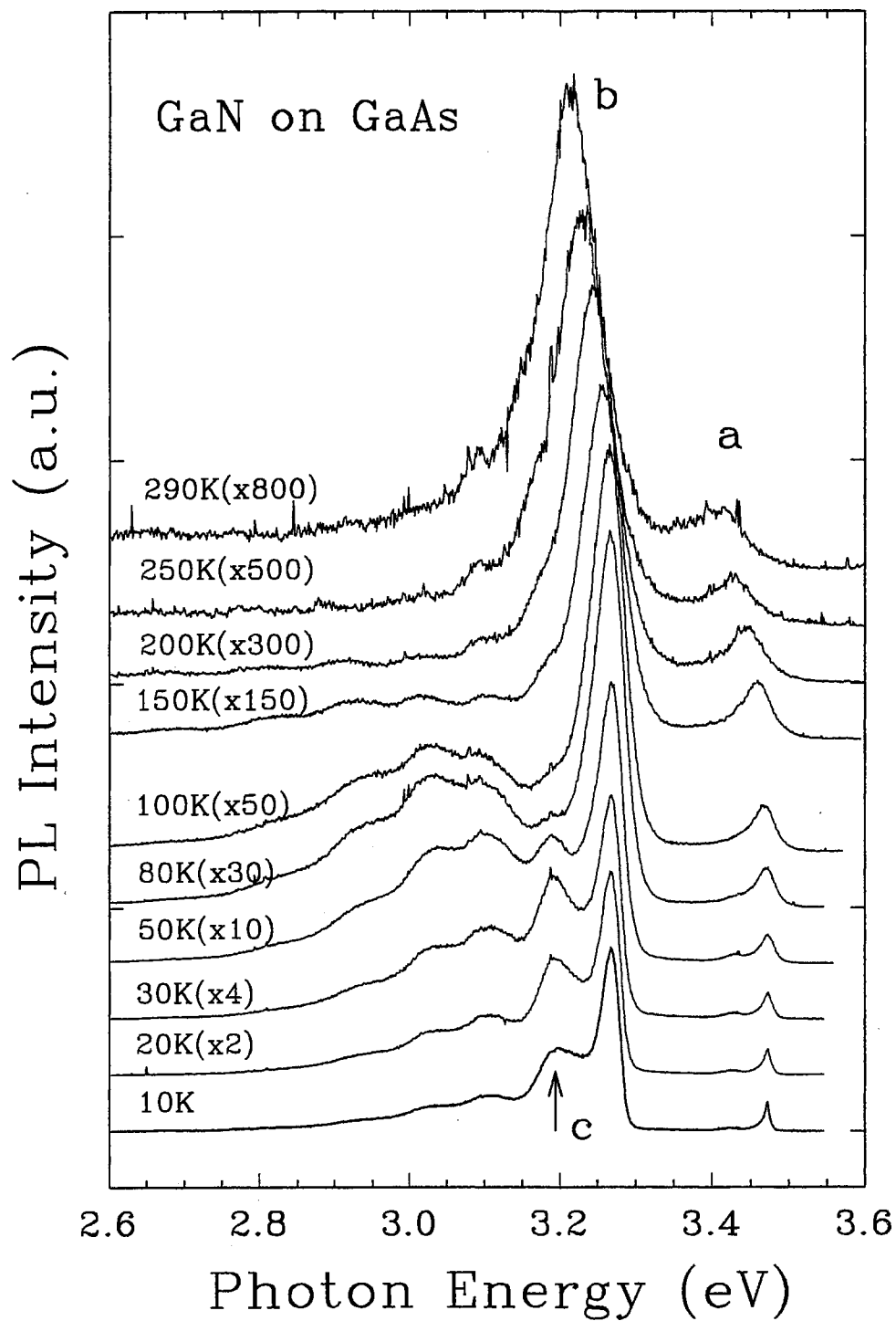


Figure 44. PL spectra of the GaN sample at different temperatures. The significant decrease in the PL intensity of peak c at temperatures above 100 K is presumably due to the quenching of DA emission by thermal ionization. Spectra were vertically shifted for a clarity.

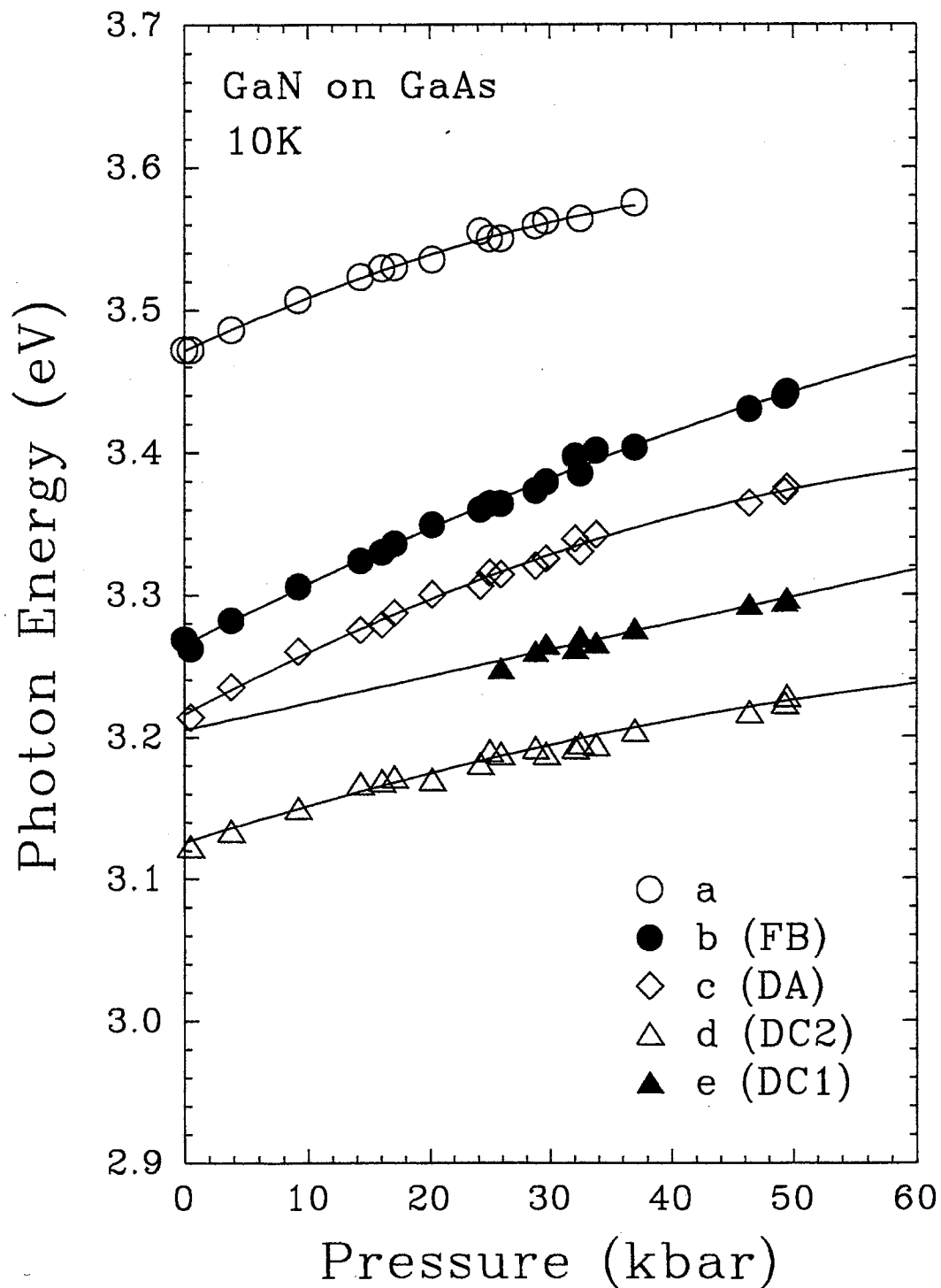


Figure 45. The variations of the energy positions for different PL emission structures of cubic GaN shown in Fig. 43 as a function of the hydrostatic pressure. The solid lines drawn through the experimental data points represent least-squares fits.

where i denotes different transitions such as FB and DA. Also, $E_i(P)$ and $E_i(0)$ are the transition energies of the peak i measured at the pressure P and at atmospheric pressure ($P = 0$), respectively. In Eq. (89), $\alpha_i = dE_i/dP$ and $\beta_i = d^2E_i/dP^2$ represent the linear and quadratic pressure coefficients of the peak i , respectively. Table VIII lists the linear and quadratic pressure coefficients of the various observed transition energies determined using the above Eq. (89). The transition energies for these peaks from the cubic GaN sample at atmospheric pressure are also listed. The band gap transition energy at atmospheric pressure and its pressure coefficient for the GaN in wurtzite structure are listed for comparison [151].

As seen in Table VIII, the pressure dependence of FB and DA transitions are comparable with the pressure coefficient of the band gap of bulk hexagonal GaN [151]. The larger values of the linear and quadratic pressure coefficients for DA transition compared to those of the FB transition are due to the uncertainty in determining the peak position because this peak overlaps with the emission feature **e** in the low pressure range. The pressure coefficients of the FB and DA transitions can be approximately regarded as those for the fundamental band gap of GaN in zinc blende structure, since the electronic states involved in the recombination processes for these two transitions can be described within the frame of the effective mass approximation and are expected to closely follow their respective band edges. Therefore, our results provide a measure of the pressure coefficient for the band gap of cubic GaN. In fact, the pressure coefficient of the FB transition should be considered to be more accurate than that of the DA transition because in the latter transition process a Coulombic interaction term needs to be taken into account.

Both emission structures **d** and **e** show that they have much smaller pressure coefficient than those of transitions **b** (FB), **c** (DA), and **a**. Such small pressure coefficients of peaks **d** and **e** rule out the possibility that they may come from phonon replicas. These two peaks do not follow any observed emission peaks with pressure as expected from phonon replicas. They most likely originate from the radiative recombination associated with some deep centers. This is because the pressure dependence of the energy level of a deep center is mainly determined by

TABLE VIII.

Energy positions and pressure coefficients for the various PL emission structures observed in this work and for the wurtzite GaN band gap.

	$E(0)$ (eV)	$\alpha = dE/dP$ (meV/kbar)	$\beta = d^2E/dP^2$ (meV/kbar ²)
a	3.472	4.0(4)	-3.4
b(FB)	3.268	4.4	-1.7
c(DA)	3.199	4.5(7)	-2.8
d(DC2)	3.115	2.7	-1.5
e(DC1)	$3.20 \pm 0.005^*$	1.8(8)	-
$E_g^{Hex}(\text{GaN})^\dagger$	3.503^\ddagger	$4.2(2)^\ddagger$	-

*Obtained by extrapolating linearly from data points at high pressures.

[†]Bulk crystal in wurtzite structure.

[‡]*Landolt-Bornstein, New Series* [151]

the composition of its wave function, which could consist of contributions from the whole of \vec{k} -space and from many bands [3]. Consequently, its pressure derivative depends on the composition of its wave function and does not follow any particular band edge. For example, the pressure coefficients of the donor-like deep level will be primarily determined by the pressure dependence of the average of different conduction band valleys [152]. The difference in the pressure coefficients of the emission peaks **d** and **e** suggests that their radiative recombination processes involve two different deep centers. Deep centers can be associated with different impurity species or various crystal defects, for example, vacancies can lead to different PL energy positions and pressure dependences. However, this is an issue requiring further study. By extrapolating the high pressure data, the energy position of the deep center related emission **e** at ambient pressure was estimated to be around 3.20 eV.

Conclusion

PL measurements on zinc blende GaN grown by MBE on a GaAs substrate have been performed at 10 K under hydrostatic pressure up to 50 kbar. The abundance of PL spectral structures indicates that a variety of radiative recombination processes are present. Among them, the free electron-bound hole (FB) and donor-acceptor pair (DA) transitions are the predominant processes. All PL structures shift to higher energy as the pressure increases. From these shifts, their pressure coefficients were determined. The pressure coefficients of the free electron-bound hole (FB) and donor-acceptor (DA) transitions obtained in this work can be used to describe the dependence of the fundamental band gap of cubic GaN based on the effective mass approximation. Application of pressure on the sample also reveals the existence of an additional luminescence structure, which is not observed at atmospheric pressure. The pressure coefficients of this pressure-induced peak and another peak are found to be much smaller compared to those of the FB and DA transitions. This suggests that their recombination processes are associated with some deep centers.

CHAPTER VIII

SUMMARY

Optical properties of strained semiconductor heterostructures have been investigated using various optical spectroscopic techniques, such as photoluminescence, photoluminescence excitation, photoreflectance and photomodulated transmission measurements. The effects of hydrostatic pressure on the optical interband transitions have been studied using a high pressure diamond anvil cell. In this study, it was shown that the hydrostatic pressure technique is a powerful tool for the optical investigation of semiconductors, both bulk and heterostructures.

The following samples, all strained, were studied in this work: GaAs/GaAs_xP_{1-x} MQW's, InAs_xP_{1-x}/InP MQW's, and CdSe/ZnSe binary QW's, and a cubic GaN epilayer. In Table IX, a summary of the built-in strain in these sample structures is presented. As shown in the table, the CdSe/ZnSe QW structure and cubic GaN epilayer have extremely high strain. The presented experimental results show that the successful growth of highly strained heterostructures allows many possible combinations of semiconductor materials providing the freedom to tailor the band gap. The deformation potential theory and envelope function approximation have been used to obtain the band alignment and interband transition energies as discussed in Chapter II.

One of the typical effects of pressure on the interband transitions in a QW is that a pressure induced Γ - X crossover can be expected with a drastic decrease of PL intensity and with the appearance of a new X -characteristic peak. In a GaAs/GaAs_{0.32}P_{0.68} SMQW, we have observed this pressure induced Γ - X crossover clearly. From this crossover we could determine the band offsets in the QW structure. The unstrained valence band offset for this sample was determined to be

0.09 ± 0.02 eV which corresponds to roughly 75:25 distribution in conduction and valence band offsets, $Q_v = \Delta E_v / \Delta E_g = 0.25$. This is the first band offset result obtained using the pressure-optical technique in the GaAs/GaAs_{1-x}P_x SMQW system. From the nature of the pressure-optical technique, this result is more direct and accurate than other indirect methods mentioned in Chapter IV.

We have also observed an emission associated with a deep center and its phonon replicas, which appeared at pressures higher than 17 kbar in the GaAs/GaAs_{0.39}P_{0.61} SMQW. With the analysis of the pressure dependent PL results, this level is attributed to donor-like deep center which is in the resonant state in the GaAs well layer located about 200 meV above bottom of the conduction band of GaAs. These deep levels did not allow the observation of the pressure induced Γ - X crossover by acting as capture centers for the cross-interface electrons. However, there was clear evidence of the pressure induced Γ - X crossover from the drastic reduction of the PL intensity. This result indicates that the observation of the pressure induced Γ - X crossover in QW's requires samples with good interface quality. The interface quality is not the only requirement in QW's to observe the pressure induced Γ - X crossover. Even though a QW sample has very good quality interfaces, we may not be able to observe the pressure induced Γ - X crossover. This is the case when the energy difference between the X -band edge of the barrier and Γ -band edges are so large that the crystal phase change occur before the pressure reaches for the Γ - X crossover. Since II-VI QW systems, such as CdSe/ZnSe QW's, usually have a large band gap energy at the X -point, it may be impossible to observe the pressure induced Γ - X crossover in these systems.

Excitonic interband transitions in InAs_xP_{1-x}/InP SMQW's have been investigated in Chapter V using low temperature PL, PLE and room temperature pressure dependent PT. Interband transitions are identified using theoretical calculations based on the envelope function approximation and deformation potential theory, taking into account the band nonparabolicity and the strain-induced mixing between light hole and spin orbital split-off bands. The modification of the effective mass in the light hole due to the mixing becomes crucial giving a better

fit to higher order ($n \geq 2$) interband transitions. In comparing the PLE³ and PT spectra, we observe a transition between the split-off hole band and the lowest confined electron state which appear only in the PT spectrum.

In Chapter VI, optical properties of all-binary CdSe/ZnSe quantum well structures grown on GaAs by MBE have been intensively studied. This material system is very attractive due to the transitions in the blue-green region. We have studied many sample structures such as submonolayer SQW's, nominal SQW's (1-4 ML) and two MQW's. In general, all samples give direct interband transitions in the energy range from 2.15 to 2.78 eV allowing the possibility of device applications over a wide spectral range. From pressure dependent PL measurements, the pressure coefficients of the PL transitions have been determined. Results show that the pressure coefficients of the lowest confined electron and heavy-hole subbands transitions ($\Gamma_{1e}-\Gamma_{1hh}$) are well width dependent such that the pressure coefficients decrease as well widths decrease. For both GaAs/GaAs_xP_{1-x} MQW's and CdSe/ZnSe SQW, the pressure coefficients for the $\Gamma_{1e}-\Gamma_{1hh}$ transitions were also found to be smaller than that of well materials in bulk. This phenomenon, as discussed in Chapter VI, is attributed to a combination of several competing mechanisms including effects of mixing of well and barrier wave functions, especially in narrow quantum wells. As shown in Table IX, the CdSe/ZnSe QW system is highly strained. As expected from the highly strained QW system, the critical thickness of the CdSe layer in the QW structure is very small, ~ 12 Å (less than 4 ML) as estimated from the pressure dependent PL and PLE results. This value is in a good agreement with the theoretically predicted critical layer thickness of 16 Å (~ 5 ML).

We observed oscillations in PLE spectra from 1, 2, 3 and 4 ML CdSe/ZnSe SQW's. This oscillation is not due to an interference pattern in the thin film. We believe that this oscillation is from the Franz-Keldysh effects due to the built-in field in the QW. This was supported by the two-photon PLE measurement which showed unallowed transitions due to the breaking of inversion symmetry of the QW with respect to the center of the QW. The built-in field will tilt the QW bands

resulting in the destruction of the inversion symmetry, by which the selection rules can be broken allowing new transitions. The estimated built-in field is of order of 10^5 V/cm. It is known that a QW grown in the (111) direction has a strong built-in field [128]. However, the reason for the built-in field in CdSe/ZnSe QW's grown in the (100) direction is not clear and further study is required.

Finally, pressure dependent PL of a cubic structure of GaN grown on a GaAs substrate by MBE has been studied as discussed in Chapter VII. This is the first pressure study on a cubic GaN heterostructure. Pressure coefficients of transitions have been determined. With the help of the temperature dependent PL from 10 K to room temperature, we could identify the origins of most transitions. Extra features appeared in the PL spectra at pressures higher than ~ 30 kbar, which have been attributed to deep centers. The pressure coefficients of these deep centers are smaller than those of the free-to-bound (FB) and donor-acceptor (DA) transitions. The pressure coefficients of the FB and DA transitions could be used for the pressure dependence of the fundamental gap of a cubic GaN.

TABLE IX.

Summary of built-in strains in all QW samples studied in this work. The GaAs/AlAs QW structure is listed for comparison.

QW System (well/barrier)	buffer (substrate)	strained layer	type of strain	strain (%)
GaAs _{1-x} P _x /GaAs	GaAs	GaAs _{1-x} P _x	tensile	0.87-1.42
InAs _x P _{1-x} /InP	InP	InAs _x P _{1-x}	compressive	1.62-1.94
CdSe/ZnSe	ZnSe	CdSe	compressive	6.78
Cubic GaN epilayer	GaAs	GaN	tensile	25.1
GaAs/AlAs	GaAs	AlAs	compressive	0.1

BIBLIOGRAPHY

1. L. Esaki and R. Tsu, IBM J. Res. Develop. **14**, 61 (1970).
2. C. Kittel, *Introduction to Solid State Physics*, 6th edition (John Wiley & Sons, Inc, New York, 1986).
3. B.K. Ridley, *Quantum Processes in Semiconductors*, (Oxford University, New York, 1988), chap.2.
4. G. Bastard, Phys. Rev. B **24**, 5693 (1981).
5. G. Bastard, Phys. Rev. B **25**, 7584 (1982).
6. G. Bastard and J.A. Brum, IEEE J. Quantum Electron. **QE-22**, 1625 (1986).
7. W.J. Schaff, P.J. Tasker, M.C. Foicy, and L.F. Eastman, in *Semiconductors and Semimetals*, edited by R. Dingle (Academic, New York, 1991), Vol. **33**, p.73.
8. H. Heinrich and J.M. Langer, in *Festkörperprobleme* **26**, (1986) p.251.
9. See, e.g., *Semiconductors and Semimetals*, edited by R. Dingle (Academic, New York, 1987) Vol. 24.
10. L. Esaki, in *Physics and Applications of Quantum Wells and Superlattices*, edited by E.E. Mendez and K. von Klitzing (Plenum Press, New York, 1987) NATO ASI series B: Physics Vol. 170.
11. P.J. Parbrook, B. Henderson, K.P.O'Donnell, P.J. Wright, and B. Cockayne, J. Crystal Growth **117**, 492 (1992).
12. Z.Q. Zhu, H. Yoshihara, K. Takebayashi, and T. Yao, Appl. Phys. Lett. **63**, 1678 (1993).
13. V.A. Wilkinson, A.D. Prins, D.J. Dunstan, L.K. Howard, and M.T. Emeny, J. Electronic Materials **20**, 509 (1991).
14. S.R. Kurtz, G.C. Osbourn, R.M. Biefeld, L.R. Dawson, and H.J. Stein, Appl. Phys. Lett. **52**, 831 (1988).
15. S.R. Kurtz, R.M. Biefeld, L.R. Dawson, I.J. Fritz, and T.E. Zipperian, Appl. Phys. Lett. **53**, 1961 (1988).

16. S.R. Kurtz, L.R. Dawson, R.M. Biefeld, and G.C. Osbourn,, SPIE **930**, 101 (1988).
17. I.J. Fritz, J.E. Schriber, E.D. Jones, T.J. Drummond, and G.C. Osbourn, in *Proc. Int. Symp. on GaAs and Related Compounds*, (IOP publishing, London, England, 1986) p.233.
18. G.C. Osbourn, J. Vac. Sci. Technol. **21**, 469 (1982).
19. P.L. Gourly and R.M. Biefeld, J. Vac. Sci. Technol. **21**, 473 (1982).
20. P.L. Gourly and R.M. Biefeld, Appl. Phys. Lett. **45**, 749 (1984).
21. M.-E. Pistol, M.R. Leys, and L. Samuelson, Phys. Rev. B **37**, 4664 (1988).
22. M.-E. Pistol and X. Liu, Phys. Rev. B **45**, 4312 (1992).
23. F.H. Pollak, in *Semiconductors and Semimetals*, edited by T.P. Pearsall (Academic, New York, 1990), Vol. 32, p.17.
24. F.H. Pollak, Surface Science **37**, 863 (1973).
25. E.O. Kane, *Semiconductors and Semimetals*, edited by R.K. Willardson and A.C. Beer (Academic, New York, 1966) Vol.1, p.1.
26. L. Laude, F.H. Pollak, and M. Cardona, Phys. Rev. B **3**, 2623 (1971).
27. E.O. Kane, J. Phys. Chem. Solids **1**, 249 (1957).
28. E.O. Kane, in *Physics of III-V Compounds*, edited by R.K. Willardson and A.C. Beer (Academic, New York, 1966) Vol.1, p.75.
29. E.O. Kane, in *Narrow Gap Semiconductors: Physics and Applications*, edited by W. Zawadzki (Springer-Verlag, Berlin, 1980), p.13.
30. J.M. Schulman and Y.C. Chang, Phys. Rev. B **24**, 4445 (1981).
31. M. Jaros and K.B. Wong, J. Phys. C **17**, L765 (1984).
32. R. Dingle, A.C. Gossard, and W. Wiegmann, Phys. Rev. Lett. **34**, 1327 (1975).
33. R. Dingle, W. Wiegmann, and C.H. Henry, Phys. Rev. Lett. **33**, 827 (1974).
34. R.C. Miller, D.A. Kleinmann, and A.C. Gossard, Phys. Rev. B **29**, 7085 (1984).
35. R.C. Miller, A.C. Gossard, and D.A. Kleinmann, Phys. Rev. B **32**, 5443 (1985).
36. G. Duggan, H.I. Ralph, and K.J. Moore, Phys. Rev. B **32**, 8395 (1985).

37. D.C. Rogers and R.J. Nicholas, *J. Phys. C* **18**, L891 (1985).
38. U. Venkateswaran, M. Chandrasekhar, H.R. Chandrasekhar, B.A. Vojak, F.A. Chambers, and J.M. Meese, *Phys. Rev. B* **33**, 8416 (1986).
39. D.J. Wolford, T.F. Keuch, J.A. Bradley, M.A. Gell, D. Ninno, and M. Jaros, *J. Vac. Sci. Technol.* **B4**, 1043 (1986).
40. R. People, A. Jayaraman, S.K. Sputz, J.M. Vandenberg, D.L. Sivco, and A.Y. Cho, *Phys. Rev. B* **45**, 6031 (1992).
41. H.Q. Hou, L.J. Wang, R.M. Tang, and J.M. Zhou, *Phys. Rev. B* **42**, 2926 (1990).
42. W. Shan, X.M. Fang, D. Li, S. Jiang, S.C. Shen, H.Q. Hou, W. Feng, and J.M. Zhou, *Phys. Rev. B* **43**, 14615 (1991).
43. M.A. Gell, D. Ninno, M. Jaros, D.J. Wolford, T.F. Keuch, and J.A. Bradley, *Phys. Rev. B* **35**, 1196 (1987).
44. M.S. Burdis, R.T. Phillips, N.R. Couch, and M.J. Kelly, *Phys. Rev. B* **41**, 2855 (1990).
45. V.A. Wilkinson, A.D. Prins, J.D. Lamkin, E.P. O'Reilly, D.J. Dunstan, L.K. Howard, and M.T. Emeny, *Phys. Rev. B* **42**, 3113 (1990).
46. J.H. Chen, J.R. Site, I.L. Spain, M.J. Hafin, and G.Y. Robinson, *Appl. Phys. Lett.* **58**, 744 (1991).
47. W. Shan, X.M. Fang, D. Li, S. Jiang, S.C. Shen, H.Q. Hou, W. Feng, and J.M. Zhou, *Appl. Phys. Lett.* **57**, 475 (1990).
48. M. Gerling, M.-E. Pistol, L. Samuelson, W. Seifert, J.-O. Fornell, and L. Ledebø, *Appl. Phys. Lett.* **59**, 806 (1991).
49. P.Y. Yu and P. Welber, *Solid State Commun.* **25**, 209 (1978).
50. H. Muller, R. Trommer, and M. Cardona, *Phys. Rev. B* **21**, 4879 (1980).
51. D. Olega, H. Muller, and M. Cardona, *Phys. Rev. B* **22**, 894 (1980).
52. M. Leroux, G. Pelous, F. Raymond, and C. Verie, *Appl. Phys. Lett.* **46**, 288 (1985).
53. D.E. Aspnes, in *Handbook on Semiconductors* edited by T.S. Moss (North-Holland, New York, 1980) Vol. 2, p.109.
54. M. Cardona, in *Festkörperprobleme X*, (1970) p.125.

55. O.J. Glembocki and B.V. Shanabrook, in *Semiconductors and Semimetals*, edited by D.G. Seiler and C.L. Littler (Academic, New York, 1992), Vol. 36, p.221.
56. E.Y. Wang, W.A. Albers, and C.E. Bleil, in *II-IV Semiconducting Compounds* edited by Thomas (Benjamin, New York, 1967) p. 136.
57. O.J. Glembocki, SPIE **1286**, 2 (1990).
58. B.V. Shanabrook, B.V. Glembocki, and W.T. Beard, Phys. Rev. B **35**, 2540 (1987).
59. X. Yin, F.H. Pollak, L. Pawlowicz, T. O'Neill, and M. Hafizi, Appl. Phys. Lett. **56**, 1278 (1990).
60. O.J. Glembocki and B.V. Shanabrook, Superlattices and Microstructures **5**, 603 (1989).
61. B.O. Seraphin and N. Bottka, Phys. Rev. **145**, 628 (1966).
62. H. Shen, X.C. Shen, F.H. Pollak, and R.N. Sacks, Phys. Rev. B **36**, 3487 (1987).
63. O.J. Glembocki and B.V. Shanabrook, SPIE **12**, 794 (1987).
64. W.F. Sherman and A.A. Stadtmuller, *Experimental Techniques in High-Pressure Research*, (John Wiley & Sons Ltd., London, 1986) p.349.
65. J.C. Jamieson, A.W. Lawson, and N.D. Nachtrieb, Rev. Sci. Instrum. **30**, 1016 (1959).
66. C.E. Weir, E.R. Lippincott, A.V. Valkenburg, and E.N. Bunting, J. Res. Natl. Bur. Stand. Sec. A **63**, 55 (1959).
67. G.J. Piermarini, S. Block, and J.S. Barnett, J. Appl. Phys. **44**, 6377 (1973).
68. J.H. Burnett, H.M. Cheong, and W. Paul, Rev. Sci. Instrum. **61**, 3904 (1990).
69. I.F. Silvera and R.J. Wijngaarden, Rev. Sci. Instrum. **56**, 121 (1985).
70. H.M. Cheong, Ph.D thesis, Harvard University, 1993.
71. G.I. Ng, W.P. Hong, D. Pavlidis, M. Tutt, and P.K. Bhattacharya, IEEE Electron. Device Lett. **9**, 439 (1988).
72. K.B.Chough, T.Y. Chang, M.D. Feuer, N.J. Sauer, and B. Lalevic, IEEE Trans. electron. Devices **ED-38**, 2708 (1991).
73. H.Q. Hou, C.W. Tu, W. Shan, S.J. Hwang, J.J. Song, and S.N.G. Chu, J. Vac. Sci. Technol. B **11**, 854 (1993).

74. H.Q. Hou, B.W. Liang, T.P. Chin, and C.W. Tu, *Appl. Phys. Lett.* **59**, 292 (1991).
75. *Landolt-Borstein*, edited by O. Madelung (Springer-Verlag, Berlin, 1988), New Series, Vol. 22a.
76. R. People and S.K. Sputz, *Phys. Rev. B* **41**, 8431 (1990).
77. R.L. Greene and K.K. Bajaj, *Phys. Rev. B* **31**, 6498 (1985).
78. C.G. Van de Walle and R.M. Martin, *Phys. Rev. B* **34**, 8154 (1987).
79. H. Kroemer, W.Y. Chien, J.S. Harris, Jr., and D.D. Edwall, *Appl. Phys. Lett.* **36**, 295 (1980).
80. J.M. Ballingall, C.E.C. Wood, and L.F. Eastman, *J. Vac. Sci. Technol. B* **1**, 675 (1983).
81. S.P. Kowalczyk, W.J. Schaffer, E.A. Kraut, and R.W. Grant, *J. Vac. Sci. Technol.* **20**, 705 (1982).
82. D.J. Wolford and J.A. Bradley, *Solid State Commun.* **53**, 1069 (1985).
83. M. Mizuta, M. Tachikawa, H. Kukimoto, and S. Minomura, *Jpn. J. Appl. Phys.* **24**, L143 (1985).
84. M. Tachikawa, T. Fujisawa, H. Kukimoto, A. Shibata, G. Oomi, and S. Minomura, *Jpn. J. Appl. Phys.* **24**, L892 (1985).
85. M.F. Li, P.Y. Yu, E.R. Welber, and W. Hansen, *Appl. Phys. Lett.* **51**, 349 (1987).
86. M.F. Li, P.Y. Yu, E.R. Welber, and W. Hansen, *Phys. Rev. B* **36**, 4531 (1987).
87. X. Liu, L. Samuelson, M.-E. Pistol, M. Gerling, and S. Nilsson, *Phys. Rev. B* **42**, 11791 (1990).
88. H.Q. Hou, private communication.
89. T.P. Pearsall, *GaInAsP Alloy Semiconductors* (Wiley, New York, 1982).
90. H.C. Casey, Jr. and M.B. Panish, *Heterostructure Lasers* (Wiley, New York, 1978).
91. H. Asonen, K. Rakennus, K. Tappura, M. Hovinen and M. Pessa, *J. Crystal Growth* **105**, 101 (1990).
92. W.T. Tsang, M.C. Wu, T. Tanbun-Ek, R.A. Logan, S.N.G. Chu, and A.M. Sergent, *Appl. Phys. Lett.* **57**, 2065 (1990).

93. P.J. Wang and B.W. Wessels, *Superlattices and Microstructures* **4**, 251 (1988).
94. R.P. Schnider, Jr. and B.W. Wessels, *Superlattices and Microstructures* **6**, 287 (1989).
95. R.P. Schnider, Jr. and B.W. Wessels, *Appl. Phys. Lett.* **54**, 1142 (1989).
96. R.P. Schnider, Jr. and B.W. Wessels, *J. Electron. Mater.* **20**, 1117 (1991).
97. H.Q. Hou, C.W. Tu and S.N.G. Chu, *Appl. Phys. Lett.* **58**, 2954 (1991).
98. H.G. Hasegawa, *Phys. Rev.* **129**, 1029 (1963).
99. D. Gershoni, H. Temkin, M.B. Panish, and R.A. Hamm, *Phys. Rev. B* **39**, 5531 (1989).
100. J.Y. Marzin, J.M. Gerard, P. Voisin, and J.A. Brum, in *Semiconductors and Semimetals*, edited by T.P. Pearsall (Academic, New York, 1990), Vol. 32, p.55.
101. See, e.g., M. Kobayashi, R.L. Gunshor, and L.A. Kolodziejski, in *Widegap II-VI compounds for Opto-electronic Applications*, edited by H.E. Ruda (Chapman & Hall, London, 1992) p.124.
102. M.A. Haase, J. Qiu, J.M. DePuydt, and H. Cheng, *Appl. Phys. Lett.* **59**, 1272 (1991).
103. H. Jeon, J. Ding, W. Patterson, A.V. Nurmikko, W. Xie, D.C. Grillo, M. Kobayashi, and R.L. Gunshor, *Appl. Phys. Lett.* **59**, 3619 (1991).
104. H. Jeon, J. Ding, A.V. Nurmikko, W. Xie, M. Kobayashi, and R.L. Gunshor, *Appl. Phys. Lett.* **60**, 892 (1992).
105. H. Okuyama, T. Miyajima, F. Hiei, and M. Ozawa, *Electron. Lett.* **28**, 1798 (1992).
106. S. Itoh, H. Okuyama, S. Matsumoto, N. Nakayama, F. Hiei, and M. Ozawa, *Electron. Lett.* **29**, 766 (1993).
107. See, e.g., Harry E. Ruda, *Widegap II-VI Compounds for Opto-electronic Applications* (Chapman & Hall, London, 1992).
108. P.J. Parbrook, P.J. Wright, B. Cockayne, A.G. Cullis, B. Henderson, and K.P. O'Donnell, *J. Crystal Growth* **106**, 503 (1990).
109. F. Yang, P.J. Parbrook, B. Henderson, K.P. O'Donnell, P.J. Wright, and B. Cockayne, *J. Luminescence* **53**, 427 (1992).
110. S. Fujita, Y.H. Wu, Y. Kawakami, and S. Fujita, *J. Appl. Phys.* **72**, 5233 (1992).

111. Z.L. Peng, J. Li, W.H. Yao, L. He, X.Y. Cheng, and S.X. Yuan, *Jpn. J. Appl. Phys.* **11B**, 31 (1992).
112. P. Juza, H. Zajicek, H. Sitter, M. Helm, W. Faschinger, and K. Lischka, *Appl. Phys. Lett.* **61**, 3133 (1992).
113. H. Zajicek, P. Juza, E. Abramof, O. Pankratov, H. Sitter, M. Helm, G. Brunthaler, W. Faschinger, and K. Lischka, *Appl. Phys. Lett.* **62**, 717 (1993).
114. H.Y.A. Chung, N. Uhle, and T. Tschudi, *Appl. Phys. Lett.* **63**, 1378 (1993).
115. N. Samarth, H. Luo, J.K. Furdyna, S.B. Qadri, Y.R. Lee, A.K. Ramdas, and N. Otsuka, *Appl. Phys. Lett.* **54**, 2680 (1989).
116. N. Samarth, H. Luo, J.K. Furdyna, R.G. Alonso, Y.R. Lee, A.K. Ramdas, S.B. Qadri, and N. Otsuka, *Appl. Phys. Lett.* **56**, 1163 (1990).
117. T. Yao, M. Fujimoto, S.K. Chang, and Tanino, *J. Cryst. Growth* **111**, 823 (1991).
118. Z.Q. Zhu, private communication.
119. K. Shahzad, D.J. Olego, and D.A. Cammack, *Phys. Rev. B* **39**, 13016 (1989).
120. S. Ves, K. Strossner, N.E. Christensen, C.K. Kim, and M. Cardona, *Solid State Commun.* **56**, 479 (1985).
121. J.R. Mei and V. Lemos, *Solid State Commun.* **52**, 785 (1984).
122. R.J. Thomas, H.R. Chandrasekhar, M. Chandrasekhar, N. Samarth, H. Luo, and J. Furdyna, *Phys. Rev. B* **45**, 9505 (1992).
123. P. Lefebvre, B. Gil, and H. Mathieu, *Phys. Lett. B* **35**, 5630 (1987).
124. J.W. Matthews, and A.E. Blakslee, *J. Crystal Growth* **29**, 273 (1975).
125. J. Cibert, Y. Gobil, L.S. Dang, S. Tatarenko, G. Feuillet, P.H. Jouneau, and K. Saminadayar, *Appl. Phys. Lett.* **56**, 292 (1990).
126. A. Shimizu, *Phys. Rev. B* **40**, 1403 (1989).
127. J.M. Hays and J.J. Song, unpublished.
128. C. Mailhot and D.L. Smith, *Solid State and Materials Sciences* **16**, 132 (1990).
129. S. Strite and H. Morkoc, *J. Vac. Sci. Technol.* **B10**, 1237 (1992).
130. H. Amano, M. Kito, K. Hiramatsu, and I. Akasaki, *Jpn. J. Appl. Phys.* **28**, L2112 (1989).

131. M.J. Paisley, Z. Sitar, J.B. Posthill, and R.F. Davis, *J. Vac. Sci. Technol.* **A7**, 701 (1989).
132. K.L. Ho, K.F. Jensen, J.W. Hwang, W.L. Gladfelter, and J.F. Evans, *J. Cryst. Growth* **107**, 376 (1991).
133. K. Hiramatsu, H. Amano, I. Akasaki, H. Fato, N. Koide, and K. Manabe, *J. Cryst. Growth* **107**, 509 (1991).
134. T. Lei, M. Fanciulli, R.J. Molnar, T.D. Moustakas, R.J. Graham, and J. Scanlon, *Appl. Phys. Lett.* **59**, 944 (1991).
135. S. Strite, J. Ruan, Z. Li, A. Salvador, H. Chen, D.J. Smith, W.J. Choyke, and H. Morkoc, *Vac. Sci. Technol.* **B9**, 1924 (1991).
136. T. Detchprohm, K. Hiramatsu, H. Amano, and I. Akasaki, *Appl. Phys. Lett.* **61**, 2688 (1992).
137. M.E. Lin, G. Xue, G.L. Zhou, J.E. Greene, and H. Morkoc, *Appl. Phys. Lett.* **63**, 932 (1993).
138. B.J. Min, C.T. Chan, and K.M. Ho, *Phys. Rev. B* **45**, 1159 (1992).
139. A. Robio, J.L. Corkill, M.L. Cohen, E.L. Shirley, and S.G. Louie, *Phys. Rev. B* **48**, 11810 (1993).
140. J.I. Pankove, J.E. Berkeyheiser, H.P. Maruska, and J. Wittke, *Solid State Commun.* **8**, 1051 (1970).
141. R. Dingle, D.D. Sell, S.E. Stokowski, and M. Ilegems, *Phys. Rev. B* **4**, 1211 (1971).
142. R. Dai, S. Fu, J. Xie, G. Fan, G. Fu, H. Schrey, and C. Klingshirn, *J. Phys. C* **15**, 393 (1982).
143. J. Miragliotta, D.K. Wickenden, T.J. Kistenmacher, and W.A. Bryden, *J. Opt. Soc. Am.* **B10**, 1447 (1993).
144. S. Strite and H. Morkoc, *J. Vac. Sci. Technol.* **B10**, 1237 (1992), and references therein.
145. G. Ramirez-Flores, H. Navarro-Contreras, A. Lastras-Martinez, R.C. Powell, and J.E. Greene, *Phys. Rev. B* **50**, 8433 (1994).
146. S. Strite, Ph.D thesis, University of Illinois, 1993.
147. T. Lei, K.F. Ludwig, Jr and T.D. Moustakas, *J. Appl. Phys.* **74**, 4430 (1993).
148. R.C. Powell, G.A. Tomasch, Y.-W. Kim, J.A. Thornton, and J.E. Green, *Mater. Res. Soc. Symp. Proc.* **162**, 525 (1990).

149. S. Strite, D. Chandrasekhar, David J. Smith, J. Sariel, H. Chen, N. Teraguch, and H. Morkoc, *J. Cryst. Growth* **127**, 204 (1993).
150. P.J. Dean, in *Progress in Solid State Chemistry*, edited by J.O. McCaldin and G.Somorjai (Pergmon, New York, 1973), Vol. 8, Chap. 1.
151. *Landolt-Borstein*, edited by O. Madelung (Springer-Verlag, Berlin, 1982), New Series, Vol. 17a.
152. J. Chadi and K.J. Chang, *Phys. Rev. Lett.* **61**, 873 (1988).

VITA

Seon-Ju Hwang

Candidate for the Degree of

Doctor of Philosophy

Thesis: OPTICAL PROPERTIES OF III-V AND II-VI STRAINED SEMI-
CONDUCTOR HETEROSTRUCTURES UNDER PRESSURE

Major Field: Physics

Biographical:

Personal Data: Born in Pusan, Korea, on December 12, 1958, the son of Hee-Ok Cho and Chi-Hyun Hwang.

Married Yun O. Lee, October 3, 1987. Two children.

Education: Received Bachelor of Science Degree and Master of Science Degree in Physics from Pusan National University, Pusan, Korea in February 1982 and in February 1984, respectively. Completed requirements for the Doctor of Philosophy Degree at Oklahoma State University in December 1994.

Professional Experience: Researcher at Research and Development Center, Samsung Electron Devices, Suwon, Korea from February 1984 to February 1986; Research Assistant at Department of Physics, Central State University, Edmond, Oklahoma from January to May 1987; Teaching Assistant, Department of Physics, Oklahoma State University, from August 1987 to May 1989; Research Assistant, Department of Physics and Center for Laser Research, Oklahoma State University, from June 1989 to present.

Professional Memberships: American Physical Society, Association of Korean Physicists in America, and Korean Scientists and Engineers in America.